THE IMPLICATIONS OF EFFECTIVE STACKING FAULT ENERGY AND LOCAL MICROSTRUCTURE ON THE MONOTONOUS AND CYCLIC DEFORMATION OF SOME MEDIUM/HIGH-Mn STEELS

THESIS SUBMITTED FOR THE DEGREE OF

DOCTOR OF PHILOSOPHY (SCIENCE)

OF

JADAVPUR UNIVERSITY

2023

By

Saikat Shyamal

Index No: 137/19/Phys./26

Reg. No: SOPHY1213719

Department of Physics

Jadavpur University

Kolkata-700 032

INDIA

Dedicated

to

my parents

যাদবপুর বিশ্ববিদ্যালয়
কলকাতা - ৭০০ ০৩২, ভারত

JADAVPUR UNIVERSITY
KOLKATA-700 032, INDIA

FACULTY OF SCIENCE : DEPARTMENT OF PHYSICS

CERTIFICATE FROM THE SUPERVISOR

This is to certify that the thesis entitled "***The implications of effective stacking fault energy and local microstructure on the monotonous and cyclic deformation of some medium/high-Mn steels***" submitted by Mr. Saikat Shyamal, who got his name registered on 14th November 2019 for the award of Ph.D. (Science) degree of Jadavpur University, is absolutely based upon his own work under my supervision and that neither this thesis nor any part of it has been submitted for any degree/diploma or any other academic award anywhere before.

Signature of the supervisor

and date with official seal

ACKNOWLEDGEMENTS

I would like to take this opportunity to convey my sincere gratitude towards all those people who have extended their valuable assistance, encouragement and contribution indispensably to this PhD work in one way or the other.

First and foremost, I would like to thank my supervisor Dr. Puspendu Sahu for his kindness, constant enthusiasm and guidance. I am extremely grateful for his continuous streams of ideas, which opened many avenues for study and for his intensive proof reading of this thesis. I have been fortunate enough in unflinching support and encouragement from him. I could not have imagined having better advisor and mentor for my Ph.D. study.

I extend my thanks to my lab mates who have assisted me immensely during this tenure. From the core of my heart, I would like to specially thank Dr. Bhupeshwar Mahato (CSIR NML, Jamshedpur) for his contribution related to TEM investigation. I would like to thank of my Lab mate Dr. Soma Rani Das, Mr. Tousif Riaz and Mr. Dhananjay Das for all contribution and support.

In my PhD tenure, I got the opportunity to work in close collaboration with Dr. Swapan Kumar Shee (Midnapore College), Prof. Pravash Chandra Chakraborti (Jadavpur University), Prof. Jukka Komi (University of Oulu), Prof. L. Pentti Karjalainen (University of Oulu), Prof. David Porter (University of Oulu), Matias Jaskari (University of Oulu) and Dr. Jadav Mola (Osnabrück University). I want to express my deep gratitude to all of them.

I extend special acknowledgement to all the office staff for their help in regards to all official's activities related directly or indirectly to my research work during these years.

I don't have any idea how to acknowledge my family. I must say that I would not have been able to come to this stage without their constant encouragement, support, love and prayers. Words cannot express how grateful I am to my parents for all of the sacrifices that they have made on my behalf.

I must thank my college friends Dipak, Pande, Sibaram, Sourav, Subham, Suman and university friends Anu, Arunavo, Brindaban, Pritwish for their timely support and friendship that I needed. I would like to thank Manish, Santanu, Rahul, Prabhakar, for their support and friendship. I also want to thank my dearest friend Swapan Karan for his continuous support through out this journey.

I would like to thank my special friend Chayanika Barman for her immense and continuous support during the end of this journey.

To conclude this, I would like to acknowledge the "JOINT CSIR-UGC NET Fellowship" for providing me the financial support. So, again thanks to all.

Date: Saikat Shyamal

PREFACE

The present dissertation reports the effects of effective stacking fault energy and the local microstructure on the deformation behaviour of cyclic and uniaxially deformed different medium/high-Mn steels. The thesis is divided into three parts i.e., Part A, Part B and Part C. Part A contains two Chapters, Part B contains two Chapters and three Chapters belongs to Part C. Chapter 1 briefly describes strain hardening in metals/alloys, cyclic and monotonous deformation microstructure and short literature review on the influence of effective stacking fault energy and local microstructure in different medium/high-Mn steels. Chapter 2 concerns the description of underlying X-ray and electron diffraction theories used towards assessment of deformation microstructure. Chapter 3 describes materials processing, initial microstructure & the mechanical behaviour of the studied steels, whereas, Chapter 4 deals with the determination of stacking fault energy of the studied steels using different methods. In Chapter 5, the cyclic deformation microstructure of a high-Mn steel is interpretated using a combination of X-ray line profile analysis and transmission electron microscopy, while Chapter 6 discusses the active deformation mechanism during monotonous deformation of a medium-Mn steel studied using extensive TEM investigations. Finally, Chapter 7 gives the overall conclusions of the dissertation.

As the title suggested, in this study two different types of steels were investigated. One of them is a high-Mn steel with chemical composition of Fe–16Mn–1.5Al–0.3C, and another is a medium-Mn steel having a chemical composition of Fe-0.17C-2.2Si-10.8Mn-18.0Cr-4.7Ni-0.9V-0.25N. It must be mention here that all the compositions reported throughout this dissertation are in weight %, unless otherwise specified. All the steels were prepared by induction furnace melting and also suitable thermomechanical treatments were applied as per the requirement, which is confirmed by studying the initial microstructure of the steels using electron backscatter diffraction (EBSD). The interrupted high-cycle fatigue (HCF) tests of the high-Mn steel were carried out at room temperature (RT), and the resulted deformation microstructure were investigated at both, pre-saturation and saturation stages, with the help of X-ray diffraction (XRD) and a transmission electron microscope (TEM). The obtained cyclic deformation microstructure was interpretated in terms of the quantitative values of different microstructural parameters such as: dislocation density, stacking fault probability, stacking fault energy etc. as estimated from X-ray line profile analyses and

the findings were also substantiated with TEM observations. However, in case of the medium-Mn steel, the interrupted uniaxial tensile tests were carried out at RT with a quasi-static strain rate of 10^{-3} s^{-1}, and the active deformed mechanisms were recognized at early stage of deformation with the help of extensive TEM investigations.

CONTENTS

Part A

General Introduction & Methodologies

Chapter 1: General introduction

Chapter 2: Methodologies associated to microstructure characterization

Part B

Materials & Their SFEs

Chapter 3: Materials processing, initial microstructure & their mechanical responses

Chapter 4: Determination of SFEs of the selected steels

Part C

Interpretation of Deformation Microstructure

Chapter 5: Cyclic deformation microstructure of the high-Mn steel

List of Publications

Journal Publications:

1. Activation of a hybrid twinning mechanism in a Cr-Ni-Si-VN medium manganese austenitic steel containing precipitates.

   S. Shyamal, M.G. Farahani, T. Allam, A. Hamada, C. Haase, J. Kömi, P.Chak raborti, P. Sahu*, *Scripta Mater.*, 192 (**2021**) 83-88.

2. Graded deformation in an Fe-Mn-Al-C steel under bending fatigue.

   S. Shyamal, S.R. Das, M. Jaskari, D.A. Porter, L.P. Karjalainen, P. Sahu*, *Materials Letters*, 285 (**2021**) 129002.

3. Evolution of deformation microstructure in a coarse-grained Fe-Mn-Al-C steel under bending fatigue.

   S. Shyamal, S.R. Das, M. Jaskari, P. Sahu*, *Materials Letters*, 327 (**2022**) 133006.

4. X-ray line profile analysis of the deformation microstructure in a medium-grained Fe-Mn-Al-C austenitic steel

   S.R. Das, **S. Shyamal**, S.K. Shee, J.I. Kömi and P. Sahu*, *Materials Characterization*, 172 **(2021)** 110833.

5. On the mechanism of cross-slip induced dislocation substructure formation in an high-Mn steel.

   S.R. Das, **S. Shyamal**, T. Sahu, J.I. Kömi, P.C. Chakraborti, D.A. Porter, L.P. Karjalainen and P. Sahu*, *Materialia* 15 **(2021)** 101042.

6. A quantitative assessment on the contribution of various dislocation substructures to flow stress in a fine-grain high-Mn steel.

   S.R. Das, T. Riaz, **S. Shyamal**, P.C. Chakraborti and P. Sahu*, *Materials Letters*, 300 **(2021)** 130216.

7. Transmission electron microscopy investigations on the twinning suppression attributes in a Fe-Mn-Al-C steel and the associated strain hardening.

   S.R. Das, **S. Shyamal**, M. Jaskari, P.C. Chakraborti, L.P. Karjalainen, P. Sahu*, *Materials Letters*, 324 (**2022**) 132730.

8. Microstructural Constituents and Mechanical Properties of Low-Density Fe-Cr-Ni-Mn-Al-C Stainless Steels.

Steffen Scherbring, Guanghui Chen, Bastian Veltel, Gert Bartzsch, Julia Richter, Malte Vollmer, Malte Blankenburg, **Saikat Shyamal**, Olena Volkova, Thomas Niendorf, Ulrich Lienert, Puspendu Sahu, Javad Mola*, Materials, 15 (15) (**2022**) 5121.

9. X-ray line profile analysis on the deformation microstructure of Al-bearing high-Mn steels.

   T. Riaz, **S. Shyamal**, S.K. Shee, L.P. Karjalainen, P. Sahu*, *Materials Characterization*, 196 (**2023**) 112567.

List of Communicated Paper:

1 On the comparison of various diffraction-based methods of estimating stacking fault energy in face-centred cubic metals and/or alloys: a case study with Fe-Mn-Al-C steel (communicated)
S. Shyamal, P. Sahu*.

List of Presentation/Participation in conferences

1 Oral presentation of a paper entitled "Grain size dependent deformation microstructure of Fe-Mn-Al-C steel under bending fatigue" in "**International Conference of Multidisciplinary Aspects of Materials in Engineering (IC-MAME 2021)**" October 8-9, 2021, Panjab University, Chandigarh, India.

2. Oral presentation of a paper entitled "On deformation microstructure of a high-Mn steel comprise of bimodal grain size distribution" in "**International Conference on Future Trends in Materials and Mechanical Engineering (IC-FTMME 2022)**" August 19-20, 2022, SRM IST, Delhi-NCR campus, Ghaziabad, India.

List of symbols*

X_s	Annihilation distance of screw dislocation
n	Any integer
D	Apparent crystallite size
σ_A	Applied tensile stress
$\bar{C}_{hkl}$	Average contrast factor for (hkl) planes
L_0	Average length of the twinning source
θ_{hkl}	Bragg angle
$\vec{b}_p$	Burgers vector of partial dislocations (Shockley/Frank)
β'	Character angle between the diffraction vector and dislocation line
E_{str}	Coherency strain energy
$\rho(D)$	Column length (size) distribution function
τ_{crss}	Critical resolved shear stress
$(\tau_c)_{twin}$	Critical twinning stress
ΔK	Deviation from diffraction vector
s	Deviation from exact Bragg angle condition in TEM
ΔL	Deviation from L
$\vec{\mathrm{g}}$	Diffraction vector
K	Diffraction vector for X-ray analysis
E_{dil}	Dilatation energy due to volumetric stress
q	Dislocation character parameter
ρ	Dislocation density
α_i	Dislocation interaction strength parameter
R_e	Effective outer cut-off radius of dislocations
γ_{eff}	Effective stacking fault energy
B	Electron beam direction
ε_{hcp}	Epsilon martensite (hcp)
x_{eq}	Equilibrium separation distance of the partial dislocation pairs
α''	Extrinsic stacking fault probability
σ	Flow stress

L	Fourier variable
$f_{\gamma(edge)}$	Fraction of edge dislocation
$f_{\gamma(screw)}$	Fraction of screw dislocation
d	Grain size
γ_{∞}	Ideal stacking fault energy
d_{hkl}	Interplanar spacing for (hkl) planes
γ_{isf}	Intrinsic stacking fault energy
α'	Intrinsic stacking fault probability
$\vec{R}$	Lattice distortion vector
σ_{YS}^{0}	Lattice friction stress
a	Lattice parameter
β	Line breadth
$\vec{u}$	Line direction of dislocations
$\langle \varepsilon_L^2 \rangle$	Mean square microstrain
ε_L	Mean squared strain
H_v	Microhardness
$A^d(L, K_i)$	Order dependent Fourier strain coefficient
$A^s(L)$	Order independent Fourier size coefficients
$\vec{b}$	Perfect dislocations' Burgers vector
ν	Poisson's ratio
K_s	Scherrer constant
E_{sh}	Shear strain energy
m_T	Shear for partial dislocation
m_G	Shear for perfect dislocation
G	Shear modulus
τ	Shear stress
β_s	Size broadening integral breadth
d_{ex}	Split distance of screw dislocation
γ	Stacking fault energy
P_{sf}	Stacking fault probability
κ	Stacking fault band width
β_D	Strain broadening integral breadth

$\rho(\varepsilon_L)$	Strain distribution function
T	Taylor factor
P_{tw}	Twin fault probability
γ_{usf}	Unstable stacking fault energy
e	Vector normal to the dislocation line
λ	Wavelength of X-rays
σ_{YS}	Yield stress

* Symbols appearing in several equations/figures obtained from literatures are not described here. This list primarily describes the symbols considered in the present work.

Abbreviations

BSE	Backscatter electron
BF	Bright field
CCD	Charge-coupled device
CG	Coarse grain
DF	Dark filed
DRV	Dynamic recovery
DSA	Dynamic strain ageing
EBSD	Electron backscatter diffraction
ESF	Extrinsic stacking fault
fcc	Face-centre cubic
FESEM	Field emission scanning electron microscope
FWHM	Full width half maximum
GPA	Geometric phase analysis
HRTEM	High resolution transmission electron microscopy
High-Mn	High-Manganese
ICDD	International centre for diffraction data
ISF	Intrinsic stacking fault
IPF	Inverse pole figure
LEDS	Low-energy dislocation structures
MMn	Medium- Manganese
MBIP	Microband induced plasticity
RT	Room temperature
SEM	Scanning electron microscope
SAED	Selected area electron diffraction
SPD	Shockley partial dislocation
SRC	Short-range clustering
SRO	Short-range order
SF	Stacking fault

SFE	Stacking fault energy
SHR	Strain hardening rate
TRIP	Transformation induced plasticity
TEM	Transmission electron microscope
TWIP	Twinning induced plasticity
UTS	Ultimate tensile strength
WA	Warren-Averbach
WB	Weak beam
WBDF	Weak beam dark field
XRD	X-ray diffraction
YS	Yield strength

Part A

General Introduction & Methodologies

Chapter 1

General introduction

1.1 Background of the work

The development of metals/alloys with superior mechanical properties i.e. combination of high strength, ductility and toughness is a challenge for the material scientists for several decades. However, scientists have successfully developed few of such steels that include advanced high-strength steels comprising dual-phase steels, transformation-induced plasticity (TRIP) steels and high-manganese austenitic steels for automotive applications. But, the upcoming electric-vehicle (EV) boom around the world in recent years has gained a great attention to enhance the fuel efficiency by further reducing the vehicle weight without compromising the safety of the passengers during crash management test and which basically provided by the strength of the steels. In general, a high level of specific strength requirement is achieved mainly by increasing the strength of the advanced steels (Grassel *et al*., 2000; Fan *et al*., 2009; Bhadeshia, 2010; Jang *et al*., 2012). However, another way of strength improvement can be done by alloying lighter elements such as Al (and/or Si) with the Fe-Mn-C-base alloy system, which have been investigated not only for several interesting applications, namely: (i) cryogenic application, (ii) oxidation resistance at high temperature and (iii) corrosion resistance, but this base alloy system can also be used as a potential substitute for more expensive Fe-Cr-Ni base stainless steels (Lee *et al*., 1992; Shih *et al*., 1993; Saxena *et al*., 1994; Zhu & Zhang, 1998; Herrmann, 2003; Hamada & Karjalainen, 2006; Morris *et al*., 2006). Therefore, much effort has been directed for the last two decades towards the development of ductile lightweight steels with high strength and reduced density for structural applications, and the Fe-Mn-Al-C system has been studied in Europe and Japan for automotive applications since the early 2000s.

In 2006, Frommeyer and Brux (Frommeyer & Brux, 2006) reported that the lightweight Fe-Al-Mn-C alloy system display an excellent high-strength and ductility combination, and they also further invented the term called TRIPLEX steels, which is basically a multiphase steel with three major phases. They studied the microstructure of such TRIPLEX steels, and also showed that the microstructures are composed of 5–15 vol.% of ferrite and nano-sized κ-carbides with less than 10 vol.%, which are finely dispersed throughout the austenite matrix. The composition range of these steels covers Fe-(18–28) Mn-(9–12) Al-(0.7–1.2) C (in wt%), and their typical alloy with chemical composition Fe-28Mn-12Al-1C exhibit a yield strength (YS) of 730 MPa, an ultimate

tensile strength (UTS) of 1000 MPa and total elongation of 55% during room temperature (RT) uniaxial tensile test with a strain rate of 10^{-4} s^{-1}. It is well known that the lightweight high-Mn (>13 wt%) steels display an excellent strength-ductility combination and, which meet the basic necessities of automobile industry. The presence of high-Mn content makes the lightweight steels more susceptible for crack initiation during processing, and therefore, recently medium-Mn (<12 wt%) lightweight steels are also getting more attentions to reduce such difficulties as compared to the high-Mn steels production. The mechanical properties of the conventional as well as different advanced grade steels are presented in Fig. 1.1. It is to be mentioned here that although the concept of lightweight steel looks quite simply, but the underlying metallurgical issues related to the material processing techniques are very complicated. Additionally, the lightweight steels can have both the single phase like: ferritic, austenitic or even a multiphase structure depending on the content of primary alloying elements of C, Mn or Al which also complicates the deformation mechanism of the steel as well.

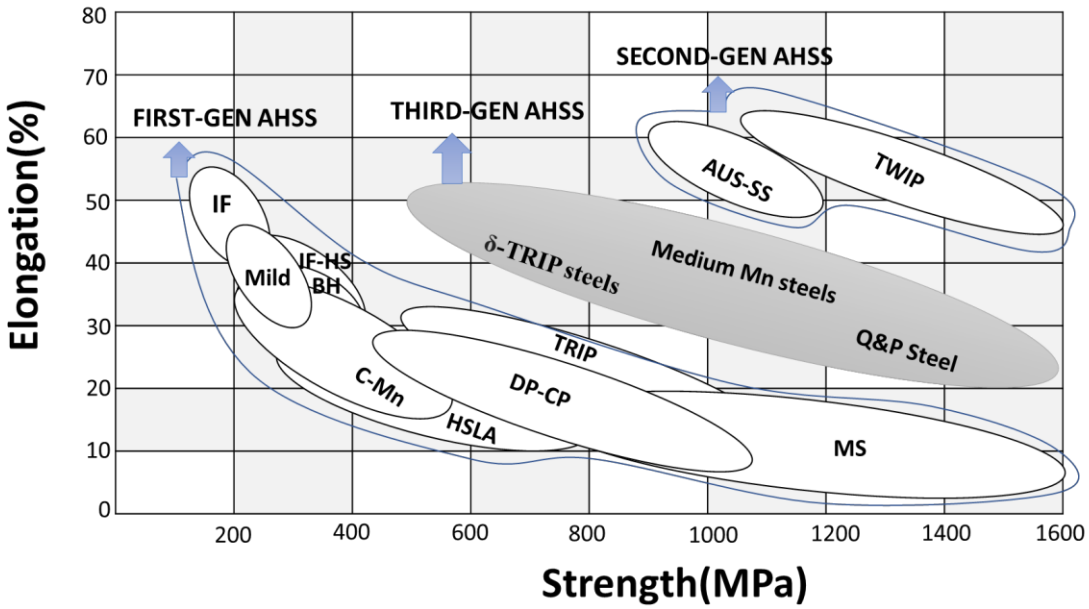

Fig. 1.1: Mechanical properties of various classes conventional and advanced high strength steel (AHSS) grades showing their tensile strength and corresponding elongations (McDermid et al., 2016).

The deformation behavior of face-centred cubic (fcc) metals/alloys strongly influenced by several microstructural parameters such as: grain size, stacking fault energy (SFE), local deformation microstructure etc. In case of high-Mn steels the superior ductility comes due to occurrence of enormous mechanical twin formation during deformation. The grain size of austenite controls the deformation behaviour significantly by influencing the deformation microstructures of a given high-Mn steel (Ueji *et al*., 2000; Gutierrez *et al*., 2008; Dini *et al*., 2010; Gutierrez & Raabe., 2012a; Lee, 2012). The mechanical twin densities are known to significantly decreases at the same strain by refining the grain size from 49.6 μm to 1.8 μm for Fe-31Mn-3Al-3Si high-Mn steel (Ueji *et al*., 2000). Ueji *et al*. (2000) explains this observations in terms of the development of a non-planar dislocation substructures (Dini & Ueji, 2012), while Gutierrez-Urrutia *et al*. (2008) believes that grain refinement retards mechanical twinning by increasing the critical twinning stress in Fe-22Mn-0.6C steel.

Another most important parameter that significantly influence the deformation behavior of lightweight austenitic steels is the SFE of the concerned materials. Depending on the SFE value different plasticity enhancing mechanisms such as: twining induced plasticity (TWIP), transformation induced plasticity (TRIP) and micro-band induced plasticity (MBIP) activates, and gives different types of deformation microstructures, and which are of course competitive with the primary deformation mechanism of any materials i.e. dislocation glide. The strain-induced martensitic transformation is known to be dominant deformation mechanism for high manganese (high-Mn) austenitic steels only when the SFE of austenite is less than about 20 mJ/m^2, whereas, deformation is likely to be controlled by mechanical twins for a SFE values above 20 mJ/m^2 – leading to the well-known twinning induced plasticity (TWIP) effect (Olson & Cohen, 1976a, 1976b). Frommeyer *et al.* (2000) reported that a transition in deformation behavior from TRIP to TWIP occurs in Fe-3Si-3Al-Mn alloys while Mn content increases from 15 to 25%. They also suggest that the strain-induced martensitic transformation ($\gamma_{fcc} \rightarrow \varepsilon_{hcp} \rightarrow \alpha'$) i.e., the TRIP effect dominates up to 15–20% Mn concentrations, while any further increase in Mn content elevates the SFE of the system and mechanical twinning become a major deformation mode i.e. TWIP effect predominates. However, the exact range of SFE value related to the different deformation mechanism activated in different grade steels are still questionable (De Cooman et al., 2018).

The formation of dislocation cell is profound during the plastic deformation of high-Mn steels only when the SFE is higher than 30-40 mJ/m^2 (Remy & Pineau, 1977). It is well accepted that before cell formation the dislocations must cross-slip to another slip system, and interestingly the cross-slip activated mostly in case of high SFE condition, whereas, the planar glide of dislocation is mostly observed during deformation of fcc metals/alloys having low SFE (Kuhlmann, 2001). However, many Fe-Al-Mn-C austenitic steels deform only by planar glide rather than wavy glide of dislocations, despite of having a high SFE value (Frommeyer & Brux, 2006; Yoo & Park, 2008; Choi *et al*., 2010; Park *et al*., 2010). For instance, Fe-28Mn-12Al-1C alloy subjected to ageing for 16h at 550˚C revealed shear band formation by planar glide even with a SFE value of ~ 110 mJ/m^2 (Frommeyer & Brux, 2006). Subsequently, Park *et al.* (2010) also observed that the solution treated Fe-28Mn-9Al-0.8C with SFE value ~ 85 mJ/m^2 deformed only by planar glide of dislocation. Park *et al.* (2010) and Park (2013) also attributed the planar dislocations glide in high-Mn steels to the glide softening phenomenon associated with short-range ordering (SRO) in the solid solution state.

Furthermore, it must be mentioned here that the deformation mechanism of steels also strongly influenced by the presence of local microstructures, and therefore, deformation mechanisms may also very with positions depending on the pre-existing local microstructures. Lee (2012) reported that the grain refinement retarded the appearance of mechanical twins in the deformation microstructures by increasing the local SFE near to the grain boundaries where the C atoms are segregated due to or the increased back stress of dislocations. It is well accepted that different heterogeneous twin nucleation in fcc materials obey the classical twinning models, which basically consist of several dislocation-based mechanisms (Venables 1974, Christian et al., 1995; Niewczas et al., 2002). However, Christian et al. (1995) sugesst that the deformation twin nucleates not only at the sites having high local stress concentrations but it is also controlled by several interrelated local variables, namely, grain size, grain orientation, precipitates, local SEF etc. Nevertheless, the exact influence of SFE and the local microstructures on the deformation behaviour is still a debated issue, and the present dissertation aims to provide newer insights in the deformation mechanisms of high/medium-Mn steel in terms of SFE and local deformation microstructures.

1.2 Strain hardening in metals/alloys

1.2.1 The Hall-Petch theory

In the 1950s, Hall and Petch first demonstrated that a ground-breaking information which suggest that the yield stress (σ_{YS}) and hence the hardness of any polycrystalline materials inversely proportional to the square root of the grain size of that material. The variations of yield stress as a function of grain size of a mild steels are also plotted in Fig. 1.2, which clearly indicate that the yield stress varies with grain size according to the following relation (Hall, 1951; Petch, 1953):

$$\sigma_{YS}(MPa) = \sigma_{YS}^{0} + \frac{k_{YS}^{HP}}{\sqrt{d}} \qquad (1.1)$$

where the parameter σ_{YS}^{0} includes the lattice friction stress, the solid solution strengthening contribution of the alloying elements, and the strain hardening contribution of the initial dislocation density, k_{YS}^{HP} is a material parameter, and d is the average grain size (Armstrong, 2014).

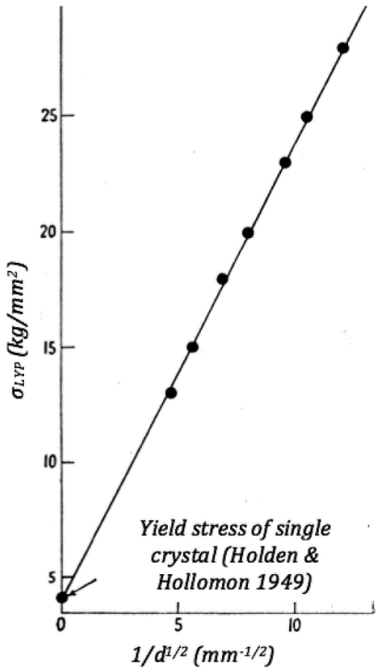

Fig. 1.2: The relationship between lower yield point (σ_{LYP}) and grain size, d, in mild steel (Hall, 1951).

The above mentioned Hall-Petch relationship has been explained by a dislocation pile-up model considering the stress concentration at the tip of a slip band (Armstrong, 2014; Cordero *et al*., 2016), but recently, the validity of this relationship has been debated (Li, 2016). In the 1980s, Gleiter *et al*. (1989) pioneered his research work into polycrystalline materials with nanometre grain size, and previously it was expected that these nanometre grain size materials would exhibit superior hardness as well as superior wear resistance and fracture strength as compared with their coarse-grained counterparts due to the large volume fraction of grain boundaries, which were known to govern the response of metals to deformation (Meyers *et al*., 2006; Pande & Cooper, 2009). Although the hardness measurements of some nano-crystalline samples have been reported to be consistent with the Hall–Petch equation, the grain boundary weakening has also been reported for nano-crystalline materials having typical grain sizes less than 30 nm, so-called inverse Hall–Petch effect (Chokshi *et al*., 1989; Koch & Narayan, 2000). Interestingly, the inverse Hall–Petch effect has been observed both experimentally (Chokshi *et al*., 1989), as well as in molecular dynamics (MD) simulations (Schiotz & Jacobsen, 2003; Huang, 2018; Xu & Davila, 2018; Kuhr & Aifantis, 2019). Several scientists had attempted to interpret the grain boundary weakening, and stated that the weakening has been mainly attributed to (1) processing artefacts (Meyers *et al*., 2006; Koch & Narayan, 2000), (2) disordered grain boundaries (Armstrong, 2016), and (3) the higher percentage of material in grain boundaries (Carsley *et al*., 1995; Carsley *et al*., 1998). Other investigations interpreted it as being the transition from dislocation controlled to grain boundary and diffusion-dominated deformation (Pande & Cooper, 2009).

1.2.2 Different stages of strain hardening

Deepening on the mechanical response Diehl (1956) first divided the stress-strain curve of single crystals into three stages, which are clearly delineated in the flow-stress curve presented in Fig. 1.3. He mentioned that the Stage I is occurred only during the activation of a single slip system in the single crystals, while the linear hardening stage (Stage II) have relatively high work hardening rate. Additionally, he also suggests that it may occur in both cases: single crystals and polycrystals, and this Stage II is independent of Stage I. However, this type of hardening behavior is considered as a limiting case for small strains, as its validity decreases with increasing temperature and

SFE. The Stage III represents a steady decrease in work hardening rate and it is quite sensitive to both, deformation temperature and strain rate. In case of large strain, a further stage IV must be added to the work hardening plot, and this stage possesses a low-level work hardening that persists in some cases deformed to very large strains. The existence of a stage IV in work hardening requires modification of the theory associated to stage III that predicts saturation of flow stress at the end of stage III. Some authors also refer to the existence of one more stage i.e., V/E, where further dynamic recovery takes place leading to an eventual actual saturation of the flow stress.

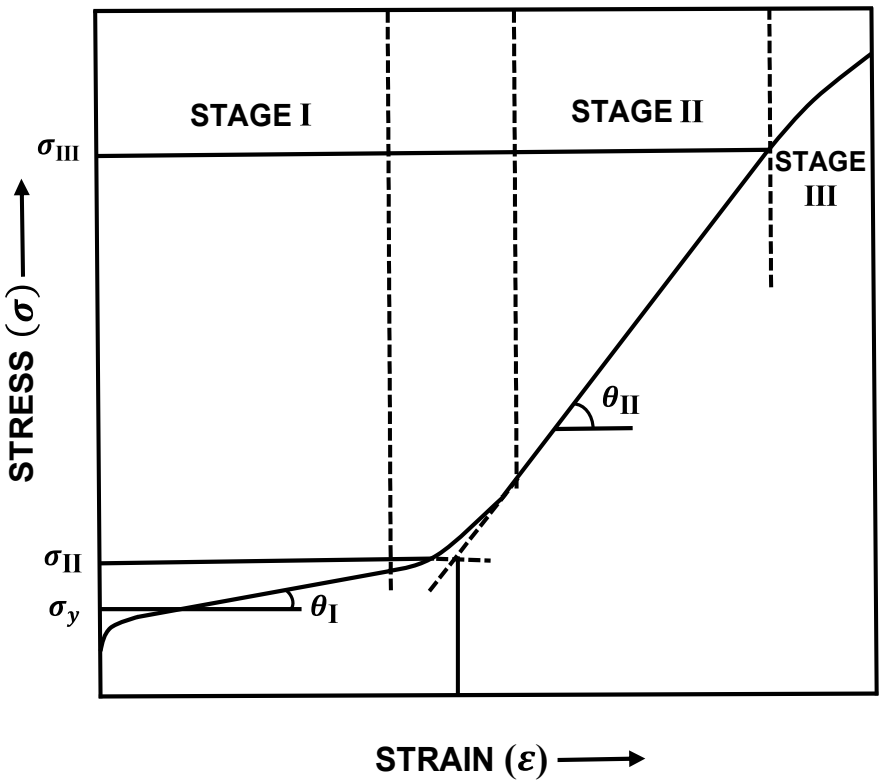

Fig. 1.3: The stages of work hardening and associated deformation mechanisms: Stage I easy glide, Stage II athermal work hardening and Stage III dynamic recovery (Diehl,1956).

The various stages of work hardening can also be distinguished even more clearly from the variation of θ versus ε, where $\theta = \frac{d\sigma}{d\varepsilon}$, and which is also presented in Fig. 1.3. It is to be mentioned here that the Stage II/B is commonly found in case of materials having low SFE and also deformed only at low temperature. The Stage III/C

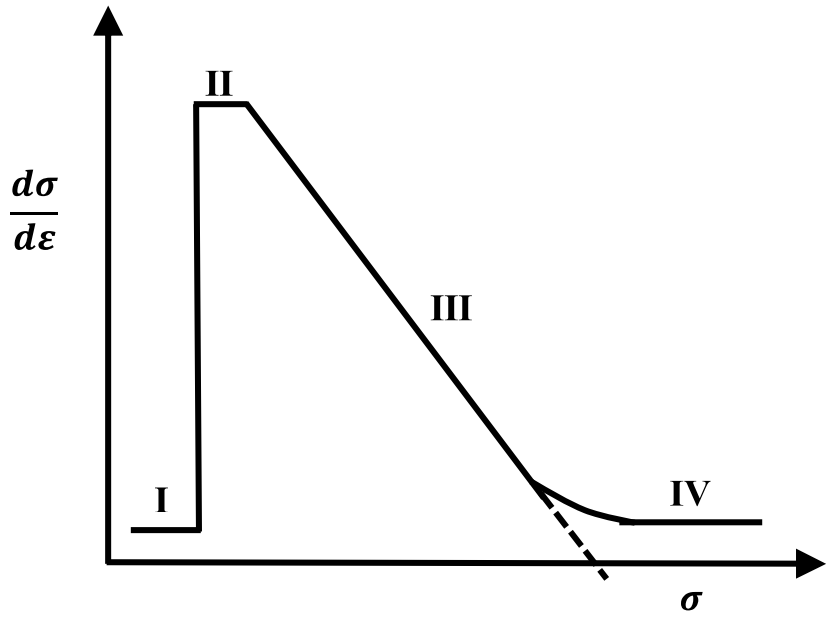

Fig. 1.4: Different work hardening stages of a single crystal represented on a plot of hardening rate versus flow stress. A polycrystalline material would show stages III & IV, possibly II also (Rolltt & Kocks, 1993).

is often represented by a straight line where the hardening rate decreases linearly with stress towards a "saturation stress", whereas, the Stage IV/D manifest before the saturation stress is reached and it is commonly assumed as a stage of constant and low hardening rate stage.

1.3 Mechanical response and associated deformation microstructures

It is well accepted that the mechanical response of any material is strongly correlated to the associated microstructural information of that material. In 1935, Chévenard first noticed the microstructural evolution with plastic strain, and also indicate the formation of a hard phase in the deformation microstructure while investigating the work-hardened Hadfield steels using thermo-magnetometry at room temperature (Chévenard, 1935). Later, Troiano and McGuire (1943) concluded that the evolution of any hard phase during plastic deformation arises as a result of the imposed plastic strain, and they also predicted that the mechanically induced phase transformation in Fe–Mn binary alloys can occur only by two mode of phase transformations: ε- martensite and α'-martensite. However, the existence of hexagonal ε- martensitic phase was first discovered by Schmidt while investigating the deformation microstructure of Fe–Mn

alloys with manganese contents lies in between 12 and 29 wt.% (Schmidt, 1930). In the 1950s, researchers first identify the presence of planar defects in deformed Hadfield steels by using optical micrographs, and also mentioned the occurrence of mechanical twinning (Doepken, 1952; Otte, 1957). After few years, the scientists have finally confirmed the presence of deformation twinning by using a direct observation method like TEM (Roberts, 1964; Raghavan et al., 1969). In this context, it must be mentioned here that the evolution of deformation microstructures strongly influenced by the types of deformation that were imposed on the specimen, and which are briefly discussed subsequently.

1.3.1 Monotonic deformation

The investigations related to the monotonic deformation behaviour of different grades advanced high strength steels (AHSS) possessing high strength and ductility combinations were studied significantly for their enormous application in the automotive industry. Several investigations were carried out related to the stress-strain response and strain hardening behaviour of different grade AHSS, and it found that the different grade steels display different types of hardening behaviour (Grassel et al., 1997; Grassel *et al*., 2000; De Cooman et al., 2018). The flow stress curve and the corresponding strain hardening behaviour of different grade steels such as: TWIP, high strength interstitial free (IF) and TRIP steels are presented in Fig. 1.5 and it must be mentioned here that the TWIP steels having strength of 1 GPa are considered in Fig. 1.5 for comparison. Interestingly, Fig. 1.5 clearly indicate that the TWIP steel has considerably higher UTS and almost twice the uniform elongation than that of TRIP steel. It is well established that TWIP steels possesses large uniform elongation due to the occurrence of deformation twin in the microstructures, although the exact cause of appearance of deformation twin and its influence on the deformation behaviour still not clearly understood (De Cooman et al., 2018).

In general, the imposed plastic strain in metals/alloys are utilized to crate different types of crystal defects and thereby hardened the material up to a certain strain limit and then failed. Depending on the types of defects created in the deformation microstructure the strain hardening mechanism of different grade steels varies, although dislocation planar glide is the primary deformation for any metals/alloys at early stage of deformation. When the imposed plastic strain are not

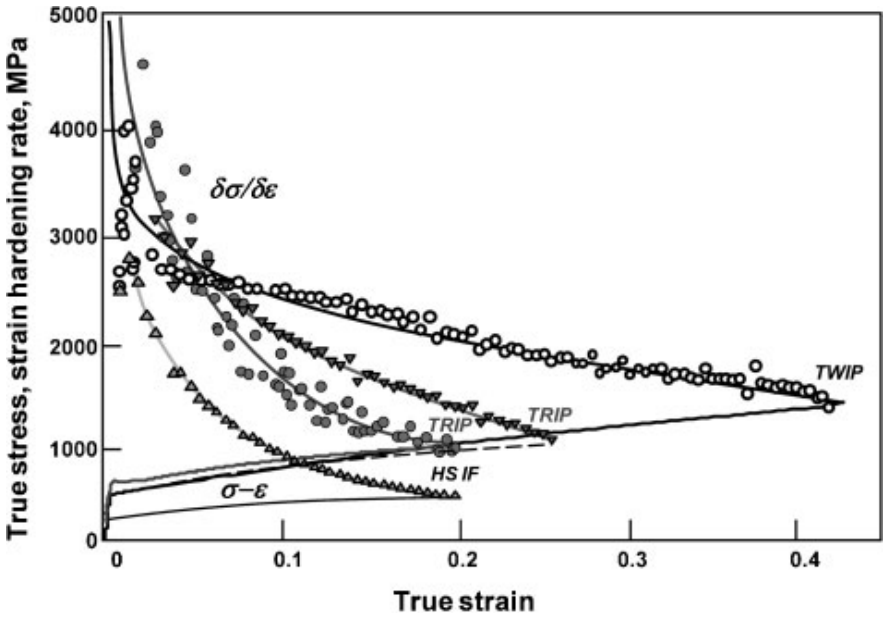

Fig. 1.5: Comparison of the stress-strain response and strain hardening behaviour of different grade steels under monotonic deformation (De Cooman et al., 2012).

accommodated only by gilding of dislocations then additional deformation mechanisms like twining, different dislocation substructures, cross-slip etc actives. In case of high-Mn steels having SFE value range of 21-39 mJ/m^2, this additional deformation mechanism is twining, whereas, the strain-induced martensitic transformation ($\gamma_{fcc} \rightarrow \varepsilon_{hcp} \rightarrow \alpha'$) dominates over any other additional deformation mode for a SFE value < 20 mJ/m^2 (De Cooman et al., 2018; Pierce *et al*., 2012; 2014). The superior mechanical properties of TWIP steels can be explained in terms of dislocation interactions to the obstacle (twin), which basically reduce effective 'mean free path' or effective glide distance of dislocations and increase the flow stress.

1.3.2 Cyclic deformation

Initially, the investigations related to the fatigue behaviour of high-Mn austenitic steels were mainly focused on surface fatigue wear of Hadfield steels, due to their extensive usage in railway switch and crossings applications (Clayton et al., 1992). At that time, the scientists were dealing with the basic fatigue properties of Hadfield steels, namely, cyclic work hardening, notch sensitivity, crack growth rate etc. (Colette et al., 1957; Katyk et al., 1985; Rittel et al., 1989). However, the investigations related to the basic fatigue properties of high-Mn steel was first reported in 2005 by Cornette et al. (2005), and they showed that the high-Mn steel with chemical composition Fe–22Mn–0.6C

offers a fatigue limit typically correlated to its ultimate tensile strength in the high cycle fatigue (HCF) regime, which is expected for standard steels. A similar kind of observations were also later confirmed by Hamada and his co-workers (Hamada et al., 2009) while investigating on coarse grained TWIP steels having different chemical compositions, such as: Fe–22Mn–0.6C, Fe–18Mn–0.6C–0.02Nb and Fe–16Mn–0.3C–1.5Al. They obtained a fatigue limit of 400 MPa for all the above mentioned three TWIP steels, whereas, the corresponding fatigue limit/tensile strength ratios varies from 0.42 to 0.48. The fatigue behaviour of the studied TWIP steels are plotted in Fig. 1.6, in which two commercial stainless steels are also included purposefully for comparison. It is clearly seen from Fig. 1.6 that the fatigue limits of commercial stainless steels are lower than the TWIP steels, while their fatigue limit/tensile strength ratio lies in the same range as TWIP steels.

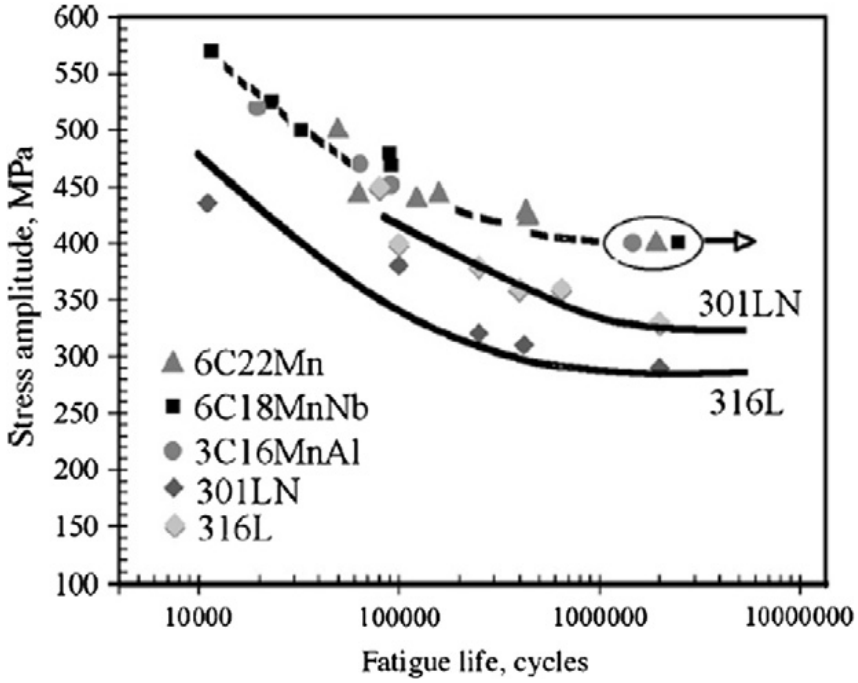

Fig. 1.6: Stress amplitude vs. fatigue life of different grade TWIP steels determined under bending fatigue experiment. Two commercial stainless steels, 301LN and 316L (as annealed) are also included for comparison (Hamada et al., 2009).

It is quite clear from Fig. 1.6 that the fatigue limit of the mentioned TWIP steels is only about 400 MPa, while their tensile strength is about 1000 MPa, and therefore, the interpretation of their deformation behaviour is in fact quite fascinating. It is well known that TWIP steels possesses a high tensile strength due to presence of intense twinning in the deformation microstructures, but the same mechanism does not occur

during cyclic loading, and which prevent the TWIP steel to reach the fatigue limits above 400 MPa. Niendorf et al. (2009) reported that no new twin nucleation occurs even at low cycle fatigue (LCF) with strain amplitudes up to 0.6%, while investigating the deformation microstructures of high-Mn steels. The TEM investigations of the specimens ahead of any stable fatigue crack growth also further advocate towards the fact that the accumulated cyclic strains are not sufficient to activate new twin nucleation, although thickening of the pre-existing twins were reported (Niendorf et al., 2010). The possible reasons of the pre-existing twin thickening could be understood in terms of decrease in dislocation density under cyclic loading (Niendorf et al., 2009; 2010). In absence of deformation induced twin under cyclic loading causes a low susceptibility to fatigue crack growth in TWIP steel, and fatigue crack embryos nucleated at various lattice sites, such as: intersections of slip bands, grain boundaries, annealing twin boundaries and then it propagate along a trans-granular path (Hamada et al., 2009; 2010).

The presence of deformation twins in the LCF behaviour of Fe–23Mn–0.6C (wt%) TWIP steel was reported by Wu et al. (2014), and they also suggest that the cyclic hardening is mainly attributed to the occurrence of deformation twins and persistent slip band (PSB) in the deformation microstructures. Although, deformation twins may appear in the LCF condition of TWIP steels (Wu et al., 2014), but most of the investigations related to HCF loading of TWIP steels suggest that deformation twins remain absent in the deformation microstructures (Hamada et al., 2009; Seo et al., 2017). However, Karjalainen et al. (2012) reported the occurrence of deformation twins under HCF loading while investigating the cyclic deformation microstructures of Fe–16Mn–1.5Al–0.3C steel, and found that not only twins, but the deformation microstructure also comprises of several dislocation substructures, wide stacking faults, planar dislocation arrays and dislocation tangles. Therefore, the deformation microstructures and their exact influence to the strengthening mechanisms that control the cyclic deformation behaviour of TWIP steels are still an open challenge to the scientific community.

1.4 Factors influencing the deformation behaviour of fcc metals/alloys

It is clearly evident from the above discussion (i.e., §1.3) that the evolution of different deformation microstructures due to imposed plastic strain not only depend on the deformation process, but it also strongly influenced by some other microstructural parameters related to the metals/alloys. In this section we will briefly discuss several microstructural parameters and their influence on the corresponding deformation mechanism of different grades steels, specifically for high and/or medium-Mn steels.

1.4.1 Stacking fault energy (SFE)

Among several microstructural parameters that have strong influence on the deformation behaviour of any metals/alloys is SFE of the materials, and it is quite possible to predict the deformation microstructure only by knowing the SFE of the material. Depending on the SFE value of the material on can predict the active deformation mechanisms of the steels, such as: TRIP, TWIP, and MBIP etc., which basically control the mechanical properties of the metals/alloys. However, it is still unclear that why a threshold SFE value is essential to activate different mechanisms, although the strain induced twinning i.e. TWIP effect appears to be related to the suppression of the athermal $\gamma \rightarrow \varepsilon$ martensitic transformation. Being an essential parameter, the experimental determination of SFE obtains a considerable attention by the scientists for different grade steels, and it is found that the high-Mn steels with a fully stable austenitic microstructures have a SFE value that lies in the range of 20-30 mJ/m^2 or more (Schumann, 1972; Alder *et al*., 1986; Mindownik, 1998; Yakubtsov *et al*., 1999; Allain *et al*., 2004a; Idrissi *et al*., 2010; Pierce *et al*., 2012; 2014;).

It is well accepted that the critical SFE regime to observe TWIP effect in high and/or medium-Mn steels is still a debated issue, and there is a slight difference in the range of SFE value, which not only depend on the experimentally obtained scatter SFE value but also strongly influenced by the alloying compositions. Frommeyer *et al*. (2003) suggested that TWIP effect in a stable austenite can be observed if the SFE value is larger than ~ 25 mJ/m^2, while Allain *et al*. (2004b) presented a narrower range for SFE mediated twinning. Furthermore, Dumay *et al*. (2008) reported that deformation twinning tends to disappear below SFE ~18 mJ/m^2, and it is replaced by ε-martensite platelets formation, while investigating copper containing Fe–Mn–C grade steels.

However, both Jin & Lee (2009) and De Cooman *et al*. (2011) reported almost similar kind of SFE value for Fe-18Mn-0.6C-1.5Al alloy, although their suggested SFE value for activation of deformation twining approximately differs by ~ 3 mJ/m^2.

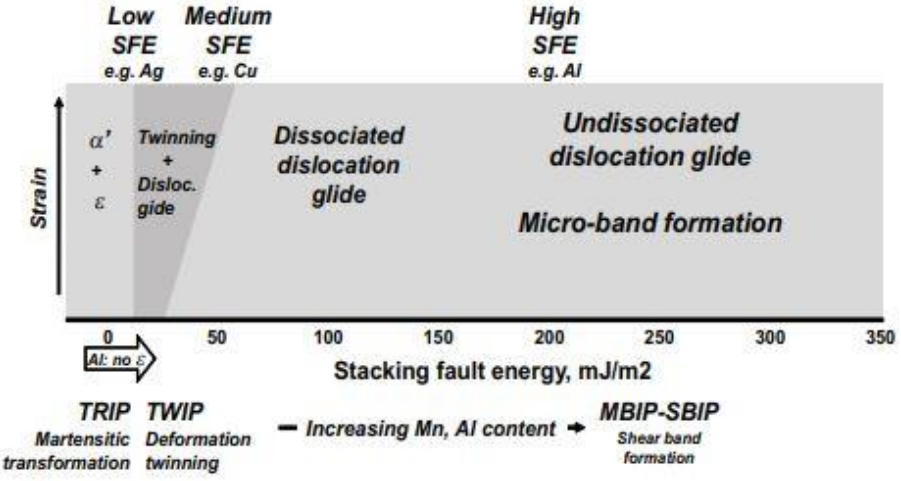

Fig. 1.7: Schematic showing the influence of SFE on the deformation mechanisms of f.c.c metals/alloys (De Cooman et al., 2011).

Additionally, the influence of SFE on the deformation microstructure evolution as well as its RT strain-hardening behaviour of three (Fe-22/25/28Mn-3Al-3Si) TRIP/TWIP steels were investigated by Pierce *et al*. (2015), and they suggested that the SFE of the alloy increased from 15 to 39 mJ/m^2 as the Mn content the increase from 22 to 28 (in wt.%). They also reported that best combination of UTS and total elongation could be obtained for the studied alloys only for the SFE value lies in the range of 15-39 mJ/m^2, and it significantly decreases when SFE value exceeds ~ 39 mJ/m^2. Such inferior mechanical properties above the SFE value of ~ 39 mJ/m^2 could be understood in terms of decrease in the incidence of mechanical twinning in the deformation microstructure. It was also observed that the deformation microstructure of Fe-25Mn-3Al-3Si steel having a SFE value of ~ 21 mJ/m^2 mostly comprises of dislocation substructure that exhibited both planar as well as wavy slip characteristics, whereas, the dislocation cross slip enhances in case of Fe-28Mn-3Al-3Si having a higher SFE ~ 39 mJ/m^2, and which reduce the work-hardening rate in comparison to the lower SFE alloys. In this context, the influence of SFE on the deformation mechanisms of different

metals/alloys can be summarize as presented in Fig. 1.7, which clearly indicate that the activation of different deformation mechanism in terms of the SFE of the materials. Fig. 1.7 reveals that as the SFE increases from low to medium range then the deformation mechanism also changes from TRIP to TWIP, and when the SFE is very high then the material mostly deforms through micro-band or shear band induced plasticity mechanism (MBIP or SBIP). Since the SFE is a very important parameter in governing the deformation mechanism is fcc metals and alloys, thus a comprehensive description on the various methods available for SFE estimation is provided in §3.

1.4.2 Grain size

It is well established that the grain size of any material is closely related to its mechanical behaviour and therefore, scientists suggest the grain refinement technique to control the deformation microstructure and thereby controlling the strength of the material, while keeping its chemical compositions same (Ueji *et al*., 2008). However, the information concerning the influence of grain size on the mechanical properties and the underlying deformation mechanism of fcc metals/alloys having low SFE, such as: high-Mn steels is still limited. Some of the investigations related to the grain size refinement of high-Mn steels suggest that the grain size refinement increases the threshold stress, i.e. initial yield while some fraction of its ductility is reduced (Scott *et al*., 2005; Ueji *et al*., 2008). In 2009, De Cooman *et al*. (2009) stated that due the increment in grain size, the YS as well as UTS of high-Mn steel decreases simultaneously according to Hall-Petch relationship, while the ductility of the steel increases. Additionally, it is also shown that the Hall-Petch parameter does not depend on the mode of deformation of the high-Mn steel, and therefore it possesses almost same value for deformation twins as well as dislocation glide dominated deformation microstructures (Gutierrez-Urrutia *et al*., 2010).

Furthermore, Gutierrez-Urrutia & Raabe (2012a) indicated that the formation of different dislocation substructures strongly depends on the grain size, and which in turn significantly influences the twinning tendency of high-Mn steels. However, this observation doesn't valid in the steels having a grain size of μm range in which the influence of grain size to suppress deformation twinning is minor, at least for the alloys with chemical composition of Fe-22Mn-0.6C (Gutierrez-Urrutia *et al*., 2010). Ueji *et al.* (2008) reported that the fine-grained (grain size, $d = 1.8\ \mu m$) Fe-31Mn-3Al-3Si

high-Mn steel demonstrate a high strength with adequate ductility, and suggest that the large ductility lies not only on the formation of deformation twinning but also the suppression of dynamic recovery due to its low SFE. Some of the investigations related to the low SFE materials also reported that the formation of deformation twin as well as martensitic transformation may completely inhibited due to the fine grain size (El-Danaf *et al*., 1999; Asgari, 2004; Mohammed *et al*., 2007). In case of high-Mn Fe-Mn-Al-C austenitic steel, Yoo & Park (2008) suggested that continuous increment in the SHR along with its the exceptionally high elongation is mainly attributed to the formation of microbands consisting of geometrically necessary dislocations, i.e. they report the occurrence of MBIP effect. In general, the microbands observed in the austenitic steel are crystallographic in nature and they run throughout the grains, and thus the length scale of the observed microbands mostly have the same order as the austenite grain size (Wilsdorf, 1989; Hughes, 1993). Therefore, it is quite plausible to understand that strain hardening by MBIP effect may saturate early in case of fine-grained steel as compared to the coarse-grained steel of the same grade steels.

1.4.3 Grain orientation

It is well known that when a bulk material is deformed under monotonic and/or cyclic deformation, then the influence of the imposed plastic strain is not same for all the grains of the material, in fact, it varies from grain to grain and that variation depends on the Schmid factor associated to the grains. Interestingly, the Schmid factor of a grain strongly correlated to the orientation of the grain with respect to the direction of the applied plastic strain, and therefore, the grain orientation should play an important role to understand the deformation mechanism of any material/alloys. In literatures, it is reported that the initial grain orientation has a pronounced influence on deformation twinning nucleation and crystallographic texture development (Kuprekova *et al*., 2008; Gutierrez-Urrutia *et al.,* 2010; Sato *et al*., 2011). Several studies also convey different explanations regarding the influence of grain orientation on deformation twinning, and three of such different explanations are summarized schematically in Fig. 1.8.

Gutierrez-Urrutia & Raabe (2011) suggested that the influence of grain orientation that observed at low strain is mainly governed by the relative value of the Schmid factor associated to the respective grains, and later this kind of observation was also confirmed by Sato *et al*. (2011) while investigating the deformation

microstructures of high-Mn steels. Both of them also proposed that the occurrence of

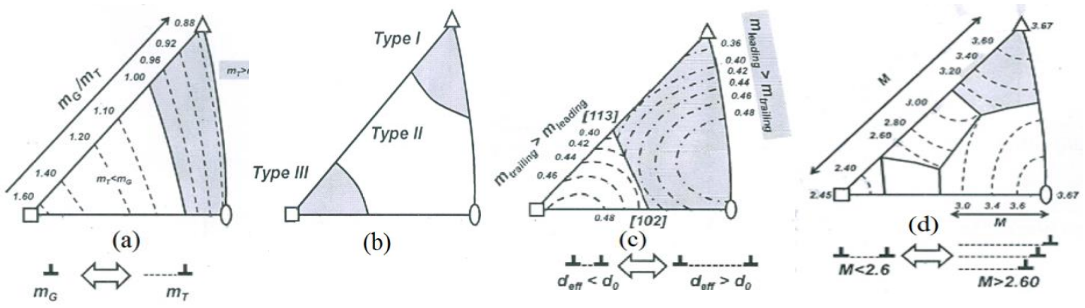

Fig. 1.8: (a) Schematic indicating the influence of grain orientation on the formation of deformation twin according to (Gutierrez-Urrutia & Raabe, 2011; Sato *et al*., 2011). (b) The type I and type II grain behave as expected on the basis of their Schmid factor (c) Schematic showing the effect of grain orientation on the formation of deformation twin according to Kireeva and Chemlyakov (Kuprekova *et al*., 2008; Kireeva & Chemlyakov, 2009;) (d) Schematic illustrating the effect of grain orientation on deformation twin according to (Beladi *et al*., 2011).

deformation twins in the microstructures is possible only when the resolved shear stress for twinning (τ_{crss}) is less than the critical resolved shear stress associated to dislocations gliding (τ_G), i.e:

$$(\tau_c)_{twin} = \tau_{crss} = m_T \sigma_A < \tau_G = m_G \sigma_A \rightarrow m_T < m_G \qquad (1.2)$$

where, Schmid factor is the product of the cosines of the angles between the direction of the applied stress (σ_A) and the slip plane normal, which depends on the direction of shear for a perfect dislocation (m_G) or a partial dislocation (m_T). In this context it must be mentioned here that scientists have reached to the above-mentioned conclusions only by analysing the uniaxial tensile deformation of high-Mn steels.

According to Gutierrez-Urrutia & Raabe (2012b), the Schmid law of orientation dependence on slip and twinning does not hold in practice under the tensile deformation of Fe-22Mn-0.6C steel. They also reported that the only type I grains were favourably oriented for twinning as their orientation are very close to $\langle 111 \rangle // t_d$, while the dislocation glide is favourable in type III grains only due their orientations, which are close to $\langle 100 \rangle // t_d$. Furthermore, the type II grains covering a wide range of orientations are unfavourable for twinning based on their Schmid factor, but it also contains deformation twins. However, Beladi *et al*. (2011) found that the grains with an orientation close to the Goss and Cube orientation were free of mechanical twins,

while those having an orientation close to the Brass or Cu, were twinned. Additionally, Beladi *et al*. (2011) also mentioned that the twin nucleation and growth requires the activation of multiple slip systems and the presence of a high stress sites in the deformation microstructures resulting from dislocation pile-ups. Therefore, it is quite clear from the aforementioned discussion that the activation of different deformation mechanism in a grain strongly influenced by the orientation of that grain with respect to the direction of the imposed plastic strain.

1.4.4 Deformation temperature

In general, as the deformation temperature increases the strength as well as elongation of metals/alloys decreases, and therefore it is expected that the deformation temperature must have significant influence on the evolution of deformation microstructures of metals/alloys. Wang *et al*. (2009) reported that deformation twinning is the dominant in Fe-25Mn-3Si-3Al steel for a deformation temperature range of $25℃ \leq T \leq 100℃$, while dislocation slip dominates over deformation twining at an elevated temperature of $T \geq 400℃$. They also suggest that the studied steel possesses superior mechanical properties in the relatively low temperatures range due to the formation of deformation twins, which behave as obstacles to dislocation movement in the deformation microstructure. Tang et al., (2018) also reported a similar kind of observations while investigating the influence of deformation temperatures on the microstructure evolution and mechanical properties of cold-rolled Fe-18Mn-3Al-3Si-0.03C high-Mn steel. The studied steel possesses a UTS of 905 MPa along with a TEL of 55% at RT, but UTS and TEL both decreases monotonously to 325 MPa and 36%, respectively, as the deformation temperature increases to 400 °C. They also claimed that deformation mechanism of the high-Mn steel at RT is mostly controlled by both the TRIP and TWIP effect, whereas, both of these mechanisms were inhibited at an elevated temperature and only dislocation glide remain activated as deformation mechanism during the plastic deformation.

However, Yoo *et al*. (2009) reported an exceptional situation i.e., the elongation does not decrease with increasing deformation temperature while investigating high-Mn steel with highly enriched Al and C contents. They reported that the YS are temperature sensitive in between $150 - 450℃$, and the UTS value

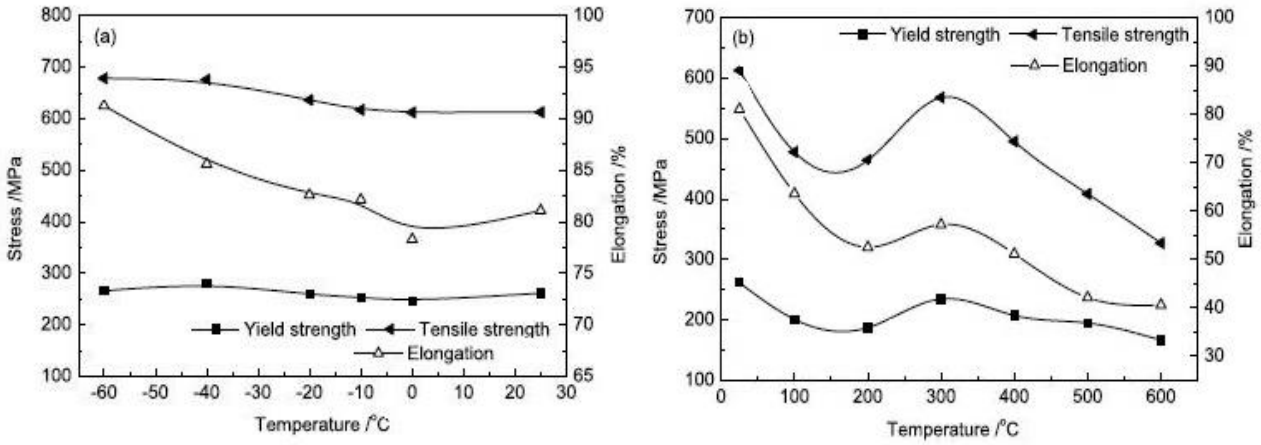

Fig. 1.9: Variations of the YS, tensile strength and elongation of Fe-23Mn-2Al-0.2C high-Mn steel with lower (a) and higher (b) deformation temperatures (Qin *et al*., 2011).

decrease as the deformation temperature increases. It is expected that the TEL decreases at elevated temperature for all over the deformation temperature range, but a higher TEL value was reported only at 300℃. Yoo et al. (2009) explained such anomalies in terms of the serrated flow occurring at 300℃, and also confirmed that the serrations are primarily attributed to interaction between dislocations-interstitial atoms rather than interaction between dislocations-substitutional atoms. Another study related to the influence of deformation temperature ranging from $-60℃ \leq T \leq 600℃$ on the tensile deformation behavior of Fe-23Mn-2Al-0.2C high-Mn steel are presented in the Fig. 1.9, which indicates that both strength as well as elongation first decrease then increases with temperature increment (Qin et al., 2011). They also revealed that the dominated deformation mechanisms of the steel change from twining to dislocation gliding as deformation temperature increased from $-60℃ \leq T \leq 600℃$, and only dislocations and dislocation cells appear in the microstructure at 600℃. However, Fig. 1.9 indicates that superior mechanical properties of Fe-23Mn-2Al-0.2C alloy can be obtained at two the deformation temperature, RT and 300℃.

1.4.5 Local deformation microstructure

Besides the above-mentioned factors, the deformation mechanism related to any grain also strongly influenced by its surrounding local microstructures, although its influence on the deformation behaviour of bulk materials is not always recognizable, but it always

presents in the deformation microstructure of the metals/alloys (Estrin and Kubin, 1986). At first, Adler et al. (1986) indicate that any local lattice distortion may contribute to the strengthening of any material. For a SF region, the local fcc stacking sequence will change to hcp stacking sequence and thereby create a local lattice distortion, which could produce strengthening effect in the Hadfield steels (Adler et al., 1986). Furthermore, Heinz and Neumann (1990) reported that the presence of elastic anisotropy in the lattice produces different local stress concentration at different lattice sites, and which plays a crucial role in controlling the deformation mechanism of the material. While investigating the HCF behaviour of an austenitic steel, they observed that the dislocation glide was enhanced significantly at grain boundaries due to the occurrence of local stress concentration across the grain boundaries, and therefore instate of grain boundaries the crack initiation starts only at the twin boundaries (Heinz and Neumann, 1990). A similar kind of observation was also reported for different types of materials, such as: nickel-based super alloys (Miao et al., 2009; 2012), stainless steels (Mineur et al, 2000) in which crack initiated only along twin boundaries during LCF. Additionally, Timokhina et al. (2004) also highlighted that the influence of local deformation microstructures plays a critical role to stabilize the austenite against phase transformation, and thereby control the cyclic behaviour of TRIP steels.

In case of high-Mn steels, Lee et al. (2011) have reported that the Mn and C atoms may produces a local ordering or clustering of Mn-C atoms, which behave as more effective obstacle for dislocation movement than individual Mn and C atoms, and thereby enhance the high strain hardening rate. Furthermore, the interaction between Mn-C clusters (or dipoles) and dislocations are also believed to be responsible for the occurrence of tee dynamic strain aging (DSA) in the flow-stress behaviour Hadfield steels. Dastur et al. (1981) suggested that the dislocations are pinned by Mn-C clusters which reorientated themselves according to the stress field of dislocation core and causes dislocation pile-up. However, the pinning strength of dislocation is not strong enough to completely stop the dislocation movements, and therefore as the pinned dislocations are released and propagate further in the microstructure DSA occurs. A similar kind of observation was also reported for TWIP steels during the studies related to the deformation behaviour of Fe-18Mn-0.6C TWIP steels (Chen et al., 2007). It is important to mention here that the occurrence of precipitates in a grain can be treated as local microstructural defects and that also have significant influence on the

deformation mechanism of the metals/alloys (Christian et al., 1995; Chateau et al., 2010; Yen et al., 2012; Gwon et al, 2017).

1.5 A review on SFE of high/medium-Mn steels

From the above discussions it is clear that the mechanical properties of any materials under different deformation conditions strongly depends on their deformation behaviour and its associated mechanisms. Interestingly, the excellent mechanical properties of the high/medium-Mn steels are also related to various deformation mechanisms such as: TRIP, TWIP, dislocation slip/glide etc., and which significantly influenced by a crucial microstructural parameter, SFE of the steels (§1.4). Only from the knowledge of SFE one can predict the possible deformation mechanisms that may activate during plastic deformation of the steels. Therefore, significant efforts have been made towards the SFE estimation of high/medium-Mn steels and as a result of which scientists have developed both, computational and experimental SFE estimation methods. It must be mentioned here that there are basically two computational approaches, such as: thermodynamic approach and ab-initio approach. The thermodynamic approach is based on the Olson-Cohen model (Olson et al., 1976) for the intrinsic stacking fault in fcc metals/alloys, whereas the ab-initio approach basically estimates the intrinsic energy barriers in the generalized stacking fault energy (GSFE) surface, which is originally proposed by Vitek (Vitek, 1968; 1970).

Moreover, the SFE is treated as an intrinsic material property in the computational approaches and the influences of any other defects present in the microstructures were neglected, and hence it is called intrinsic SFE. The intrinsic SFE is the SFE of the material while no other defects are present except an infinitely long SF, but in reality, this is not possible and therefore, intrinsic SFE can't be determined in reality by experimental measurement. The SFE estimated experimentally is known as effective SFE, which is basically nothing but a modified value of intrinsic SFE, and the modification directly correlated to the occurrence of other microstructural defects in the microstructures. However, there are several studies related to the estimation of effective SFE, which have reported a scatter effective SFE value for the same high/medium-Mn alloys while measured with different experimental techniques (Kim et al., 2011; Kim and De Cooman, 2011; Jin and Lee, 2012; Jeong et al., 2012). The

Table 1: Effective SFE and corresponding deformation mechanisms/microstructures of high/medium-Mn steels.

Alloys	Effective SFE in mJm^{-2}	Deformation mechanism/microstructure	References
Fe–20Mn–1.2C	15[a]	Deformation twin, and highly dense sessile Frank dislocations within the twins.	Idrissi et al., (2010)
Fe–18Mn–0.6C	(13 ± 3)[a]		Kim et al., (2011)
Fe–18Mn–0Al–0.6C	(17 ± 3)[b]	Primary and secondary twin formation and weakened DSA by suppression of cementite precipitation	Jin and Lee, (2012)
Fe–18Mn–0Al–0.6C	(20 ± 4)[c]	Planar glide of dislocation and dynamic Hall–Petch effects	Jeong et al. (2012)
Fe–18Mn–1.5Al–0.6C	(30 ± 10) (WBDF)[a]		Kim and De Cooman (2011)
Fe–18Mn–1.5Al–0.6C	26.4 (node)[a]		Kim and De Cooman (2011)
Fe-25Mn-0.15C-0.6Al	7.75[b]	ε_{hcp}-martensite	Tian et al. (2008)
Fe-19Mn-5Cr-0.25C-1Al	20.9 (node)[a]	Deformation twin, α'-martensite and ε_{hcp}-martensite	Oh et al., (1995)
Fe–26Mn–1Al–0.14C	(60 ± 5.5)[b]	Taylor lattice, dislocation substructures, tangles, cell	Das et al., (2021)
Fe-8%Mn-0.4%C-3%Al-2%Si-(0–0.2)%V	20	TRIP and TWIP	Lee and De Cooman (2015)

[a]TEM, [b]XRD, [c]Neutron diffraction

experimentally estimated effective SFE value and the corresponding active deformation mechanisms/microstructure of high/medium-Mn steels are summarized in Table 1. It is also important to mention here that the SFE of these high/medium-Mn steels not only significantly influenced by the presence of other microstructural defects but also it

depends on several parameters, which have been discussed briefly in the following subsections.

1.5.1 Chemical compositions

At first, Schumann (1972) considered the compositional weight percentage of C and Mn as a variable to achieve fcc phase stability at room temperature, while investigating the mechanical properties of Fe-Mn-C alloys, and after observing the deformation microstructure he concluded that there is a characteristic boundary line between two regions in the Mn-C composition plane. He has also reported that the stable compositions deformed by dislocation glide and twinning while the unstable compositions leading to the deformation-induced phase formation, and these can be understood in terms of change in SFE of the compositions. Later, several studies also suggest the same while investigating the influence of different compositional elements with different weight percentage. Lee and Choi (2000) suggest that the SFE

Table 2: Influence of alloying element on the SFE of high/medium-Mn steels

Elements	Influence on SFE	References
Mn	The SFE and Mn content dependency is nonlinear in nature. SFE decreases with addition of Mn in the range of 3-12 wt.% Mn, and at lower Mn content (< 7- 8wt.% Mn) SFE decreases relatively faster than higher Mn content (>8 wt.%). Lowest SFE is possible for the range of 10-16 wt. %, and then SFE increases as the Mn content exceeds >16 wt. %.	Lee and Choi (2000); Dai et al., (2002); Zambrano *et al*., (2016).
Al	SFE often drastically increases by aluminium additions. In general, SFE increases monotonously at least 7mJ/m^2 with 1% Al of addition.	Chen et al., (1993); Tian et al., (2009); Zambrano *et al*., (2016)

Si	Si addition generally reduces the SFE of high/medium-Mn steels. However, the influence of Si on SFE is stronger when the aluminium content high as compared to the low aluminium contents alloys.	Tian et al., (2009); Lehnhoff et al. (2014); Zambrano *et al*., (2016)
C	There is currently some confusion regarding the relationship between SFE and C content. Several earlier research indicated very different results, such as SFE can be increased, decreased or have a little influence due to C addition. It has recently been stated that its effects depend on the additions of Al and Mn.	Brofman et al., (1978); Peng et al., (2014); Zambrano *et al*., (2016)

in Fe–Mn binary alloys increases with the increment of the manganese, whereas, Dai et al. (2002) reported the same for austenitic steels. The influences of silicon addition on SFE of austenitic stainless steels has been studied by Lehnhoff et al. (2014), and suggest that SFE decrease with Si addition, which was also confirmed in other studies (Dumay et al., 2008; Tian et al., 2009). The influence of commonly added alloying elements such as: Mn, Al, Si, and C on the SFE of austenitic phase in high/medium-Mn steels are summarized in Table 2.

1.5.2 Temperature

Temperature is another crucial factor that significantly affects the SFE of high/medium-Mn alloys. In 1971, Latanision first suggest that the SFE is directly related to temperature while thoroughly investigating the SFE of austenitic alloys over a large temperature range of 25°C to 325°C, and also reported that as the temperature increases the dislocation node size decrease (Latanision et al., 1971). Later, these findings are also confirmed by the other investigations related to the influence of temperature on SFE of high/Mn alloys (Remy, 1977; Remy et al., 1978). It is also reported that as deformation temperature increases the TRIP and TWIP effects disappears for 316L austenitic stainless steels, and the non-existence of TRIP and TWIP effect can be explained in terms of increment of SFE of austenite phase at higher temperatures.

Another study shows that the SFE of Fe-25Mn-3Si-3Al steel increases from 21 mJ/m^2 to 76 mJ/m^2 as the deformation temperature increases for 25℃ to 400℃ (Wang et al., 2009).

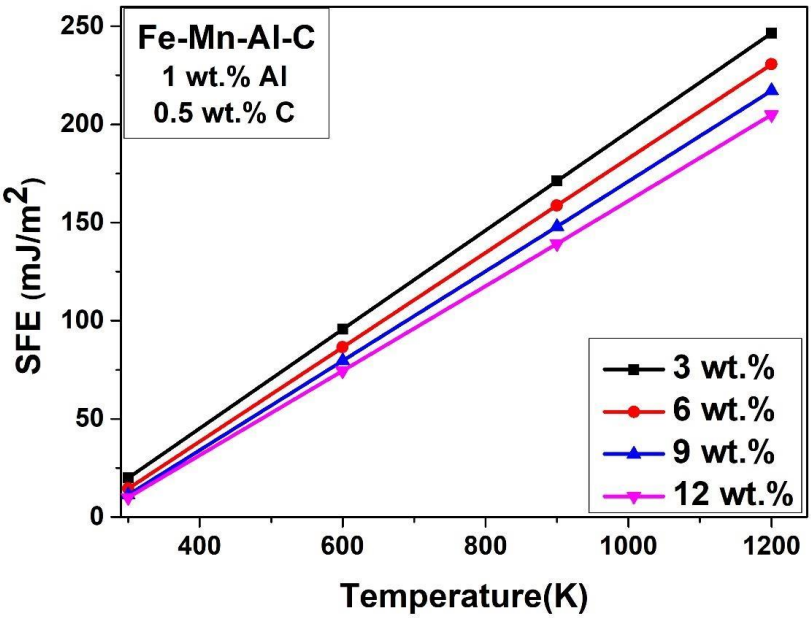

Fig. 1.10: Temperature dependent SFE map of Fe-Mn-Al-C steels (Zambrano *et al.*, 2016).

An opposite trend of SFE with temperature is also recently reported i.e. SFE decreases as temperature increases while predicting the SFE of AHSS using ab-initio calculations during an investigations related to the nano-diffusion effect (Suzuki segregation) of carbon in the stacking faults at cryogenic temperature (Hickel et al., 2014). Interestingly, this opposite trend is also confirmed using TEM investigations and found that the dissociation width of partial dislocation increases as temperature increases starting from cryogenic temperature (Hickel et al., 2014). It must be mentioned here that this investigation also suggests that the SFE value at different locations of metals/alloys i.e., the local SFE value changes drastically in comparison with the SFE value obtained from the global chemical composition of the alloys. Therefore, Zambrano et al. (2016) considered only the relation between global chemical compositions and SFE value in his SFE prediction thermodynamic model and neglect any compositional interaction to the local SFE value. The temperature dependency of SFE of in Fe-XMn-1Al-0.5C (wt.%) alloy is presented in Fig. 1.10, which clearly indicates that SFE monotonously increases for the medium-Mn steels as the temperature increases.

1.5.3 Grain size

Although the influence of grain size on SFE of high/medium-Mn steels are not clear yet, but there are few reports which collectively suggest that the SFE of the austenitic steels have an inverse relationship with the grain size of the steels. Jun and Choi (1998) first reported that the SFE of Fe-18Mn (wt.%) alloy increases exponentially as the austenite grain size decreases below 35 μm, whereas, SFE decreases slightly while grain size exceeds 35 μm. Few years later, A similar kind of observation was also reported by Lee and Choi (2000) while investigating the deformation behaviour of Fe-Mn alloy with different Mn content having a grain size of 5 μm to 150 μm. They also reported that finer or smaller austenite grain size promotes the suppression of TRIP or TWIP effects in comparison to that revealed by coarser grain size due to SFE increment of austenite. At RT, the relationship between the SFE and austenite grain size for high/medium-Mn steels is depicted in Fig.1.11, which clearly reveals that SFE decreases rapidly as austenite grain size increases (< 50 μm), however, there is no appreciable decrease in SFE with austenite grain size for austenite grain size above 50 μm (Zambrano *et al*., 2016).

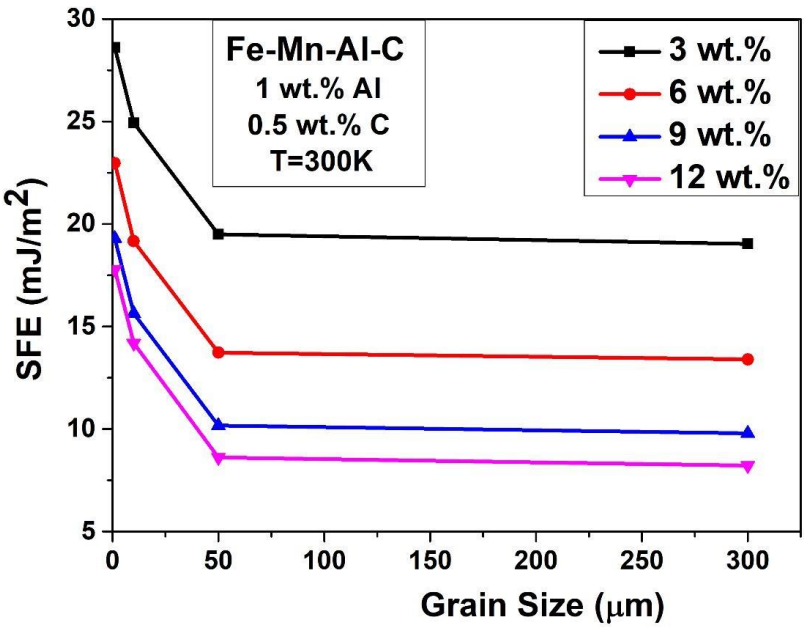

Fig. 1.11: Grain size dependent SFE map of Fe-Mn-Al-C steels (Zambrano *et al*., 2016).

1.6 Aims and scopes of the dissertation

The previous discussions related to the interpretation of deformation behaviour of high-Mn austenitic steels and its corresponding deformation mechanisms have clearly recognized that TWIP effect play an importance role in revealing a high strength and superior plasticity, which is essential for lightweight automotive structures and components production (De Cooman *et al*., 2018). In general, there are basically three types of high-Mn steels, namely, Fe-Mn-C (Idrissi *et al*., 2010), Fe-Mn-Al-C (Jin & Lee, 2012) and Fe-Mn-Si-Al (Idrissi *et al*., 2013), which have been investigated extensively till now, and interestingly, Fe-Mn-Al-C remained the most investigated steel grade as compared to the other two steel grade due to its good strength and ductility combination. The superior mechanical properties of Fe-Mn-Al-C grade steel under monotonous deformation are quite understandable in terms of deformation twin formations in the microstructures, but its role in case of cyclic deformation is sill under debate and need further investigations (De Cooman *et al*., 2018).

The early works related to the cyclic deformation of high-Mn steels mainly attributed to the modest fatigue properties of TWIP steels due the absence of deformation twin (Hamada et al., 2009; 2010; Niendorf et al., 2010), while the reasons for this are unknown (Benito et al., 2016). Many studies reported that the grain refinement as an effective method to improve the fatigue limit and in fatigue resistance in high-Mn steels (Hamada et al., 2010; Shao et al., 2019). Most of the investigations on high-Mn steels in last decade has focused primarily on monotonous deformation (De Cooman et al., 2018), while the cyclic deformation behavior is still not properly understood, and only a few studies reported a detailed microstructure evolution during cyclic deformation of these steels (Karjalainen et al., 2012; Wang et al., 2015). Wu et al. (2014) suggest that the cyclic hardening in the LCF behaviour of Fe–23Mn–0.6C (wt%) is mainly attributed to the occurrence of deformation twins and persistent slip band (PSB) in the deformation microstructures. Although, deformation twins may appear in the LCF condition of high-Mn steels (Wu et al., 2014), but most of the investigations related to HCF loading of high-Mn steels indicate that deformation twins remain absent in the deformation microstructures (Hamada et al., 2009; Seo et al., 2017). However, the occurrence of deformation twins under HCF loading of Fe–16Mn–1.5Al–0.3C steel was also reported (Karjalainen et al., 2012), although the critical role of deformation twin in cyclic deformation of high-Mn steels are not critically inspected.

Additionally, it is well known that dislocation activity is fundamental to any plastic deformation, but the occurrence of different types of dislocation substructures in the deformation microstructures of high-Mn steels under cyclic deformation are not adequately investigated. Several studies related to the cyclic deformation microstructure of high-Mn steels with different grain size reported that the deformation microstructures comprise of different dislocation substructures, slip bands, wide stacking faults, planar dislocation arrays and dislocation tangles (Hamada et al., 2010; Karjalainen et al., 2012). However, their exact influence on the different strengthening mechanisms which control the cyclic deformation behaviour of high-Mn steels are still an open challenge to the scientific community. Most of the studies related to the cyclic deformation of TWIP steels were aimed at understanding the mechanical properties of the steels, while their cyclic deformation behavior in terms of microstructural parameters is still poorly understood. In a part of this study, we will investigate the microstructural evolution in a coarse-grained (CG) and graded grain high-Mn steel deformed under high-cycle bending fatigue, and the aim is to critically interpret the evolution of cyclic deformation microstructure in relation to its cyclic response through a combination of EBSD, TEM and the quantitative microstructural information such as: dislocation density, effective SFE, planar fault probabilities etc. obtained from XRD analysis.

Another part of this study deal with the active deformation mechanisms of medium-Mn (<12 wt%) steel deformed under uniaxial monotonous loading. Recently, medium-Mn lightweight steels are also getting more attentions due to low production cost, corrosion resistant property and superior strength–ductility balance comparable to high-Mn steels (Kannan et al., 2008; Allam et al, 2019). There are few studies related to the medium-Mn steels, which suggest that different microalloying elements such as: Cr, Cu, Si, Al, V, Ni, N can be added in single or combined to enhance the corrosion resistance with in a desirable range of SFE, which basically determines the austenite stability and also controls the activation of the secondary deformation mechanisms, namely, TWIP, TRIP etc. addition to primary deformation mechanism i.e. dislocation slip (Dumay et al., 2008; Kannan et al., 2008; Dieudonné et al., 2014; Allam et al, 2019). It is also reported that different alloying concept strongly affects the yield strength due to activation of different deformation mechanisms, such as: Ashby–

Orowan effect, Hall–Petch effect, solid–solution, and dislocation strengthening (Allam et al, 2019).

It is well accepted that the formation of deformation twin in the deformation microstructure significantly influence the mechanical properties, and also believed that deformation twin is initiated from the pre-existing dislocation configurations that generally dissociate into multi-layered SF structures forming a three-layer twin nucleus (Christian et al., 1995). There are several classical dislocation-based models of heterogeneous twin nucleation (Ookawa, 1957; Venables, 1974; Christian et al., 1995; Niewczas et al., 2002), and depending on the different length scales, i.e. the grain sizes various twinning mechanisms are activated (Christian et al., 1995; Zhu et al., 2012). For instance, the classical twinning methods involving dissociations of $\frac{a}{2}\langle 110\rangle$ perfect dislocations are generally applicable in the grain size range well above the nano crystalline (NC) regime (Venables, 1961; 1964; Mahajan et al., 1973; Niewczas et al., 2002), while various non-classical twinning mechanisms involving emission of Shockley partial dislocations (SPDs) from the GBs (Yamakov et al.,2001; Zhu et al., 2012), alternated SF pair (Wang et al., 2017), etc. are activated in the NC regime. However, Yen et al. (2012) recently reported that a non-classical alternated SF pair twinning mechanism could be activated in grain sizes well above the NC regime.

Furthermore, it is important to mention here that the twin nucleation also significantly influenced by several interrelated variables, namely, composition, temperature, strain rate, pre-strain, grain size, grain orientation, precipitates, etc. (Christian et al., 1995). Although, the influence of the parameters in controlling the twin nucleation are widely reported, but the influence of precipitates is still poorly understood due to some conflicting reports. McHargue et al. (1963) reported the suppression of twinning in Ti-Zr alloys due to presence of precipitates, while Mahajan et al. (1980) observed micro twins during precipitation hardening in spinodally-decomposed Fe-Cr-Co alloy. Generally, the presence of any precipitates in the matrix creates a lattice mismatch between the precipitate and the matrix, and this lattice mismatch produce a local stress field in the surrounding matrix (Tirry et al., 2005). In this part of the study, we focus on the role of local stress field associated to the precipitates on the twinning tendency of a precipitation hardened medium-Mn steel containing V (C, N) precipitates. The objective of study is to capture the fate of

deformation twinning, at an early stage of deformation in presence of local microstructural defects i.e., precipitates, and also to identify the underlying twinning mechanism in the studied medium-Mn steel.

References

Adler, P., Olson, G., Owen, W. (1986) Metall. Mater. Trans. A 17, 1725-1737.

Allam, T., Guo, X., Sevsek, S., Lipińska-Chwałek, M., Hamada, A., Ahmed, E., Bleck, W. (2019) *Metals* **9(6)**, 705.

Allain, S, Chateau, J. P., Bouaziz, O., Migot, S. & Guelton, N. (2004a). Mater.Sci. Eng. A. 387-389, 143-147.

Allain, S., Chateau J. P., Bouaziz, O., Migot, S. & Guelton N. (2004b). *Mater.Sci. Eng. A.* **387-389**, 158-162.

Armstrong, R. W. (2014) *Mater. Trans.* **55**, 2-12.

Benito, J. A., Cobo, R., Lei, W., Calvo, J., Cabrera, J. M. (2016) *Mater. Sci. Eng. A* **655**, 310–320.

Beladi, H., Timokhina, I. B., Estrin, Y., Kim, J., De Cooman, B. C. & Kim S. K. (2011). *Acta Mater*. **59**, 7787-7799.

Bhadeshia, H. K. D. H. (2010) *Proc. R. Soc. Lond.* A. **466**, 3-18.

Bouaziz, O., Allain, S., Scott, C., Cugy, P., Barbier, D. (2011) *Curr. Opin. Solid. St. M*. **15,** 141-168.

Brofman, J., Ansell, G. S. (1978) Metallurg. Trans. A **9(6)**, 879-881.

Chen, F. C., Chou, C. P., Li, P., and Chu, S. L. (1993) *Mater. Sci. Eng. A,* **160(2)**, 261–270.

Chen, J., Dong, F., Liu, Z., & Wang, G. (2021) *J. Mater. Res. Technol*. **10**, 175-187.

Chen, L., Kim, H. -S., Kim, S. -K. (2007) *ISIJ Int*. **47**, 1804-1812.

Choi, K., Seo, C. H., Lee, H., Kim, S. K., Kwak, J. H., Chin, K. G., Park, K. T. & Kim, N. J. (2010) *Scr. Mater*. **63**, 1028-1031.

Chateau, J. P., Dumay, A., Allain, S., Jacques, A. (2010) *Journal of Physics: Conference Series* **240**, 012023.

Chévenard, P. (1935) *Métaux.* **10**, 203.

Christian, J.W., Mahajan, S. (1995) *Prog. Mater. Sci.* **39**, 1–157.

Clayton, P., Devanathan, R., Jin, N., Steele, R. K. (1992) *International conference on rail quality and maintenance for modern railway operation*, Delft, Kluwer Academic Publishers.

Colette, G., Crussard, C., Kohn, A., Plateau, J., Pomey, G., Weiz, M. (1957) *Rev. Métall.* **54(6)**, 433–86.

Cordero, Z. C., Knight, B. E. & Schuh, C. A. (2016) *Int. Mater. Rev.* **61**, 495-512.

Cornette, D., Cugy, P., Hildenbrand, A., Bouzekri, M., Lovato, G. (2005) *Rev. Métall.* **12**, 905–918.

Dai, Q.-X., Wang An-Dong, C. X.-N., Luo, X.-M. (2002) *Chin. Phys*. **11(6)**, 596–600.

Dastur, Y., Leslie, W. (1981) *Metall. Mater. Trans. A* **12**, 749-759.

Das, S.R., Shyamal, S., Shee, S.K., Kömi, J.I., Sahu, P. (2021) *Mater. Charact*. **172**, 110833.
De Cooman, B. C., Chen, L., Kim, H. S., Estrin, Y., Kim, S. K. & Voswinckel, H. (2009). *State of the science of high manganese twip steels for automotive applications, Microstructures and texture in steels*, ch.10. Haldar A., Suwas, S. & Bhattacharjee, D. eds., Springer.
De Cooman, B. C., Estrin, Y. & Kim, S. K., (2018) *Acta Mater.* **142**, 283-362.
De Cooman, B.C., Chin, K.G. & Kim, J.Y. (2011) *New Trends and Developments in Automotive System Engineering*, Ed. M. Chiaberge, Publisher: InTech, Rijeka, Croatia.
De Cooman, B.C., Estrin, Y. & Kim, S.K. (2018) *Acta Mater*. **142**, 283-362.
Diehl, J. (1956) *Z. Metall*. **47**, 331.
Dieudonné, T., Marchetti, L., Wery, M., Miserque, F., Tabarant, M., Chêne, J., Allely, C., Cugy, P., Scott, C. P. (2014) Corros. Sci., **83**, 234–244.
Dini, G. & Ueji, R. (2012) *Steel Res. Int.* **83**, 374-378.
Dini, G., Najafizadeh, A., Ueji, R. & Monir-Vaghefi, S.M. (2010) *Mater. Des*. **31**, 3395-3402.
Doepken, H. C. (1952) *J. Met.* **4**, 166-170.
Dumay, A., Chatau, J.P., Allain, S., Migot, S. & Bouaziz, O. (2008). *Mater. Sci.Eng. A*. **483-484**, 184-187.
El-Danaf, E., Kalidindi, S. R. & Doherty, R. D. (1999). *Metall. Mater. Trans. A*. **30A,** 1223-1233.
Estrin, Y., Kubin, L. P. (1986) *Acta Metall*. **34(12)**, 2455-2464.
Estrin, Y. & Vinogradov, (2013) A. *Acta Mater*. **61**, 782-817.
Fan, D. W., Kim, H. S. & De Cooman, B. C. (2009) *Steel Res.Int.* **80,** 241-248.
Friedel, J.(1964) Dislocations, Pergamon, Oxford, , pp 264.
Frommeyer, G. & Brux, U. (2006) *Steel Res. Int*. **77**, 627-633.
Frommeyer, G., Brüx, U., & Neumann, P. (2003). *ISIJ Int.*, **43**, 438-446.
Frommeyer, G., Drewes, E. J. & Engl, B. (2000) *Rev. Metall. Cah. Inf. Tech*. **97**, 1245-1253.
Fu, X., Wu, X. & Yu, Q. (2018) *Mater. Today Nano*. **3**, 48-53.
Gleiter, H. (1989) *Prog. Mater. Sci.* **33,** 223-315.
Grassel, O., Frommeyer, G., Derder, C., Hofmann, H. (1997) *J. Phys. IV* **7**, 383-388.
Grassel, O., Kruger, L., Frommeyer, G. & Meyer, L. W. (2000) *Int. J. Plast.* **16,** 1391-1409.
Gutierrez-Urrutia, I. & Raabe, D. (2011). *Acta Mater*. **59**, 6449-6462.
Gutierrez-Urrutia, I. & Raabe, D. (2012) *Acta Mater.* **60**, 5791-5802.
Gutierrez-Urrutia, I. & Raabe, D. (2012a). Scr. *Mater*. **66**, 992-996.
Gutierrez-Urrutia, I. & Raabe, D. (2012b). *Mater. Sci. Forum*. **702-703**, 523-529.
Gutierrez-Urrutia, I. & Zaefferer, S., Raabe, D. (2010) *Mater. Sci. Eng*. A. **66**, 3552-3560.
Gwon, H. MS Thesis, Pohang University of Science and Technology, South Korea, 2017.
Gwon, H., Kim, J. K., Shin, S., Cho, L., De Cooman, B. C. (2017) *Mater. Sci. Eng. A* **696**, 416-428.
Hall, E. O. (1951) *Proc. Phys. Soc. Lond.* B. **64**, 747-753.
Hamada, A. S. & Karjalainen, L. P. (2006) *Can. Metall. Q*. **45,** 41-48.
Hamada, A. S., Karjalainen, L. P., Puustinen, J. (2009) *Mater. Sci. Eng. A* **517**, 68–77.
Hamada, A. S., Karjalainen, L. P. (2010) *Mater. Sci. Eng. A* **527**, 5715–5722.
Heinz, A., Neumann, P. (1990) *Acta Met. Mater*. **38**, 1933–1940.
Herrmann, J., Inden, G. & Sauthoff, G. (2003) *Acta Mater.* **51,** 2847-2857.

Hickel, T., Sandlöbes, S., Marceau, R. K. W., Dick, A., Bleskov, I., Neugebauer, J., Raabe, D., (2014) *Acta Mater*. **75**, 147–155.
Hirsch, P. B.(1975) The Physics of Metals, P. B. Hirsch (ed.), Cambridge University Press, Cambridge, , pp. 193.
Hughes, D.A. (1993). *Acta Metall. Mater*. **41**, 1421-1430.
Idrissi, H., Renard, K., Ryelandt, L., Schryvers, D. & Jacques P. J. (2010). *Acta Mater.* **58(7)**, 2464-2476.
Idrissi, H., Renard, K., Schryvers, D., Jacques, P.J. (2013) *Philos. Mag*. **93**, 4378-4391.
Jackson, P. J. (1983) *Mater. Sci. Eng*. **57**, 39-47.
Jang, J. H., Lee, C. H., Heo, Y. U. & Suh, D. W. (2012) *Acta Mater.* **60,** 208-217.
Jeong, J. S., Woo, W., Oh, K. H., Kwon, S. K., Koo, Y. M. (2012) *Acta Mater*. **60(5)**, 2290–2299.
Jin, J.E. & Lee, Y.K. (2009) *Mater. Sci. Eng.* A. **527**, 157-161.
Jin, J.-E. & Lee, Y.-K. (2012) *Acta Mater.* **60**, 1680-1688.
Jun, J. H. and Choi, C. S. (1998) *Mater. Sci. Eng. A* **257(2)**, 353-356.
Kang, J.-H., Duan, S., Kim, S.-J., Bleck, W. (2016) *Metall. Mater. Trans*. A. **47**, 1918-1921.
Kang, S., Jung, J. G., Kang, M., Woo, W. & Lee Y.K. (2016) *Mater. Sci. Eng*. A. **652**, 212-220.
Kannan, M. B., Raman, R. S., Khoddam, S. (2008) *Corros. Sci*. **50**, 2879–2884.
Katyk, S. A., Volodin, V. L., Zuev, L. B,, Rasshchupkin, V. P., Dadotchkin, N. V, Vulf, V. V. (1985) *Izvest. Vhz. Chermaya. Met*. **6**, 99–103.
Kim, J.K. & De Cooman, B. C. (2016). *Mater. Sci. Eng. A.* **676**, 216-231.
Kim, J., Lee, S. J., De Cooman, B. C. (2011) *Scr. Mater*. **65(4)**, 363–366.
Kim, J., and De Cooman, B. C. (2011) *Metall. Mater. Trans. A* **42(4)**, 932–936.
Kim, S.-D., Park, J. Y., Park, S.-J., Hoon Jang, J., Moon, J., Ha, H.-Y., Lee, C.-H., Kang, J.-Y., Shin, J.-H., Lee, T.-H. (2019) *Sci. Rep*. **9**, 1-13. 15171.
Karjalainen, L. P., Hamada, A., Misra, R. D. K., Porter, D. A. (2012) *Scr. Mater.* **66**, 1034–1039.
Kireeva, I.V., & Chumlyakov, Yu. I. (2009) *Phys. Met. Metallogr*. **108**, 298-309.
Kubin, L.P., & Kratochvíl, J. (2000) *Philos. Mag.* A. **80**, 201-218.
Kuhlmann-Wilsdorf, D. (2001) *Mater. Sci. Eng. A* **315**, 211-216.
Kuprekova, E. I., Chumlyakov, Yu. I. & Chernov, I. P. (2008). *Met. Sci. Heat. Treat*. **50**, 282-288.
Latanision, R. M., Ruff, A. W. (1971) *Metall. Trans.* **2(2)**, 505-509.
Lee, P. Y., Chiu, C. S., Gau,Y. J. &Wu, J. K. (1992) *High Temp. Mater. Proc*. **10**, 141-144.
Lee, S. -J., Kim, J., Kane, S. N., De Cooman, B. C. (2011) *Acta Mater*. **59**, 6809-6819.
Lee, S., De Cooman, B. C. (2015) *Steel Res. Int*. **86**, 1170-1178.
Lee, T., Koyama, M. Tsuzaki, K., Lee, Y.-H., Lee, C.S. (2012) *Mater. Lett*. **75**, 169-171.
Lee, Y.-K. & Choi, C. (2000) *Metall. Mater. Trans. A* **31**, 355-360.
Lee, Y.-K. (2012) *Scr. Mater*. **66**, 1002-1006.
Lehnhoff, G. R., Findley, K. O., De Cooman, B. C. (2014) *Scr. Mater*. **92**, 19–22.
Li, J. & Chou, Y. (1970) *Metall. Mater. Trans*. **1**, 1145.
Li, Y., Bushby, A. J., Dunstan, D. J. (2016) *Proc. R. Soc.* A. **472**, 20150890.
Liang, Z. Y., Li, Y. Z. & Huang, M. X. (2016) *Scr. Mater*. **112**, 28-31.
Luo, Z. C. & Huang, M. X. (2018) *Scr. Mater*. **142**, 28-31.
Mahajan, S. & Chin, G.Y. (1973) *Acta Mater*. **21**, 1353-1363.
Mahajan, S., Jin, S., Brasen, D. (1980) *Acta Metall*. **28**, 971–977.

McDermid, J.R., Bhadhon, K. M., McNally, E. A., Pallisco, D. M., Goodwin, F. E. (2016) In Proc. of the 108th Galvanizers Association Meeting, NW Resort, Farmingham, PA.
McHargue, C. J., McCoy, H. E. (1963) *Amer. Inst. Min. Eng*. **227**, 1170.
Miao, J., Pollock, T. M., Wayne Jones, J. (2012) *Acta. Mater*. **60**, 2840–2854.
Miao, J., Pollock, T. M., Wayne Jones, J. (2009) *Acta. Mater*. **57**, 5964–5974.
Mineur, M., Villechaise, P., Mendez, J. (2000) *Mater. Sci. Eng. A* **286**, 257–268.
Miodownik, A.P. (1998). Z. *Metallkunde***. 89**, 840-847.
Mohammed, A. A. S., El-Danaf, E. A. & Radwan, A. A. (2007). *Mater. Sci. Eng. A.* **457**, 373-379.
Morris, D. G., Munoz-Morris, M. A. & Requejo, L. M. (2006) *Acta Mater.* **54,** 2335-2341.
Nabarro, F. R. N. (1967) Theory of Crystal Dislocations, Oxford University Press, Oxford, , pp. 260.
Nabarro, F. R. N., Basinski, Z. S. & Holt, D. B. (1964) *Adv. in Phys*. **13**, 193-323.
Naik, S. N. & Walley, S. M. (2019) *J. Mater. Sci*. **55**, 2661-2681.
Niendorf, T., Lotze, C., Canadinc, D., Frehnc, A., Maier, H. J. (2009) *Mater. Sci. Eng. A* **499**, 518–524.
Niendorf, T., Rubitschek, F., Maier, H. J, Niendorf, J., Richard, H. A, Frehn, A. (2010) *Mater. Sci. Eng. A* **527**, 2412–2417.
Niewczas, M., Saada, G. (2002) *Philos. Mag. A* **82**, 167–191.
Oh, B. W., Cho, S. J., Kim, Y. G., Kim, Y. P., Kim, W. S. and Hong, S. H. (1995) *Mater. Sci. Eng. A* **197**, 147–156.
Olson, G. B. & Cohen, M. (1976a) *Metall. Trans.* A. **7,** 1897-1904.
Ookawa, A. (1957) *J. Phys. Soc.* Japan **12**, 825.
Otte, H. M. (1957) *Acta Metall*. **5(11)**, 614-627.
Park, K. T. (2013) *Scr. Mater*. **68**, 375-379.
Park, K. T., Jin, K. G., Han, S. H., Hwang, S. W., Choi, K. & Lee, C. S. (2010) *Mater. Sci. Eng*. A. **527**, 3651-3661.
Peng, X., Zhu, D. Y., Hu, Z. M. (2014) J. Iron Steel Res. Int. 21(1), 116-120.
Petch, N. J. (1953). *J. Iron. Steel. Inst.* **174**, 25-28.
Pierce, D. T., Bentley, J., Jiménez, J. A. & J. E. Wittig. (2012). *Scr. Mater.* **66**, 753-756.
Pierce, D. T., Jimenez, J. A., Bantley, J., Raabe, D. & Witting, J.E. (2015). *Acta Mater*. **100**, 178-190.
Pierce, D.T., Jimenez, J. A., Berntley, J., Raabe, D., Oskay C. & Witing, J.E. (2014). *Acta Mater.* **68**, 238-253.
Qin, X.M., Chen, L.Q., Di, H.S. & Deng, W. (2011). *Acta Metall. Sin*. **47**,1117.
Raghavan, K. S., Sastri, A. S., Marcinkowski, M. J. (1969) *Trans. Met. Soc. AIME* **245**, 1569-1575.
Remy L. (1977) Acta metall. 25(2), 173-179.
Remy, L. & Pineau, A. (1977) *Mater. Sci. Eng*. **28**, 99-107.
Rittel, D., Roman, I. (1989) *Int. J. Fatigue* **11(3)**, 177–182.
Roberts, W. N. (1964) *Trans. AIME* **230**, 372–377.
Rolltt, A.D. & Kocks, U. F. (1993) *Solid State Phenom.* **35-36**, 1-18.
Sato, Y. S., Kwon, E.P., Imafuku, M., Wagatsuma K., Suzuki, S. (2011). *Mater.Character.* **62**, 781-888.
Saxena, V. K., Krishna, M. S. G., Chhaunker, P. S. & Radhakrishnan, V. M. (1994) *Int. J. Press. Vessels Pip.* **60,** 151-157.
Schmidt, W. (1930) *Arch. Eisenhuttenwes.* **3**, 293.

Schumann, V.H. (1972). *NeueHütte*. **17**, 605-609.
Scott, C., Guelton, N., Allain, S. & Faral, M. (2005). *Mater. Sci. Technol. Conf.*, **2**, 127-138.
Scott, C., Remy, B., Collet, J.-L., Cael, A., Bao, F. Danoix, C., Malard, B. Curfs, C. (2011) *Int. J. Mater. Res.* **102**, 538-549.
Seo, W., Jeong, D., Sung, H., Kim, S. (2017) *Mater. Charact*. **124**, 65–72.
Sevillano, J.G. & de Las Cuevas, F. (2012) *Scr. Mater.* **66,** 978-981.
Sevillano, J.G. (2009) *Scr. Mater*. **60**, 336-339.
Shao, C. W., Zhang, P., Wang, X. G., Wang, Q., Zhang, Z. F. (2019) *Mater. Res. Lett.* **7(1),** 26-32.
Shen, Y., Jia, N., Misra, R., Zuo, L. (2016) *Acta Mater*. **103**, 229-242.
Shih, S. T., Tai, C. Y. & Perng, T. P. (1993) *Corrosion* **49,** 130-134.
Takaki, S., Nakatsu, H. & Tokunaga, Y. (1993) *Mater. Trans. JIM.* **34**, 489-495.
Tang, Z., Huang, J., Ding, H., Cai, Z., Zhang, D., Misra, D. (2018) *Metals*. **8(7)**, 476.
Tian, X., Li, H. and Zhang Y. (2008) *J. Mater. Sci.* **43(18)**, 6214–6222.
Tian, X., Zhang, Y. (2009) *Mater. Sci. Eng. A* **516(1–2)**, 73–77.
Timokhina, I., Medvedev, A., Lapovok, R., (2014) *Mater. Sci. Eng*. A. **593**, 163-169.
Timokhina, I. B., Hodgson, P. D., Pereloma, E. V. (2004) *Metall. Mater. Trans. A* **35(8)**, 2331-2341.
Tirry, W., Schryvers, D. (2005) *Acta Mater.* **53**, 1041–1049.
Troiano, A. R. & McGuire, F. T. (1943) *Trans. ASM* **31**, 340-346.
Ueji, R., Tsuchida, N., Fujii, H., Kondo, D., Kunishige, K. (2007) *J. Jpn. I. Met*. **71**, 815-821.
Ueji, R., Tsuchida, N., Terada, D., Tsuji, N., Tanaka, Y., Takemura, A. & Kunishige, K. (2008) *Scr. Mater*. **59**, 963-966.
Valiev, R.Z., Estrin, Y., Horita, Z., Langdon, T.G., Zechetbauer, M.J., Zhu, Y.T. (2006) JOM **58,** 33-39.
Venables, J. A. (1961) *Philos. Mag*. **6**, 379–396.
Venables, J. A. (1964) *J. Phys. Chem. Solids*. **25**, 685–692.
Venables, J.A. (1974) *Philos. Mag.* **30**, 1165–1169.
Vitek, V. (1968) *Philos. Mag.* **18**, 773-786.
Vitek, V. (1970) *Scr. Metall.* **4**, 725-732.
Volosevich, P., Gridnev, V. & Petrov, Y. (1976) *Phys. Met. Metallogr*. **42**, 126-130.
Wang, L., Guan, P., Teng, J., Liu, P., Chen, D., Xie, W., Kong, D., Zhang, S., Zhu, T., Zhang, Z., Ma, E., Chen, M., Han, X. (2017) *Nat. Commun*. **8**, 1–7.
Wang, X. D., Huang, B. X., & Rong, Y. H. (2006). *Mater. Sci. Eng*. A, **438-440**, 300-305.
Wang, X., Liang, Z. Y., Liu, R. D., Huang, M. X. (2015) *Mater. Sci. Eng. A* **647**, 249–255.
Wilsdorf, D. K. (1989). *Mater. Sci. Eng. A*, **113**, 1-41.
Wu, Y.- X., Tang, D., Jiang, H. -T., Mi, Z. -L.; Xue, Y., Wu, H. -P. (2014) *J. Iron Steel Res. Int*. **21**, 352–358.
Yakubtsov, I. A., Airapour, A. & Perovic, D. D. (1999). *Acta Mater*. **47**, 1271-1279.
Yamakov, V., Wolf, D., Salazar, M., Phillpot, S. R., Gleiter, H. (2001) *Acta Mater.* **49**, 2713–2722.
Yen, H. W., Huang, M., Scott, C. P., Yang, J. R., (2012) *Scr. Mater*. **66(12)**, 1018-1023.
Yoo, J. D. & Park, K. T. (2008) *Mater. Sci. Eng*. A. **496**, 417-424.
Yoo, J. D., Hwang, S. W. & Park, K. T. (2009). *Mater.Sci. Eng. A*, **508**, 234-240.
Zambrano, O. A. (2016) *J. Eng. Mater Technol.* **138(4)**, 041010.

Zhi, H., Zhang, C., Antonov, S., Yu, H., Guo, T., Su, Y. (2020) *Acta Mater*. **195**, 371-382.
Zhu, Y. T., Liao, X. Z., Wu, X. L. (2012) *Prog. Mater. Sci.* **57**, 1–62.
Zhu, X. M. & Zhang, Y. S. (1998) *Corrosion*, **54**, 3-12.

Chapter 2

Methodologies associated to microstructure characterization

2.1 Interpretation of extended defects in crystals and the underlying principles

It is well known that several types of instrumentals set up as well as different techniques are used to interpret the deformation microstructures, but each of them have its own merits and demerits as well. Different types of lattice imperfections were studied using different techniques, and Bryne (1965) had reviewed it in great detail. In the present dissertation, three different methodologies, namely, X-ray diffraction (XRD), transmission electron microscopy (TEM) and electron backscatter diffraction (EBSD) are used to interpret the deformation microstructure of two different steels with chemical compositions: Fe-16Mn-1.5Al-0.3C (wt.%) and Fe-0.17C-2.2Si-10.8Mn-18.0Cr-4.7Ni- 0.9V-0.25N (wt.%) under different experimental conditions, whose underlying principles are briefly described in following sections.

2.2 X-ray diffraction

In general, X-ray diffraction (XRD) is used to identify the crystalline phases present in a material. However, other microstructural information related to the different types of imperfections that may produce during crystal growth or plastic deformations can be extracted from a detailed analysis of XRD patterns. Basically, X-ray diffraction is a scattering phenomenon, when X-rays beam interact with the atoms of a material then scattering occurs in all directions. It is experimentally observed that the scattered X-ray beams follow two completely distinct patterns for crystalline and non-crystalline materials. In 1913, Lawrence Bragg and his father, William Henry Bragg, first derived a theory to explain the patterns of X-rays scattered from crystalline materials. In this model, they consider each plane of atoms as a source of scattered radiation and proposed that the diffraction effect will be observed only when the distance between the sources is comparable to the wavelength of the X-rays radiation. The interaction of X-rays with atoms gives rise to scattering in all directions, however, the scattered X-ray beams will be completely in phase along some of those directions and therefore, the scattered beams strengthen each other to form diffracted beams by following the Bragg's law, which can be expressed as:

$$2d_{hkl}\, sin\, \theta = n\lambda \qquad (2.1)$$

where, λ is the wavelength of X-rays incident on the set of parallel crystalline planes (hkl). The distance between identical planes of a crystal is indicated by d_{hkl}, whereas n is the order of reflection, and the angle θ where maximum intensity occurs is called Bragg angle. The schematic representation in Fig. 2.1 clearly indicates the different parameters related to the mathematical form of the Bragg's law presented in Eq. 2.1. In case of an ideal crystal each crystallographic phase consists of a set different inter-planar spacing d_{hkl} for each individual (hkl) crystallographic planes, and which produces a specific diffraction pattern at corresponding Bragg angles. However, in reality there are always some impurities present in crystals, and also the incident X-ray beam is not always perfectly parallel and monochromatic. Therefore, the experimental X-ray peaks are always found to be broad peaks instead of sharp lines, and interestingly, one can extract information related to the defects from the amount of X-ray peak broadening, which is discussed subsequently.

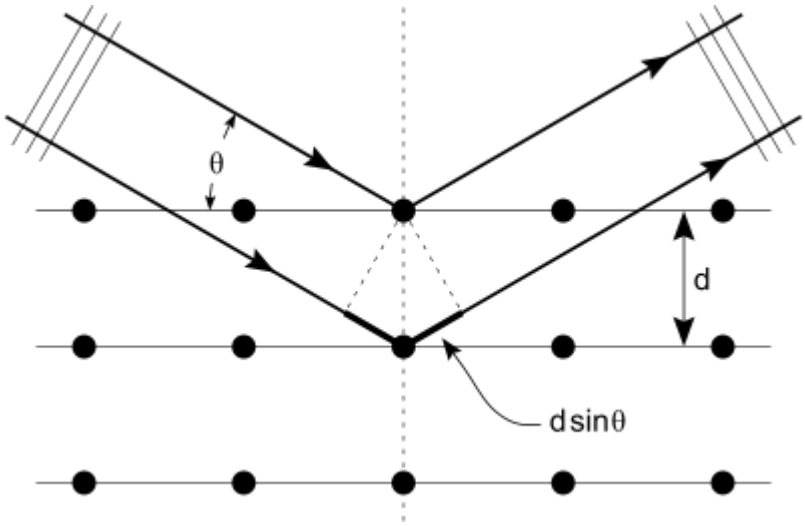

Fig. 2.1: Schematic representation of the Bragg's law.

One of the most important applications of X-ray line profile analysis (XLPA) of a powder diffraction pattern is immensely successful to study the nature of crystal imperfections, whereas it produces somewhat scatter outcomes for a highly deformed bulk specimen. It is well known that any types of plastic deformation introduce broadening to the XRD profiles, and the amount of broadening increases along with the amount of deformation of the specimen. The broadening in X-ray diffraction profiles occurs mainly due to small crystallite size, micro-strain inside the crystallites and

different types of defects, line defects and planar defects, present with in the crystal. However, it is important to be mentioned here that other than crystallite size-strain and defects, some instrumental parameters such as: slit widths, sample size, penetration in the sample, imperfect focusing, unresolved α_1 and α_2 peaks etc. are also responsible for some extraneous broadening of the line profile. The signature of these extraneous sources is always be present in the diffraction profiles, as it is mainly depends on the experimental set up of the diffractometer, and therefore these types broadening are generally termed as "instrumental broadening". Scherrer (Scherrer, 1918) first proposed the idea of determination of crystallite size from X-ray line profile and reported that the line breadth is inversely proportional to the size of the crystallites. According to the Scherrer, the line breadth (β) can be expressed interms of the wavelength of the X-ray (λ), Bragg angle (θ) and apparent crystallite size (D) as:

$$\beta = \frac{K_S \lambda}{D \cos\theta} \qquad (2.2)$$

where, K_s is known as Scherrer constant ($1.0 > K_s > 0.89$), which strongly depends on the shape of the crystallite.

It is clearly observed from Eq. (2.2) that the crystallite size is strongly crystallographic direction dependent i.e., the length of the crystallite size is different along different crystal orientation, whereas the size broadening is independent of the order of reflection. A careful observation of the Scherrer formula presented in Eq. (2.2) indicates that the instrumental broadening, which is always be present along with the diffraction profile, is totally neglected. Therefore, to get precise information about the microstructural parameters one has to extract the amount of instrumental broadening from the diffraction profile, and thus the Scherrer formula given in the Eq. (2.2) is not appropriate to study the diffraction profile of the materials containing strain broadening. However, the Scherrer formula give considerably well outcomes for undeform specimens where the crystallite size is less than hundred angstroms and therefore, the amount of line broadening is insignificant in that circumstances due to such small crystallite size.

Many physicists have observed that the diffraction line broadening arising from micro-strain, ε_L , strongly correlated with the Bragg angle and the order of the reflection. They also suggest that in terms of the breadth of the corresponding

diffraction line and Bragg angle, the amount of strain-broadening of a diffraction line can be expressed as:

$$\beta = 4\varepsilon_L \ tan\,\theta \qquad (2.3)$$

It is clearly seen from Eq. (2.3) that one can easily calculate the contribution of strain broadening in terms of micro-strain parameter, ε_L . However, in case of a polycrystalline specimen, it is observed that there exists a noticeable variation in crystallite size with grains containing different types of line and planar defects, and therefore, a precise interpretation of the peak broadening is difficult due to these distortions. In general, the Scherrer equation produces large values of coherently diffracting domains, although Scherrer equation established the first relation between microstructural properties of a specimens and their corresponding Bragg reflection profile. Therefore, the use of some more advanced techniques is briefly presented in the following sections.

2.2.1 The integral breadth method and the Williamson-Hall analysis

The integral breadth method is one of the oldest methods to determine the crystallite size and micro-strain related parameters. In 1918, Scherrer first described the breadth of a diffraction line as its angular width in radians at a point where the intensity has fallen by half of its maximum value. Later, von Laue defined the breadth of a diffraction line as the ratio of the integrated intensity of the line profile above the background to the diffraction peak height (I_p), and according to him the diffraction line breadth (β) can be expressed as:

$$\beta = \frac{1}{I_p}\int I(2\theta)\, d_{hkl}(2\theta) \qquad (2.4)$$

In integral breadth method the separation of size and strain broadening component of integral breadth is difficult as it strongly depends on the shape of the broadening profile due to each component, i.e., size and strain component. Generally, it is considered that the broadening is occurred only due to lattice strain if the crystallite size is greater than 10^{-4} cm i.e., $D \geq 10^{-4}$cm. However, the broadening composed of both the crystallite size and lattice distortion can exist in a diffraction profile, and then the separation of crystallite size and micro-strain component can be done only if the

shapes of their individual broadening profiles are completely known. In those circumstances, the total integral breadth of a Bragg peak is equal to the sum of the size and strain-broadening component, and can be expressed as:

$$\beta = \beta_s + \beta_D \tag{2.5}$$

where, β_s and β_D represent the size-broadening and strain-broadening integral breadth component, respectively. In 1953, Williamson and Hall further use the concepts of distinct dependences of the both broadening components to segregate the effects of size and strain broadening in their analysis, and expressed the integral breadth as:

$$\beta_{2\theta} = \frac{K_s \lambda}{\langle D \rangle_V \cos\theta} + 2K_D \varepsilon_L \tan\theta \tag{2.6}$$

where, K_s is the constant used by Scherrer, and $\beta_{2\theta}$ is the integral breadth. The previously mentioned integral breadth β can now be modeled numerically as a function of scattering angle 2θ and the course of $\beta(2\theta)$ can be fitted with the model function in Eq. (2.6) and thereby from the fitting parameters, the average volume-weighted crystallite size, $\langle D \rangle_V$ and micro-strain, ε_L, are obtained. The Eq. (2.6) can be written in more scientific and convenient way by multiplying $\frac{\cos\theta}{\lambda}$ in the both sides of Eq. (2.6), and which yields:

$$\beta_{2\theta} \frac{\cos\theta}{\lambda} = \frac{K_s}{\langle D \rangle_V} + 2K_D \varepsilon_L \frac{2\sin\theta}{\lambda} \tag{2.7}$$

Interestingly, the Eq. (2.7) clearly indicates that the variation of $\frac{\beta \cos\theta}{\lambda}$ with $\frac{2\sin\theta}{\lambda}$ give a straight line, and the value of the average volume-weighted crystallite size, $\langle D \rangle_V$ as well as the micro-strain parameter, ε_L, can be easily obtained from the intercept and the of the slope of the straight line, respectively. The plot of $\frac{\beta \cos\theta}{\lambda}$ vs $\frac{2\sin\theta}{\lambda}$ graph is commonly known as conventional Williamson-Hall (W-H) plot. Although the determination of crystallite size and micro-strain parameters are quite straightforward using the W-H plot according to Eq. (2.7), but a special caution should be taken while various anisotropies are present in the diffraction profiles. In presence of highly anisotropic component, which may be associated with the microstructure of the specimens, the W-H plot shows a significant scatter of the data points around an ideal straight line, and therefore one have to take into account the effect of the anisotropy

component to extract precise microstructural information, which is discussed subsequently.

2.2.2 The Fourier method in X-ray line profile analysis

In case of the diffraction profile of any imperfect crystals, i.e., crystals composed of different types of line as well as planar defect, the Warren-Averbach (WA) technique of peak-shape analysis using Fourier method is a very common and prevailing method to analyse the peak broadening due to both, size and strain broadening component. In case of X-ray diffraction line profile analysis, the Fourier methods of expressing any distribution function as a sum of sine and cosine terms play an important role. According to Warren, the intensity distribution of an X-ray diffraction peak may be expressed in terms of Fourier series, and can be written as (Warren, 1969):

$$P_i(\Delta K) = N \sum_{L=-\alpha}^{+\alpha} A(LK_i)\cos(2\pi L\Delta K) + B(LK_i)\sin(2\pi L\Delta K) \qquad (2.8)$$

where, N is (approximately) a constant, and L represents the perpendicular distance to the diffracting planes. The Fourier cosine and sine coefficients are represented by the constants A and B, respectively. In practice, L is considered as a specific discrete value $n\Delta L$, where n is an integer and ΔL is inversely proportional to the length of the measurement range in the reciprocal space. The diffraction line profile according to Eq. (2.8) is defined with respect to a distance K_i to the origin in reciprocal space, related to the diffraction angle $2\theta_i$, and the value of K_i is defined as: $K_i = 2sin\theta_i/\lambda$, where λ is the wavelength of the incident X-ray radiation. The deviation from K_i is denoted by ΔK, and therefore, it can be expressed as: $\Delta K = 2(sin\theta - sin\theta_i)/\lambda$. Usually, the value of $2\theta_i$ is so chosen that it coincides with the centroid of the diffraction peak. Another important information should be mentioned here that any pair of diffraction line profile, P_1 and P_2; satisfying the condition $K_2 = 2K_1$ is known as a first and second order reflection. Since, the imaginary parts of the Fourier series i.e., the sine coefficients are not physically interpreted (Mittemeijer & Delhez, 1978; Ungar *et al*., 1989), and therefore only the real parts i.e., the cosine coefficients of the Fourier series, $A(L, K_i)$ are considered for further analysis.

2.2.3 The conventional Warren-Averbach analysis

It is well established that the intensity distribution of X-ray diffracted from a imperfect crystalline specimen consist of a mixture of both, structurally and instrumentally broadened diffraction line profile. Since, the intensity of a diffraction profile can be expressed in terms of Fourier series, as discussed in § 2.2.2, and therefore the Fourier coefficients of the measured diffraction profile are also be a combination of both, the structural and instrumental line profiles. The contribution of instrumental profile can be evaluated by measuring the diffraction profile of a 'standard' specimen, which is free from any types of lattice defects, and which can be treated as the instrumental profile for the particular instrumental set-up. Now, the actual contribution of the structural components from the diffraction profile measured using this instrumental set-up can be easily evaluated by subtracting the previously measured instrumental component profile. According to Stokes, the Fourier coefficients of the structurally broadened line profile can obtain (Stokes, 1948) by convoluting the Fourier coefficients of the line profiles of imperfect specimen and the 'standard' specimen. Another way of removing the instrumental profile from the measured diffraction profile can be done by treating two broadened line profiles analogously if no standard specimen is available, and in that case one can define the diffraction profile with a smaller broadening as instrumental profile. By doing this, the resultant Fourier coefficients will reflect only the differences due to the lattice imperfections (crystallite size and micro-strain) present in the specimen, and the instrumental profile of both the profile will cancel each other.

For a structurally broadened diffraction line profile the real part of the Fourier series, i.e. the cosine coefficients can be written as the products of two coefficients, named as: size component $A^s(L)$ and strain component $A^d(L, K_i)$ (superscript s for size and d for distortion). Interestingly, both of these coefficients are independent of diffraction-order, i.e., a particular set of diffracting planes have similar types of size and strain components. Now, the challenge is to evaluate the value of these two components for a diffraction profile, and to do that one can consider that the specimen is composed of columns parallel to the diffraction vector instated of atoms. In this circumstance, the column length and the column length (size) distribution can be represented by D and $\rho(D)$, respectively. Now, the average column length (size) i.e., $\langle D \rangle$, and the Fourier size component, i.e., $A^s(L)$ can be easily determined from the

column length (size) distribution function $\rho(D)$. Similarly, one can easily determine the strain component, $A^d(L, K_i)$, from the strain distribution function $\rho(\varepsilon_L)$. An important aspect should be mentioned that here ε_L represents the average of the true (local) strain ε_0 over a length L. According to Warren, both the distribution i.e. column length and strain distribution functions normalized to unit area can be expressed as (Warren, 1959):

$$A(L, K_i) = A^s(L)\, A^d(L, K_i), \tag{2.9}$$

$$A^s(L) = \frac{1}{\langle D \rangle} \int_{|L|}^{\infty} (D - |L|)\, \rho(D) dD \tag{2.10}$$

$$A^d(L, K_i) = \int_{\propto}^{\infty} \rho(\varepsilon_L)\, \cos(2\pi L K_i \varepsilon_L) d\varepsilon_L \tag{2.11}$$

In this method of separating the size and strain component, it is recommended that at least two orders of reflections have to be measured separately to know the most accurate statistics of $A^s(L)$ and $A^d(L, K_i)$ distribution function. Another careful measure must be kept in mind that the assumptions imposed on $\rho(D)$ and $\rho(\varepsilon_L)$ to evaluate $A^s(L)$ and/or $A^d(L, K_i)$ must be consistent with the experimental conditions and the materials properties. However, the later can be accomplished in various ways that are resulting in different separation methods. In practice, one must choose the separation method that suits best for the specimens they are studying.

A careful observation indicates that the size component $A^s(L)$ is independent of diffraction vector; whereas, the strain component $A^d(L, K_i)$ is a function of K_i, i.e. it strongly depends on the diffraction vector. The strain component can also be made independent of the diffraction vector for a smaller range of K_i by using the concept of Taylor-series expansion. According to Warren & Averbach, the strain component $A^d(L, K_i)$ can be expanded in Taylor-series for small L and K_i, and it can be expressed as (Warren & Averbach, 1950; van Berkum *et al*., 1994):

$$ln\, [A^d(L, K_i)] \cong -2\pi^2 L^2 K_i^2 \langle \varepsilon_L^2 \rangle \cong (K_i/K_1)^2 ln\, [A^d(L, K_1)] \tag{2.12}$$

where, $\langle \varepsilon_L^2 \rangle$ is represent the mean squared strain. Interestingly, the Eq. (2.12) give the exact value of $A^d(L, K_i)$ for all values of L and K_i if only if all the strain distribution functions i.e. $\rho(\varepsilon_L)$ are purely Gaussian distribution in nature (Warren & Averbach,

1950). As the strain distribution function $\rho(\varepsilon_L)$ deviates more from being Gaussian, the range of L will be smaller for which the Eq. (2.12) remains valid.

Now, combining the order independency nature of $A^s(L)$ and Eq. (2.12) the Eq. (2.9) can be expressed in a more significance way, and Warren & Averbach wrote it in a more compact form, which is also known as W-A equation (Warren & Averbach, 1952):

$$ln\,[A(L,K_i)] = ln\,[A^s(L] - 2\pi^2 L^2 K_i^2 \langle \varepsilon_L^2 \rangle \qquad (2.13)$$

However, tor the sake of comparison with the other separation method, the following form of the basic equation for the W-A analysis is mostly favoured:

$$ln\,[A(L,K_i)] \;=\; ln\,[A^s(L] - (K_i/K_1)^2\; ln\,[A^d(L,K_i] \qquad (2.14)$$

The Eq. (2.14) clearly indicates that the parameter, $ln\,[A(L,K_i)]$ changes linearly with $(K_i/K_1)^2$. Therefore, the size and strain component of the Fourier coefficients can easily be determined from the Y- intercept and the slope of $ln\,[A(L,K_i)]$ vs $(K_i/K_1)^2$ plot, respectively. After evaluating the strain component, the mean squared strain $\langle \varepsilon_L^2 \rangle$ can be directly determined from $A(L,K_i)$ using Eq. (2.12) only if the application of the W-A analysis is acceptable for the diffraction profile.

2.2.4 The modified Williamson-Hall and Warren-Averbach analysis

The scatter data points in the conventional Williamson-Hall plot are mainly caused due to the presence of strain anisotropy in the diffraction profile of the specimen, and Ungar and his coworkers first take the effect of strain anisotropy into account in their X-ray diffraction profile analysis procedure. They considered the strain anisotropy factors in terms of elastic constants by introducing dislocation contrast factors ($\bar{C}_{hkl}$) for different representative Bragg reflections (hkl), and which shows a significant reduction in the scatter data points while plotted according to the Williamson-Hall relation using Eq. (2.7). This modification of introducing the dislocation contrast factors ($\bar{C}_{hkl}$) in Williamson-Hall and W-A procedure is commonly referred to as the modified Williamson-Hall and W-A analyses.

The average contrast factors ($\bar{C}_{hkl}$) for different Bragg reflections (hkl) were further used in the modified W-H plot (Ungar et al., 1998a; Sahu et al., 2012) and in the modified W-A procedure (Ungar et al., 1998; Sahu et al., 2012) to determine the dislocation densities (ρ), the effective outer cut-off radius (R_e) of dislocations and the dimensionless quantity, $M = R_e\sqrt{\rho}$. The parameter R_e indicates the range over which the dislocation could be assumed as randomly distributed, while M represents the dipole character of the dislocations, whose value smaller or larger than unity indicate a stronger or weaker dipole character, respectively (Wilkens, 1970; Ungar et al., 1998a). The full-width half-maxima (FWHM) i.e. the width of a diffraction peak at the half of it's maximum intensity value of the Bragg reflections were obtained after fitted using a pseudo-Voigt (pV) function according to Enzo et al. (1988). It is important to be mentioned that a pseudo-Voigt function is basically a convolution of Gaussian and Lorentzian distribution function that suits best for any diffraction profile fitting. Now, the measured FWHM could be substituted into the W-H equation, which can be written as (Williamson & Hall, 1953):

$$\Delta K = \frac{0.9}{D} + \Delta K^{D} \qquad (2.15)$$

where, $K = \frac{2\sin\theta}{\lambda}$ is the magnitude of the diffraction vector, $\Delta K = \frac{2\cos\theta}{\lambda}\Delta\theta$ is the FWHM, θ and λ represent the Bragg angle and wavelength of the X-rays used, respectively. The average crystallite size is represented by D, whereas the strain contribution to X-ray peak broadening is represented by ΔK^{D}. Furthermore, by invoking the concept of dislocation contrast factors, Ungar et al. (1998a) suggested that the conventional W-H equation, i.e. Eq. (2.15) could be modified in terms of the scaling factor $K^2\bar{C}_{hkl}$, and can be expressed as:

$$\Delta K = \frac{0.9}{D} + \left(\frac{\pi M^2 b^2}{2}\right)^{1/2} \rho^{1/2} K\bar{C}_{hkl}{}^{1/2} + O(K^2\bar{C}_{hkl}) \qquad (2.16)$$

The parameters, ρ and b represent the dislocation density and the magnitude of the Burgers vector, respectively, and O represents the higher order terms in the $K^2\bar{C}_{hkl}$ series. For very small value of $K^2\bar{C}_{hkl}$, we can neglect the higher order terms of the quadratic Eq. (2.16) and after squaring Eq. (2.16), the following equation can be obtained:

$$[(\Delta K^2) - \alpha]/K^2 \; = \; \beta \, \bar{C}_{hkl} \qquad (2.17)$$

where, $\alpha = \left(\frac{0.9}{D}\right)^2$ and $\beta = \frac{\pi M^2 b^2 \rho}{2}$. In case of cubic crystals, it is well established that the average dislocation contrast factors, $\bar{C}_{hkl}$, corresponding to the Bragg reflections (hkl) can be expressed as (Ungar et al., 1999):

$$\bar{C}_{hkl} = \bar{C}_{h00}(1 - qH^2) \qquad (2.18)$$

where, $\bar{C}_{h00}$ is the average contrast factor for (h00) type of Bragg reflections, and it can be directly estimated by using the elastic constants of the crystal. The parameter, q, is often known as dislocation character parameter, which is a function of both elastic anisotropy (A_i) and the ratio of the elastic constant (c_{12}/c_{44}) of the crystal. Interestingly, the value of this parameter determines whether most of the dislocations are screw or edge types. Furthermore, the parameter H^2 can be defined as:

$$H^2 = \frac{(h^2k^2+k^2l^2+l^2h^2)}{(h^2+k^2+l^2)^2} \qquad (2.19)$$

Using Eq. (2.18) in Eq. (2.17), the modified W-H formula i.e. the Eq. (2.16) further reduces to:

$$[(\Delta K^2) - \alpha]/K^2 = \beta \bar{C}_{h00}(1 - qH^2) \qquad (2.20)$$

The Eq. (2.20) clearly indicates that the value of the parameter q can be easily determined from the linear relation of $[(\Delta K^2) - \alpha]/K^2$ vs. H^2 plot, and the X-intercept of the plot directly give the value of reciprocal of q. For austenite Ungar *et al*. (1999) reported that the values of q for pure edge and screw dislocations are 1.71 and 2.46, respectively. They also showed that depending on the numerical values of the parameter q, the nature of dislocations changes from purely edge to a mixed type as q parameter increases from 1 to 2, and finally it becomes purely screw type as q parameter goes above 2. Another important use of this parameter is the estimation of the fractions of edge and screw dislocations present in microstructure. The faction of dislocations with a specific character type can be estimated according to following relation (Garabagh *et al*., 2008):

$$f_{\gamma(edge)} = \frac{(2.46-q_\gamma)}{(2.46-1.71)} \qquad (2.21)$$

$$f_{\gamma(screw)} = 1 - f_{\gamma(edge)} \quad (2.22)$$

In the Eq. (2.21 & 2.22), the fraction of edge and screw type components of the total dislocations present within the austenite microstructure are indicated by the terms, $f_{\gamma(edge)}$ and $f_{\gamma(screw)}$, respectively.

In a similar fashion, the concept of average contrast factor can be use to evaluate the Fourier coefficients in W-A analysis. After adopting the concept of dislocation contrast factor concept in to the conventional W-A equation, Ungar and his co workers showed that the real part of the Fourier coefficients, $A(L)$, can be expressed in a modified form of the conventional W-A equation, and that can be written as (Ungar et al., 1998a):

$$ln\, A(L) \cong ln\, A^s\,(L) - \rho \frac{\pi b^2}{2} L^2\, ln\left(\frac{R_e}{L}\right)(K^2 \bar{C}_{hkl}) + O(K^4 \bar{C}^2{}_{hkl}) \quad (2.23)$$

where, L is known as Fourier variable, and $A^s(L)$ indicates the size component of Fourier coefficients of a diffraction peak profile. Neglecting the higher order terms of $K^2\bar{C}_{hkl}$ in Eq. (2.23), which is indicated by the term $O(K^4\bar{C}^2{}_{hkl})$, the parameter in the left hand side i.e. $\ln A(L)$ becomes only a function of $K^2\bar{C}_{hkl}$. Therefore, the real part of the Fourier coefficients estimated from the pV fitting of individual Bragg reflection may be plotted for various L values, and whose slope (Y) from the linear regions can be approximated as $\rho \frac{\pi b^2}{2} L^2 \ln\left(\frac{R_e}{L}\right)$. Now, the rearrangement of parameters leads to express the slope in Eq. (2.23) in a simple and effective shape as:

$$\frac{Y(L)}{L^2} = \rho \frac{\pi b^2}{2} \ln(R_e) - \rho \frac{\pi b^2}{2} \ln(L) \quad (2.24)$$

It is clearly observed that the shape of the Eq. (2.24) is identical to $y = mx + c$, and thus yielding a linear relationship between $\frac{Y(L)}{L^2}$ and $\ln(L)$. Now, the parameters i.e. the dislocation density, ρ, and the effective outer cut-off radius of dislocations, R_e, can be directly determined from the slope and the Y-intercept of $\frac{Y(L)}{L^2}$ vs $\ln(L)$ plot according to the Eq. (2.24), respectively. The estimated dislocation density and outer cut-off radius of dislocations are further used to study other microstructural parameters such as: stacking fault energy (SFE), planar fault probabilities, dipole character of dislocations etc.

2.2.5 Estimation of planar fault parameters

As discussed in § (2.2.4), the X-ray diffraction profile can be use to interpret the effects of planar defects i.e. stacking faults (SFs) and twin, present in the microstructure of a deformed specimen. Barrett (1952) first suggest that the SFs can be generated in a close-packed fcc metals as a result of cold work, and he also identify certain changes among the XRD patterns of the specimens with and without SFs. It is important to be mentioned here that there are two different types of planar faults; one created during crystal growth and another planar faults may be created during plastic deformation. In his study of planar faults of a fcc metals, Paterson (1952) showed that the presence of growth faults produce asymmetry broadening, whereas, deformation faults produce symmetric broadening. The difference equation method was formerly used by Wilson (1942) and then by Paterson (1952) to interpret the SFs issue, and which leads to the expression for the probability of m^{th} neighbour layer is the same or different from the original layer. Later, Gevers (1954a) gives the difference equation by combining the effect of both, the growth and deformation faults. According to Warren, the probabilities of occurrences of both type faults are sufficiently small for an fcc structure, and therefore he gives a simplified form of Gevers (1954b) technique by considering that the fault probabilities are very small. It is well acceptable that the shift in peak positions, peak asymmetry and peak broadening effects mainly contribute to the two types of fault probabilities, such as: SFP $\left(P_{sf}\right)$ and twin fault (P_{tw}) probability.

Generally, SFs occurs on the closed packed planes such as: (111) for fcc crystals, and that produces a shift in positions of the Bragg reflections in the XRD pattern. According to Paterson's theory (1952) due to SF the (111) Bragg reflection of any fcc crystal shift towards higher Bragg angle, whereas (200) approaches to lower Bragg angle, and this effect is just reverse for the 2^{nd} order Bragg reflection pairs i.e. (222) & (400). In general, the amount of peak shift only due to SF is very small and therefore, it is commonly measured with the pairs of opposite displacement of Bragg reflections such as: $(111\,\&\,220)$ or $(222\,\&\,400)$ instated of measuring the displacement of a single Bragg reflection. It is also important to be mentioned that the peak positions implies the positions of maximum intensity of Bragg reflections, not the positions of their center of gravity, and this is cautiously chosen by Warren (1959) to

eliminate the peak asymmetry part which mainly appears due to the presence of twin fault.

The shift in peak position of a Bragg reflection of a cold-worked material from its annealed specimen is mainly occur due to combined effect of presence of long range residue stress, SFs, and change in lattice parameter $(\Delta a/a_0)$ in the crystal structure. As the residue stress of a cold-worked material is very small as compare to the contribution of SFs, and therefore, the amount of peak shift can be written as (Wagner, 1966):

$$\delta(\Delta 2\theta)_{hkl}^{h'k'l'} = A_{hkl}^{h'k'l'}(\Delta a/a_0) + H_{hkl}^{h'k'l'}(\alpha' - \alpha'') \quad (2.25)$$

where, $\delta(\Delta 2\theta)_{hkl}^{h'k'l'} = \Delta(2\theta)_{hkl} - \Delta(2\theta)_{h'k'l}$

$$= (2\theta_{hkl} - 2\theta_{h'k'l})_{cw} - (2\theta_{hkl} - 2\theta_{h'k'l})_{ann} \quad (2.26)$$

The parameters, α' and α'' represents the intrinsic and extrinsic fault probability, respectively. The comparative peak shifts of the neighbouring pairs of Bragg reflections hkl and $h'k'l'$ for the cold-worked and annealed diffraction profiles are represented by $(\Delta 2\theta)_{hkl}^{h'k'l'}$. However, the estimation of SF probability (P_{sf}) using the amount of peak shift as determined form Eq. (2.26) has some disadvantage as we needs both the cold-worked as well as annealed specimens and also it involves only pairs of Bragg reflections with opposite displacement, whereas more number of Bragg reflections should be involved to achieve more accurate results. Thus, to avoid the necessity of an annealed and SF free specimen, another novel approach for determining the values of P_{sf} exists, which has also been adopted by several researchers to calculate P_{sf} in different austenitic steels (Talonen & Hanninen, 2007; Huang *et al.*, 2008). In this study we use austenitic steels, and therefore this novel approach (Talonen & Hanninen, 2007) of SF probability estimation was adopted in this study, and which is described below.

In absence of any long-range residual stress, it can be assumed that the peak positions of any specimen are mainly influenced not only due to any change in the lattice parameter according to Bragg's law, and the existence of SF in the microstructures also induced a shift in the peak positions. Therefore, the SF probability of low SFE materials can be sensibly determined by combining Bragg's law of diffraction with the peak shift of each Bragg reflections as obtained by Warren's planar fault theory (Warren, 1969) from the following relation (Talonen & Hanninen, 2007):

$$2\theta_{hkl} = 2arcsin\left(\frac{\lambda}{2d_{hkl}}\right) + \frac{90\sqrt{3}\,P_{sf}tan\theta_{hkl}}{\pi^2 h_0^2(u+b)}\sum(\pm)\,L_0 \qquad (2.27)$$

where, θ_{hkl} is the angular position of (hkl) Bragg reflections. The term, $\frac{1}{\pi^2 h_0^2(u+b)}\sum(\pm)\,L_0$ represent a fixed constant for each austenitic Bragg reflections (hkl), which are already available in the literatures (Warren, 1969). The inter-planar spacing of the faulted specimens and the wavelength of X-ray are represented by d_{hkl} and λ, respectively. The parameters were obtained simultaneously for each Bragg reflection (hkl) from the XRD pattern, and they were inserted in Eq. (2.27) to produce a set of five equations. The two unknown parameters, d_{hkl} and P_{sf}, were determined by the regression analysis of those five equations. It must be mentioned here that the effect of long-range residual stress on the direction dependent diffraction line shifts was insignificant and therefore, its contribution was assumed to be zero in the Eq. (2.27).

According to Wagner (1966), any type of asymmetrical broadening introduced in a diffraction profile is mainly due to presence of the twin fault and extrinsic SFs in the microstructure and therefore, it is possible to extract the information related to twin fault by critical analyzing the asymmetry of a diffraction peak. Like SF probability P_{sf}, the twin fault probability, P_{tw}, can be estimated from the amount of peak asymmetry component i.e. the amount of shift of the peak maxima (PM) from its center of gravity (CG) position. For austenite, the value of P_{tw} can be estimated from the amount of peak asymmetry of the two most prominent Bragg reflections (111) and (200). The peak asymmetry component of most prominent Bragg reflection of austenite can be expressed in terms of both, the twin fault and extrinsic SFs probability as (Cohen & Wagner, 1962):

$$\Delta_{CG}^{PM}(2\theta)_{111} = 11(4.5\alpha'' + P_{tw})\,tan\,\theta_{111} \qquad (2.28)$$

$$\Delta_{CG}^{PM}(2\theta)_{200} = -14.6\,(4.5\alpha'' + P_{tw})\,tan\,\theta_{200} \qquad (2.29)$$

where, $\Delta_{CG}^{PM}(2\theta)_{hkl} = CG(2\theta)_{hkl} - PM(2\theta)_{hkl}$

The CG of a diffraction peak can be easily determined from the numerical integration of the diffraction intensity profile and can be expressed as:

$$CG(2\theta)_{hkl} = \frac{\int_{2\theta_1}^{2\theta_2} (2\theta).\ I(2\theta)\, d(2\theta)}{\int_{2\theta_1}^{2\theta_2} (I(2\theta))\, d(2\theta)} \qquad (2.30)$$

where, $2\theta_1$ and $2\theta_2$ is the angular range over which the diffraction peak is extended. However, the background and instrumental component effect can be minimized in determination of P_{tw} by combining the above Eq. (2.28 & 2.29) in a more compact form as:

$$4.5\alpha'' + P_{tw} = \frac{\Delta_{CG}^{PM}(2\theta)_{111} - \Delta_{CG}^{PM}(2\theta)_{200}}{11\ tan\,\theta_{111} + 14.6\ tan\,\theta_{200}} \qquad (2.31)$$

Usually, the value of P_{tw} of a diffraction profile of austenite is determined using the relation given by the Eq. (2.31).

2.3 Transmission Electron Microscopy

The most effective and direct microscopic technique is known as transmission electron microscope (TEM), which is very much accomplished to do the microstructural characterization of any materials in great detail. Because of its resolving power and its simultaneous imaging capability in both space, the direct and Fourier space, it is widely used to study the crystal defects such as; dislocations, SFs, twin, grain boundaries and voids etc. that are present in a crystal. It is a direct observation method that helps to show the real images of different types of crystal defects, and at the same time its Fourier space image i.e. the diffraction pattern, which give the informations about the crystallographic orientations of that crystal defects. Therefore, by combining the images of crystal defect along with its crystallographic orientations one can gather a complete knowledge related to the defects, and that improve to understanding of the microstructure of the crystal. The basic TEM imaging principle and the underlying contrast formation mechanism are same for all types of crystal defects, and which basically exploits the effect of the strain fields associated to different types of defects on the electron scattering. However, TEM can be operated under different modes to meet the requirements of different experimental conditions, and the underlying principles related to different mode of operations are briefly presented in the following sections.

2.3.1 Contrast formation in transmission electron microscope

In general, TEM offers two contrast formation mechanisms, namely, phase contrast and diffraction contrast, which basically produce distinguishable image contrast for different types of defects. In case of phase contrast imaging mode, it is assumed that the crystals composed of parallel columns of atoms, and the electron beam is made parallel to those columns. The phase of the diffracted electron beams are preserved and produce high-resolution TEM (HRTEM) image i.e. HRTEM fringes by interfering constructively or destructively with the transmitted electron beams depending on their phase differences. Due to its very high resolution, the HRTEM is generally used to image the missing planes and the core structure of a dislocation. It is very much possible to identify the planes which are placed as close as 0.2 nm apart (Li, 2009) by using HRTEM. Another interesting fact is that a strain field mapping of a HRTEM microstructure is possible by masking a strong reflection in the first Fourier transform of the microstructure and then performing an inverse Fourier transform of that reflection, which is often known as geometric phase analysis (GPA). However, HRTEM technique can be applicable only for a limited area of the microstructure characterization topic, as it requires not only the dislocation line to be straight and parallel to the electron beam, but also its core remains same all over its entire length (Li, 2009; William & Carter, 2009). Therefore, imaging of dislocations with HRTEM is mostly restricted to dislocations with planar core structures as in the case of covalent crystals and the usage of HRTEM technique in the case of metallic materials is very minimal.

The diffraction contrast imaging technique is basically based on the exploitation of the effect of strain fields associated to different types of defects on the scattering of electrons that are diffracted by satisfying the Bragg diffraction condition. The occurrence of a dislocation in the microstructure causes a bend in the atomic planes in the lattice, and the bending is sufficient to produce an effective change in the path of the diffracted beam in the regions near the to dislocation, particularly at regions close to the core of the dislocation. The dislocation can be observed in TEM by tilting the specimen into a two-beam condition, and this two-beam condition can be achieved by exciting a strong diffraction vector $\vec{g}$ representing a specific set of crystallographic (hkl) planes. The two-beam condition can be confirmed form the selected area electron diffraction (SAED) pattern, which consists of only a diffracted beam than the direct i.e.

the transmitted beam and at exact two-beam condition both the beam will have exactly equal intensity. It is then tilted slightly away from the exact Bragg condition ($s = 0$) to a condition with some excitation error or deviation i.e. $s > 0$ so that the distorted planes near the core of dislocation can be brought into the Bragg condition, while the regions distant from the dislocation core are tilted away, as schematically presented in Fig. 2.2. However, in practical situation some of the scattered intensity from the regions that are not at the exact Bragg condition may still be visible due to broadening of Bragg peaks.

The contrast of dislocation image can be understood by the numerical value obtained from the scalar product of the diffraction vector $\vec{\mathrm{g}}$ and the lattice distortion vector $\vec{R}$, i.e. $\vec{\mathrm{g}}.\vec{R}$. In case of a pure screw type dislocation, $\vec{R}$ is directly proportional to the Burgers vector ($\vec{b}$) of the dislocation, and therefore, the values of $\left|\vec{\mathrm{g}}.\vec{b}\right|$ can be directly correlated to the observed contrast condition of the dislocation. In case of a pure screw type dislocation does not produce any strain contrast even if it satisfy $\vec{\mathrm{g}}.\vec{b} = 0$, and that can be understood due to the fact that the diffracting planes are parallel to $\vec{R}$. Interestingly, it is also found that for a value of $\left|\vec{\mathrm{g}}.\vec{b}\right| = 0$, no contrast is observed for a pure screw dislocation in the TEM micrograph, and this is known as the "invisibility" or "null" criterion in TEM studies. However, it is important to be mentioned here that the null condition i.e. $\left|\vec{\mathrm{g}}.\vec{b}\right| = 0$, is not always ensure a complete invisibility of an edge dislocations due to the existence of a "residual contrast", which mainly produces from the buckling regions of the glide planes associated with the displacement field of the edge dislocation. The amount of "residual contrast" can be determined from $\vec{\mathrm{g}}.(\vec{b} \times \vec{u})$, where $\vec{u}$ is the unit vector along the dislocation line. Therefore, a complete invisibility of an edge dislocations will happen only when both the scalar product value will be zero, i.e. $\left|\vec{\mathrm{g}}.\vec{b}\right| = 0$ & $\left|\vec{\mathrm{g}}.(\vec{b} \times \vec{u})\right| = 0$. It is evident that the contrast of a dislocation images is asymmetric in nature as long as the deviation parameter s is non-zero, and the diffraction contrast relative to the dislocation core strongly depends on the signs of both the parameters, s

& $\vec{g}.\vec{b}$ value. The occurrence of any changes in sign of any one the parameter shift the contrast across the dislocation core.

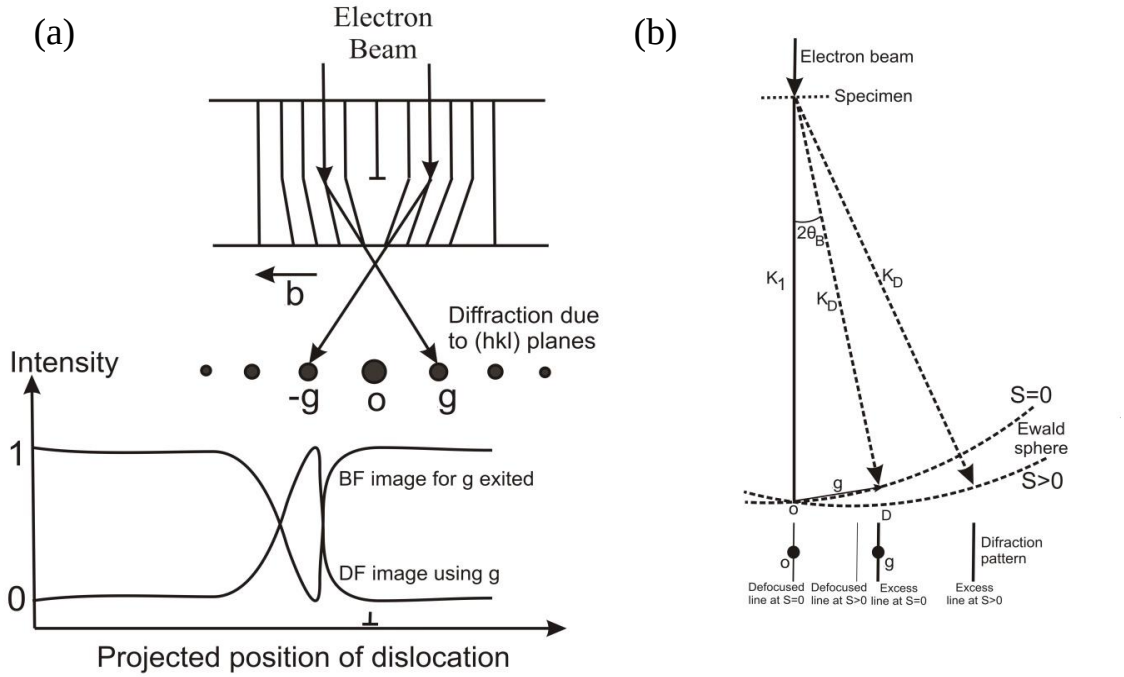

Fig. 2.2: (a) Schematic representing the diffraction into $\vec{g}$ and $-\vec{g}$ from a distorted planes near dislocation core. This diffraction condition is achieved only when the specimen is tilted slightly away from the Bragg condition ($s = 0$) to bring the distorted planes near the core into exact Bragg diffraction condition. Lower diagram depicts intensity profiles of the dislocation contrast away from its projected position when imaged with $-\vec{g}$ reflection. (b) Ewald sphere geometry for two beam diffraction condition with $s = 0$ and $s > 0$. Kikuchi lines are also indicated by vertical lines, which arise due to in-elastically scattered electrons. A pair of Kikuchi lines comprises of two lines, "excess" and "deficient" line. These lines help to set up the exact Bragg's condition. When $s > 0$, Kikuchi lines are on the opposite side of $\vec{g}$, and on the same side of $\vec{g}$ for $s < 0$ (William & Carter, 2009).

In general, TEM offers two basic operation modes, such as: bright field (BF) and dark field (DF) depending upon whether the transmitted or the diffracted beam is chosen to construct the micrograph by placing the objective aperture around it. In case of BF mode the objective aperture is placed such that it only pass the transmitted beam, while only diffracted beam is allowed in DF mode. The image of a dislocation appears as a dark line on a bright background in BF mode, while they appear as a bright line on a dark background in DF mode. The contrast of a dislocation appears only due to the

excitation of a diffraction vector, and the background contrast are due to the area of the hkl planes satisfying Bragg diffraction condition. The characterization of a dislocations i.e. its pure edge, screw, or mixed nature can only be identified by a detailed analysis $\left|\vec{g}.\vec{b}\right|$, and that can be done by systematic excitation of different $\vec{g}$ vectors associated with the glide planes. Interestingly, the BF and DF image contrast not only can detect the existence of unusual defects like SF tetrahedron, faulted dipoles, and multipoles, it can also help to study some peculiar microstructural features such as: jogs, kinks, interactions of dislocations with other dislocations or lattice defects etc. (William & Carter, 2009). There are different modes of operations, such as: multi-beam diffraction condition, two-beam diffraction condition, axial or cantered dark or bright field and off-axis dark field etc. Each of the above-mentioned techniques have its own merits and demerits depending on the requirement of the investigations.

The diffraction contrast imaging techniques also play a critical role to study the dislocation reactions and development of different dislocation structures in real time by using a special type of TEM holder, known as in-situ TEM specimen holder. In this experimental set up, generally a miniature tensile sample (less than 3mm in gauge length) is strained with the help of the in-situ TEM specimen holder inside of the microscope, and different defect activity such as: dislocation movements, dislocation-dislocation interaction, interactions with other defects, dislocation multiplication processes etc. which are occurring during the plastic deformation are observed and also recorded in real time. The in-situ experiments are very much powerful tools to study micro-processes that control dislocation mobility. Interestingly, the direct measurement of microstructural parameters such as: density of mobile dislocations, kinetics of movements or events, measurement of activation volume can be done by in-situ experiments, and it is also possible to observe metastable dislocation core configurations that exist only under stress. Finally, this is the only technique in which the direct observation can be made of processes like dislocations overcoming obstacles such as, precipitates, interfaces, etc. However, the in-situ experimental set up is very expensive, and not easily available in most of the laboratories.

2.3.2 Weak Beam technique in electron microscopy

Apart from the BF and DF mode of operation, the weak-beam (WB) transmission electron microscopy is another very important and successful method to get better resolution of a TEM micrograph. Basically, it is a special case of diffraction contrast imaging method in which the objective aperture is placed around a weakly excited Bragg reflection to construct the micrograph. As its name suggest that the intensity of the diffraction spot chosen for imaging is very weak when averaged over the imaging area, and this diffraction condition can be achieved by tilting the specimen or the incident beam far away from the exact Bragg diffraction in the two beam condition i.e. set the deviation parameter, $s \gg 0$ or $s \ll 0$. The diffraction condition of one such most successful WB method under Ewald sphere geometry is schematically presented in Fig. 2.3, which shows that tilting the incident electron beam rotated the Ewald sphere to satisfy the required $\vec{g} - 3\vec{g}$ conditions.

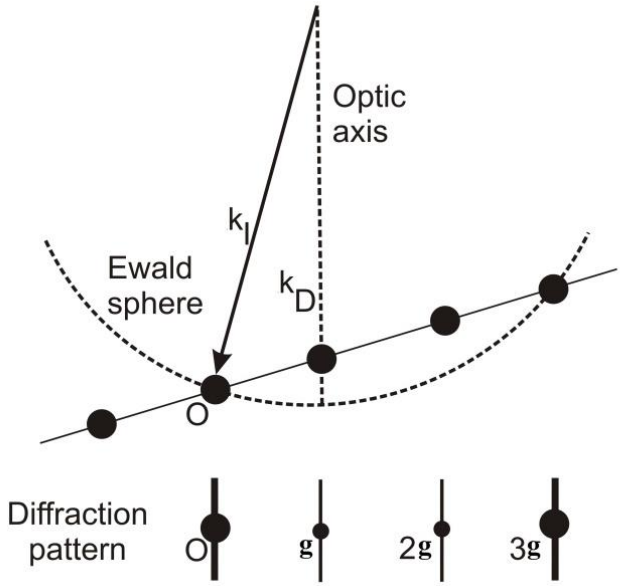

Fig. 2.3: Ewald sphere and positions of Kikuchi lines for the diffraction conditions (William & Carter, 2009).

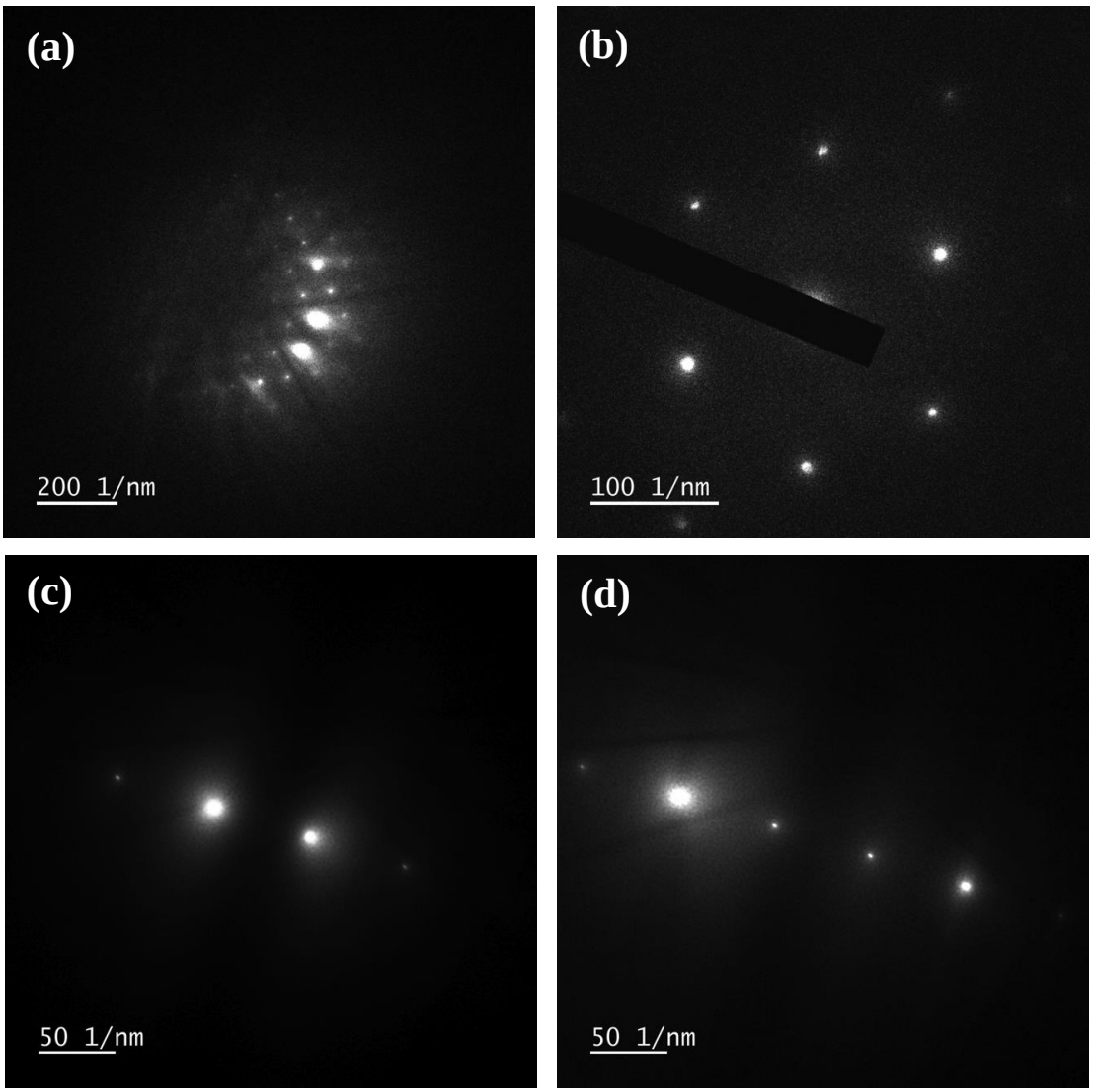

Fig. 2.4: Procedure of WBDF imaging technique showing each intermediary steps: (a) at far away from zone axis alignment, (b) at perfect zone axis alignment, (c) at two-beam condition, (d) at $\vec{g} - 3\vec{g}$ conditions after tilting the incident beam.

The WB technique mainly produce a DF image as it use weak diffraction spot to construct the image and therefore it has highest resolving power. In the weak-beam dark field (WBDF) diffraction condition, as shown in Fig. 2.3, the dislocations appear as bright and sharp lines with negligible intensity everywhere of the crystal plane, and interestingly the imaged lines are very close to the actual dislocation core. However, the establishment of diffraction condition of WBDF i.e. $\vec{g} - 3\vec{g}$ condition is very difficult and needs extremely good TEM operation skills. At first, the specimen is tilted to a particular zone axis, and then the two-beam condition is set up for BF/DF imaging.

Once the two-beam condition is achieved, then the incident illumination is tilted to rotate the Ewald sphere, and by observing the movement the Kikuchi lines cautiously an exact $\vec{g} - 3\vec{g}$ condition can be established. The entire method of WBDF technique obtained during one such TEM measurement is also summarized in Fig. 2.4, as a representative. Fig. 2.4(a) clearly indicates that the specimen is away from the zone axis, which lies at the center of the observed Ewald sphere, and a perfect zone axis alignment in Fig. 2.4(b) is achieved by tilting the specimen. Further, the two-beam and $\vec{g} - 3\vec{g}$ condition in Figs. 2.4(c-d) were achieved by tilting the specimen and primary electron beam, respectively. A critical observation of Fig. 2.4(a) & (d) also indicate the presence straight black lines which is basically known as Kikuchi lines, although both the lines of each pairs are not clearly visible.

In WBDF method, the incident illumination is tilted to rotate the Ewald sphere from the two-beam condition to produce a large deviation from its actual Bragg conditions i.e. a large value of deviation parameter, s, is obtained. Interestingly, the average intensity decreases at a rate of $\frac{1}{s^2}$ as s increases and the diffraction beam looks as a weak spot (William & Carter, 2009). The excitation distance will be small at large s value, and usually a deviation parameter value of ~ 0.2 nm^{-1} is always chosen as it satisfies all the conditions for sharp and narrow images of dislocations (William & Carter, 2009). Unlike the conventional DF imaging, the positions of dislocations imaged under WBDF condition are well defined with respect to their cores, and a dislocation pairs as close as ~1.5 nm can be easily resolved under the WBDF imaging (Veyssier, 1991). However, the resolution of the WBDF technique is limited due to the minimum volume of crystal (set locally in Bragg orientation) that causes a constructive interference (William & Carter, 2009). The WBDF technique is mostly useful for reviewing finely separated dislocations, specially the dissociation of a perfect dislocation where the distances between dislocation pairs are very small (of the order of nm). This characterization technique is very popular due to its high resolving power and its advantages over other DF imaging techniques. Once the value of s is fixed, then the width of a dislocation image is almost independent various factors, such as: diffraction vector, foil thickness, position of dislocations, excitation voltage etc., and therefore a lower uncertainties can be achieved for an elastically anisotropic crystals.

Despite of so many advantages of TEM characterization techniques, it has a major disadvantage related to the volume of the specimens. Generally, a typical TEM sample only characterizes a maximum volume of about 10^{-5} mm^3, and therefore questions arise about the reliability of TEM techniques while predicting deformation mechanisms of bulk materials. According to Veyssier (1991) a rough estimation of the defect density in TEM samples can be made by assuming that the density of dislocations is of the order of ~ 10^9 cm^{-2} while a sample is deformed to ~ 1% of strain. This implies that only examining a small fraction of dislocations of few centimeters length can describe the parameters related to the entire deformation process. However, the TEM characterization delivers the most wide-ranging and detailed analysis related to different defects, and it is the only tool that can reveal unusual slip systems and deformation processes which often occur in many alloys. Its imaging capabilities are better than other techniques, while the others characterization techniques may be used to substantiate its findings by sampling larger volumes of the specimens.

2.3.3 Geometric phase analysis (GPA)

Geometric phase analysis (GPA) is basically a digital signal processing method, which mainly used to determine many crystallographic parameters such as: interplanar spacing, strain and/or displacement components etc. from captured HRTEM microstructures. Interestingly, the estimated crystallographic quantities in GPA describe not only one particular point of the input HRTEM microstructures, it give the informations across the whole microstructures. It is well accepted that the presence of strong Bragg-reflections in the Fourier transform of an HRTEM microstructure characterize the quality of that microstructure, and the frequency components of the strong Bragg-reflections are related to the two-dimensional unit cell of the projected crystal structure. A perfect lattice gives only intense Bragg-spots in its Fourier transform i.e. sharp frequency components, whereas any distortion in the lattice spacing produce a diffusive Bragg-spots in the Fourier transform whose intensity centered around the frequencies corresponding to the mean lattice spacing. Now, the local lattice variation components can be easily determined by forming images generated from diffuse and strong Bragg-spots. The whole process of the strain filed mapping using GPA can be done by different computer packages, however in this study the Strain++

is used, which is basically an open source computer package and the detailed GPA algorithm of it is described by M. J. Hÿtch (Hÿtch *et al.*, 1998).

2.4 Electron Backscatter Diffraction technique

Other than XRD and TEM, electron backscatter diffraction (EBSD) is also an important quantitative microstructure characterization technique, which is basically based on the principle of a scanning electron microscope (SEM). It is generally used to obtain quantitative informations related to grain size distribution; crystallographic orientations with sub-micron spatial resolution and the informations related to crystallographic phases of the specimen. The EBSD image based on the Kikuchi diffraction patterns can be used for TEM study (Nishikawa & Kikuchi, 1928a, 1928b; Joy & Booker, 1971; Venables & Harland, 1973; Dingley, 1984) and its interpretation can be done by introducing the concept Hough transform for the obtained images (Schmidt *et al*., 1991; Lassen *et al*., 1992; Lassen, 1996). In case of EBSD, the atomic layers of a crystalline material diffract the accelerated electrons of the primary SEM beam, and those diffracted electrons is detected when they impact on a phosphor screen, and creates visible lines, called Kikuchi bands, or "EBSP's" (electron backscatter patterns). These patterns are basically the projections of the geometry of the lattice planes, and it contains the informations related to the crystalline structure and crystallographic orientation of the grains from which it is generated. From this patterns the crystallographic structure information for phases of interest are obtained with the help of a database, and it is further process with software to index the observed lines.

A highly flatten crystalline specimen with well-polished surface is needed in the SEM chamber to carry out the EBSD measurement. It is important to remember that resultant EBSD pattern produce best contrast only if the electron beam hit the sample at a grazing angle nearly 20 degrees, i.e. the sample-carrying stage should be inclined at 70 degrees, as shown in Fig. 2.5. The primary beam undergoes through an acceleration voltage of 10-30 kV using with an incident current of 1-50 nA. When the electrons of this primary beam impinge on the specimen surface then they scatter incoherent or quasi-elastically in all directions from the point of impingement of the specimen. The scatter electrons made an electron clouds near to the specimen surface, and that act as a divergent source of electrons from which some electrons can incident on crystal lattice at Bragg angle, and got diffracted. The diffracted electrons produce a

paired of large-angle cone for each crystallographic plane and the gnomonic projection of such diffracted cones are imaged on the detector.

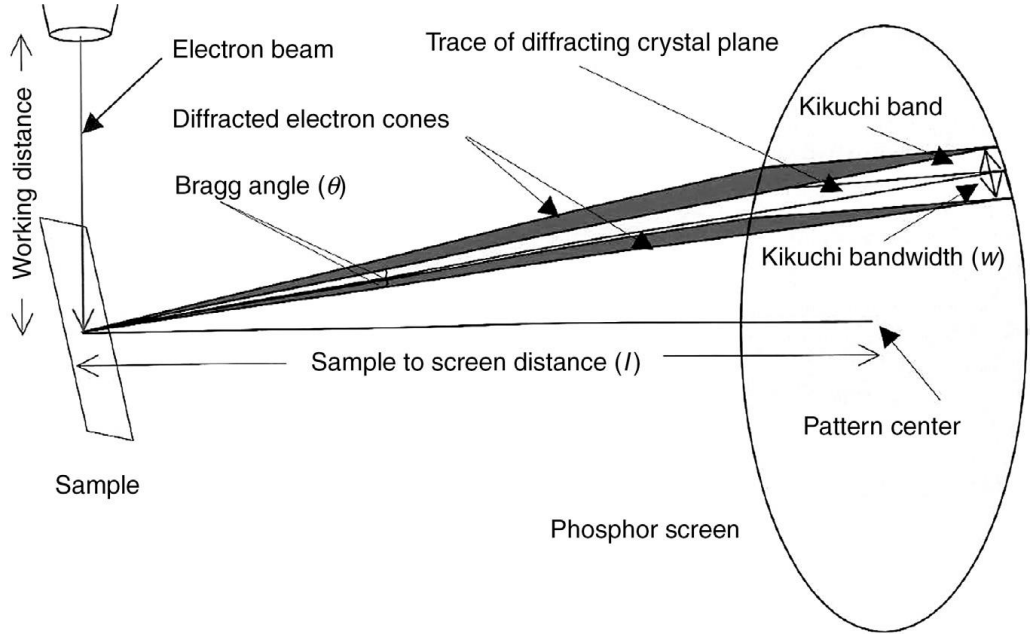

Fig. 2.5: Schematic representation of the detection setup for electron backscatter diffraction (EBSD) pattern (Pereira-da-Silva & Ferri, 2017).

The Kikuchi lines drops on the phosphor screen are electronically digitized and processed with the help of software associated with the instrument for further analysis to recognize the individual Kikuchi lines. It should be mentioned here that a good quality image of Kikuchi lines are generally observed from the thicker portions of the specimen with a very low density of crystal defects, whereas only diffraction spots will be seen for a very thin region of the specimen. The procedure of indexing an observed Kikuchi band is presented in Fig. 2.6, which demonstrate that only intense Kikuchi bands are recognized in Hough space by the brightest peaks, whereas the other peaks are more indistinct and nearly invisible. However, the sum of the total number of peaks detected under the Hough transform basically gives the Image Quality (IQ) value, and describe the quality of the EBSD pattern.

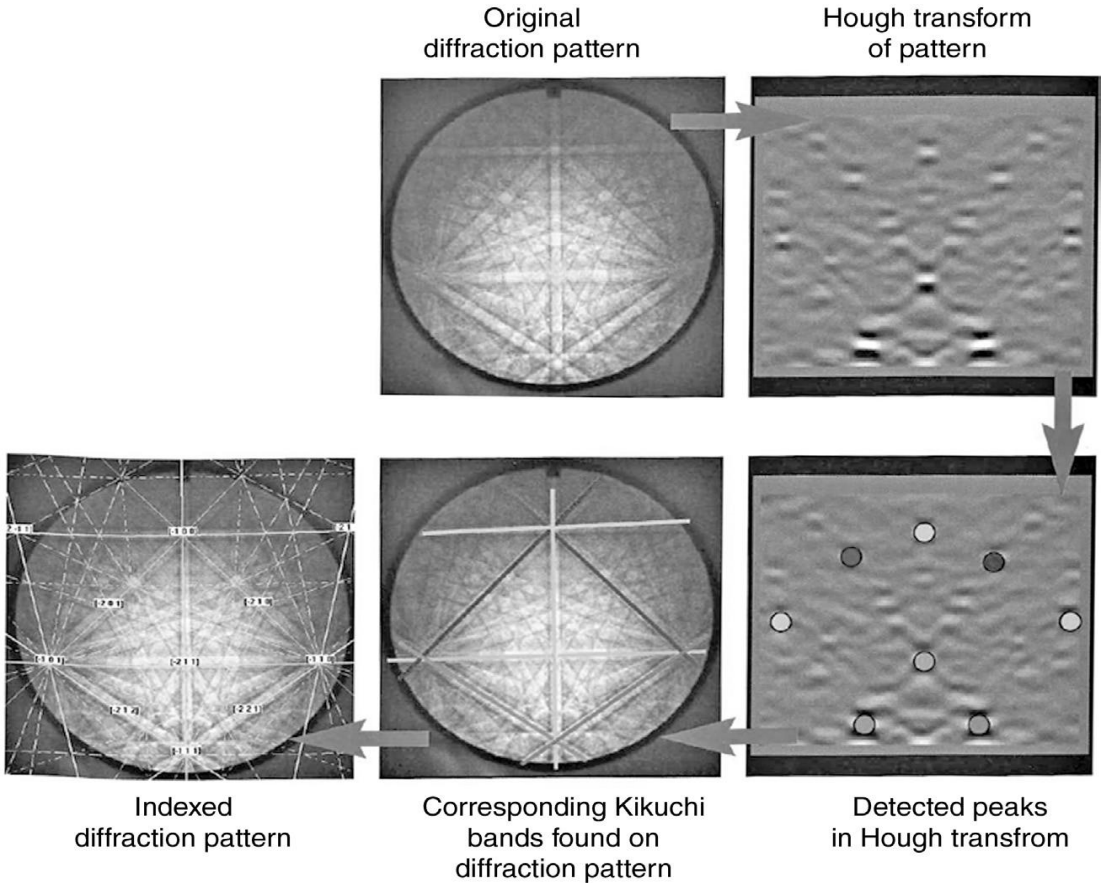

Fig. 2.6: The sequence of structural characteristics determination using EBSD technique that includes original diffraction pattern, Hough transformed pattern, peaks detected in the Hough transformation, corresponding Kikuchi bands found in the diffraction pattern, and indexed diffraction patterns (Pereira-da-Silva & Ferri, 2017).

At first, the ultrafine false peaks in the Hough space are neglected using peak detection algorithm, and then a line corresponding to each intense peaks is superimposed on the original image of the Kikuchi diffraction pattern. Now the width of the experimental Kikuchi bands will be matched with the expected broadest and narrowest Kikuchi bands as calculate for different crystallographic phases using software. The best-matched Kikuchi bands gives the informations related to the corresponding crystallographic phases present in the specimen. The EBSD technique is also useful to study the systematic textural relations between individual grains or phases, and it can construct true 3-dimensional orientations relationship of the individual crystals.

References

Barman, H., Hamada, A.S., Sahu, T., Mahato, B., Talonen, J., Shee, S.K., Sahu, P., Porter, D.A. & Karjalainen, L.P. (2014) *Metall. Mater.Trans. A.* **45**, 1937-1952.

Barret, C. S. (1952) *Imperfections in nearly perfect crystal*, Chap. III, John. Wiley, New York.

Bryne, J.G. (1965) *Recovery Recrystallization and Grain Growth*, McMillan CO, NY.

Cohen, J. B. and Wagner, C. N. J. (1962) *J. Appl. Phys.* **33 (6),** 2073-2077.

Dingley, D. J. (1984) *Scanning Electron Microscopy* **2**, 569-575.

Enzo, S., Fagherazzi, G. Benedetti, A. & Polizzi, S. (1988) *J. Appl. Crystallogr*. **21**, 536-542.

Garabagh, M. R. M., Nedjad, S.H., Shirazi, H., Mobarekeh, M.I. & Ahmadabadi M.N. (2008). *Thin Solid Films.* **516**, 8117-8124.

Gevers, R. (1954a). *Acta Cryst.* **1**, 337-343.

Gevers, R. (1954b). *Acta Cryst.* **1**, 740-744.

Greenough, G. B. (1952) *Prog. Metal. Phys.* **3**, 176-219.

Huang, B. X., Huang, X. D., Wang, L. & Rong, Y.H. (2008) *Metall. Mater. Trans*. A. **39A**, 717-724.

Hÿtch, M. J., Snoeck, E. & Kilaas, R. (1998) *Ultramicroscopy* **74**, 131-146.

Joy, D.C. & Booker, G. R. (1971) *J Phys E Sci Instrum* **4**, 837.

Keijser, de Th. H. & Mittemeijer, E. J. (1980) *J. Appl. Cryst.* **13**, 74-77.

Kim, J. Y., Lee, S. J. & De Cooman, B.C. (2011) *Scr. Mater*. **65**, 363-366.

Lassen, N. C. K. (1996) *Mater Sci Technol*. **12**, 837-843.

Lassen, N. C. K; Jensen, D. J. & Conradsen, K. (1992) *Scanning Microsc*. **6**, 115-121.

Li, X.W. (2009). *Adv. Mater. Res*. **79:82**, 215-218.

Mittemeijer, E. J. & Delhez, R. (1978) *J. Appl. Phys*. **49**, 3875-3878.

Nishikawa, S. & Kikuchi, S. (1928a) *Nature* **122**, 726-726.

Nishikawa, S. & Kikuchi, S. (1928b) *Nature* **121**, 1019-1020.

Paterson, M. S. (1952) *J. Appl. Phys.* **23**, 805-811.

Pereira-da-Silva, M. de Assumpçao. & Ferri, F.A. (2017) Scanning electron microscopy
Nanocharacterization Techniques, William Andrew Publishing, 1-35.

Ray, I.L.F. & Cockayne, D. J. H. (1971) *Proc. R. Soc. Lond. A*. **325**, 543-554.

Sahu, P., Shee, S. K., Hamada, A. S., Rovatti, L., Sahu, T., Mahato, B., Ghosh Chowdhury, S., Porter, D.A. & Karjalainen, L.P. (2012) *Acta Mater*. **60**, 6907-6919.

Scherrer, P. & Gottinger Nachrichten (1918) **2**, 98-100.

Schmidt, N. H; Bildesorensen, J. B. & Jensen, D. J. (1991) *Scanning Microsc*. **5**, 637-643.

Stokes, A. R. (1948). *Proc. Phys. Soc., Lond.* **61**, 382-391.

Talonen, J., & Hanninen, H. (2007) *Acta Mater*. **55**, 6108-6118.

Ungár, T. & Borbe´ly A. (1996) *Appl. Phys. Lett.* **69**, 3173-3175.

Ungar, T. & Ribarik, G. (2017) IOP Conf. Ser. Mater. Sci. Eng. **194**, 1-8.

Ungár, T. (2001). *Mater. Sci Eng. A.* **309-310**, 14-22.

Ungar, T., Dragomir, I., Revesz, A., Borbely, A. (1999) *J. Appl. Crystallogr*. **32**, 992-1002.

Ungár, T., Groma, I. & Wilkens, M. (1989). *J. Appl. Cryst.*, **49**, 26-34.

Ungár, T., Ott, S., Sanders, P., Borbély, A. & Weertman, J.R. (1998). *Acta Mater*. **46**, 3693-3699.

Ungar, T., Revesz, A. & Borbely, A. (1998) *J. Appl. Crystallogr*. **31**, 554-558.

van Berkum, J. G. M., Vermeulen, A. C., Delhez, R., de Keijser, Th.H.. & Mittemeijer, E. J. (1994). *J. Appl. Cryst.* **27**, 345-357.

Venables, J. A. & Harland, C. J. (1973) *Philos. Mag.* **27**,1193-1200.
Veyssier, P. (1991). *ISIJ International.* **31**, 1028-1048.
Wagner, C. N. J. *Local Atomic Arrangements studied by X--ray Diffraction* (AIME, NewYork, 1966), Vol. 36, Chap.7.
Warren, B. E. & Averbach, B. L. (1950) *J. Appl. Phys.* **21**, 595-599.
Warren, B. E. & Averbach, B. L. (1952) *J. Appl. Phys.* **23**, 497-498.
Warren, B. E. (1959) *Prog. Met. Phys.* **8**, 147-202.
Warren, B. E. (1969) *X-ray diffraction*, Addison-Wesley, Reading, Mass.
Wilkens, M. (1970) *Phys. Status Solidi* (a) **2**, 359-370.
Wilkens, M. in: J.A. Simmons, R. de Wit, R. Bulloug (Eds.), (1970) Fundamental Aspects of Dislocation Theory Vol. II, Natl Bur. Stand. Publ., Washington, 1195-1221.
William, D.B. & Carter, C.B. (2009) *Transmission Electron Microscopy*, second ed., Springer Science, NY, Vol-3.
Williamson, G.K. & Hall, W.H. (1953) *Acta Metall*. **1,** 22-31.

Part B

Materials and their SFEs

*Chapter 3**

Materials processing, initial microstructure & their mechanical responses

*This chapter is published in Scripta Mater., 192 (2021) 83-88, Materials Letters, 285 (2021) 129002 & 327 (2022) 133006. (No.1, 2 & 3 in the list of publications)

3.1 Materials, their processing and characterization

A high-Mn steel with the nominal chemical composition: Fe–16Mn–1.5Al–0.3C (all compositions are in wt.%) was prepared by induction furnace melting followed by homogenization. It was then hot rolled at 1100°C with subsequent water quenching, and finally cold rolled by 50% reduction into 2.5 mm sheets. The heat treatment of the cold rolled sheets was done under protective argon environment at different conditions to produced required grain size variations, and finally water quenched to room temperature (RT). The cold rolled sheets were annealed in a Gleeble 3800 thermomechanical simulator at 750°C for 120s to obtain a graded grain structure. After heat treatment the initial microstructure was studied using electron backscatter diffraction (EBSD) (Carl Zeiss Ultra plus, 20 kV and 30 nA) to ensure that the heat treatment condition produce the required graded grain distribution. Similarly, another heat treatment was also done at 1000 °C for 300 s to produce a coarse grain (CG) structure with the average grain size ~ 25 μm, and the initial microstructure were also studied using EBSD. Interrupted fatigue tests with flat hour-glass type specimens were carried out at room RT using a constant deflection at 23 Hz (Hamada *et al*., 2009; Karjalainen *et al*., 2012). The specimens were designed according to ASTM D 3479 standard, and the specimen design with dimensions (in mm) is also given in Fig. 3.1. The applied bending moment was converted into applied stress amplitude, and it found that the value of the applied stress amplitude for graded grain specimen is ~ 560 MPa, whereas it was ~ 400 MPa in case of CG specimen. These conditions are known to correspond to the fatigue limit of the respective TWIP steels (Hamada *et al*., 2009). The tests were interrupted at different cycles for microstructural investigations and hardness measurement. The Vickers microhardness (H_v) of the specimens were measured after each interrupted fatigue cycles at five different locations of the gauge region using a load of 9.8 N.

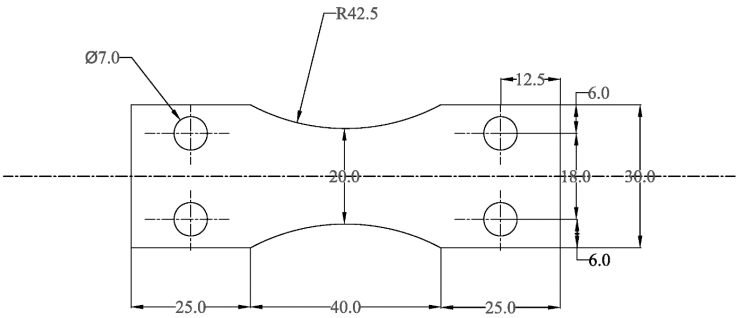

Fig. 3.1: Fatigue specimen design with dimensions (in mm)

Furthermore, a medium-Mn (MMn) steel with a chemical composition of Fe-0.17C-2.2Si-10.8Mn-18.0Cr-4.7Ni-0.9V-0.25N (all in wt.%) was also studied in this dissertation. The alloy design of the studied MMn steel was predominantly based on two important factors; one of them is the enhancement of its corrosion resistant property, while other one deals with the improvement its mechanical property. Interestingly, the studied MMn steel with above mentioned chemical compositions not only demonstrate a stability between its corrosion and superior mechanical properties, but also its corrosion resistant property was significantly improved and which is far better than the corrosion resistant property of any other conventional TWIP steels (Allam et al., 2019). The manufacturing route comprised of ingot-casting, hot and cold rolling processes down to a final thickness of 1.5 mm, followed by an annealing heat treatment at 1200°C for 3 min. It should be mentioned here that the parameters related to heat treatment were intentionally chosen based on the thermodynamic calculations to introduce only one type of precipitates *i.e.*, V (C, N) in the austenitic matrix (Allam et al., 2019). After heat treatment the initial microstructure was investigated using electron backscatter diffraction (EBSD) in a Zeiss Sigma field emission gun (FEG) scanning electron microscope (SEM) equipped with EDAX-TSL Hikari detector at an accelerating voltage of 15 to 20 kV with a probe current of 30 nA. Before any EBSD measurement, the annealed specimens were electro-polished at room temperature for 20 s at 22 V using an electrolyte consisting of 700 mL ethanol, 100 mL butyl glycol, and 78 mL 60%-perchloric acid. The EBSD scans of the annealed specimens were performed with a 150 nm step size and the resulting microstructures were analysed to ensure the existence of a single austenitic phase in the matrix, whereas the occurrence of V(C,N) precipitates can be confirmed under TEM investigations. Mechanical tests were carried out at RT with flat hour-glass type specimens of standard A30 defines having a parallel gauge length of 30 mm and 6 mm width. Quasi-static uniaxial tensile tests were carried until failure with a strain rate of 10^{-3} s^{-1} using a Zwick Z 100 tensile testing machine (Zwick Roell, GmbH) to study the mechanical properties of the designed MMn steel, and the test was also interrupted at 0.02 true strain to identify the early deformation mechanisms.

To interpret the deformation microstructure the gauge regions of the differently deformed specimens were cut into pieces with a feeding speed of 0.005 mm/s by using Secotom-20 operating at lowest wheel speed of 500 rpm. These cutting conditions were

deliberately chosen to avoid the influence of any additional deformation on the different microstructural parameters, which may be produced during the cutting process. The trimmed portion of the specimens was electropolished before X-ray diffraction (XRD) investigations, and the XRD data acquisitions for the angular range of 40º - 150º were carried out with a Bruker D8 Advance laboratory X-ray powder diffractometer using CuK_{α} radiation operating at 40kV under the Bragg-Brentano geometry with a scan speed of 0.3°/min, and fixed step size of 0.01. Such a slow scans speed for XRD measurements were intentionally chosen to get more data points, and which is a necessary condition for a suitable outcome from XLPA analysis. The instrumental broadening and the peak shape parameters were evaluated from the X-ray powder patterns of LaB6, NIST SRM660b specimen. Special precautions have been taken while preparing specimens for TEM observations to minimize any types of external strain influence on the microstructures, and which are described below.

After XRD measurement, the specimens were also mechanically grounded to about 100 μm thickness using different grits of SiC papers, starting from 500 to 2000 in Tegramin-25 operating under normal water stream with an applied force of 5 to 10 N. To minimize the bend contours effect, which mainly produced due to disparity in applied force during polishing, few 3 mm disks were punched from the 100 μm foil prior to final polishing. Before any electrolytic thinning, the disks were implanted in the cylindrical tunnel of ASTEN, a special insert for AccuStop 30, for further polishing of about 20 μm using 4000 grit SiC papers with a minimal applied force of 5 N. Then 3 mm disks were finally electropolished in a TenuPol–5 operating at 30 V DC and 40 mA using a solution of 90% methanol and 10% perchloric acid maintained at -20°C. The TEM observations were carried out on a JEOL 2200FS electron microscope operating at 200 kV and equipped with a GATAN 994UltraScan® 1000XP imaging system.

3.2 Initial microstructure

The high-Mn steel demonstrated only a single-phase austenitic structure comprised of different grain sizes, which basically directly correlated to the parameters related to the heat treatment process. The pre-deformation microstructure of the high-Mn steel with different grain sizes were investigated using EBSD, and the outcomes of the investigations are demonstrated in Fig. 3.2. The EBSD inverse pole figure (IPF) map

of the initial recrystallized grains in Fig. 3.2(a) and its corresponding grain size distribution are also presented in Fig. 3.2(b). It is important to be mentioned here that during grain size measurement we have counted the annealing twin boundaries (TB) as grain boundaries. Interestingly, the IPF map in Fig. 3.2(a) along with the grain size distribution in Fig. 3.2(b) clearly establish that the heat treatment condition imposed on the specimen successfully produce a mixture of different grains without any pronounced texture. However, a careful observation of Fig. 3.2(b) suggests that the scan areas are mostly covered with finer grains of grain size ~ 2 μm, and except from the finer grains few larger grains of grain size ~ 5 μm are also observed, although the population density of the larger grains are minimal. Similarly, the EBSD IPF map of the CG specimen is presented in Fig. 3.2(c) and the corresponding grain size distribution are also presented in Fig. 3.2(d). It is clearly evident from Fig. 3.2(d) that the scan areas consist of quite large grains of grain size ~ 25 μm, whereas the IPF map in Fig. 3.2(c) directly reveals that the grains are randomly oriented i.e., no pronounced texture is present in the microstructure. Hence, the above EBSD investigations of the pre-deformation microstructure of the high-Mn steels advocates towards the fact that the used material processing methods successfully produces the desired specimens for the present study.

Similarly, the initial microstructures of the medium-Mn steel also demonstrate a single-phase austenitic matrix like the studied high-Mn steel, and which mainly correlated directly to the parameters related to the heat treatment process. The as-annealed microstructures of the medium-Mn steel was studied using EBSD and TEM, and the outcomes of the investigation is demonstrated in Fig. 3.3. The EBSD inverse pole figure (IPF) map of the initial recrystallized grains in Fig. 3.3(a) and its corresponding grain size measurement indicate that the applied annealing treatment produce an average grain size of ~ 20 μm with without any pronounced texture. The presence of large number of white lines in Fig. 3.3(a) also indicates that the applied annealing treatment also produce numerous annealing twins in the microstructure, and it is important to be mentioned here that during grain size measurement we have not counted the annealing twin boundaries (TB) as grain boundaries.

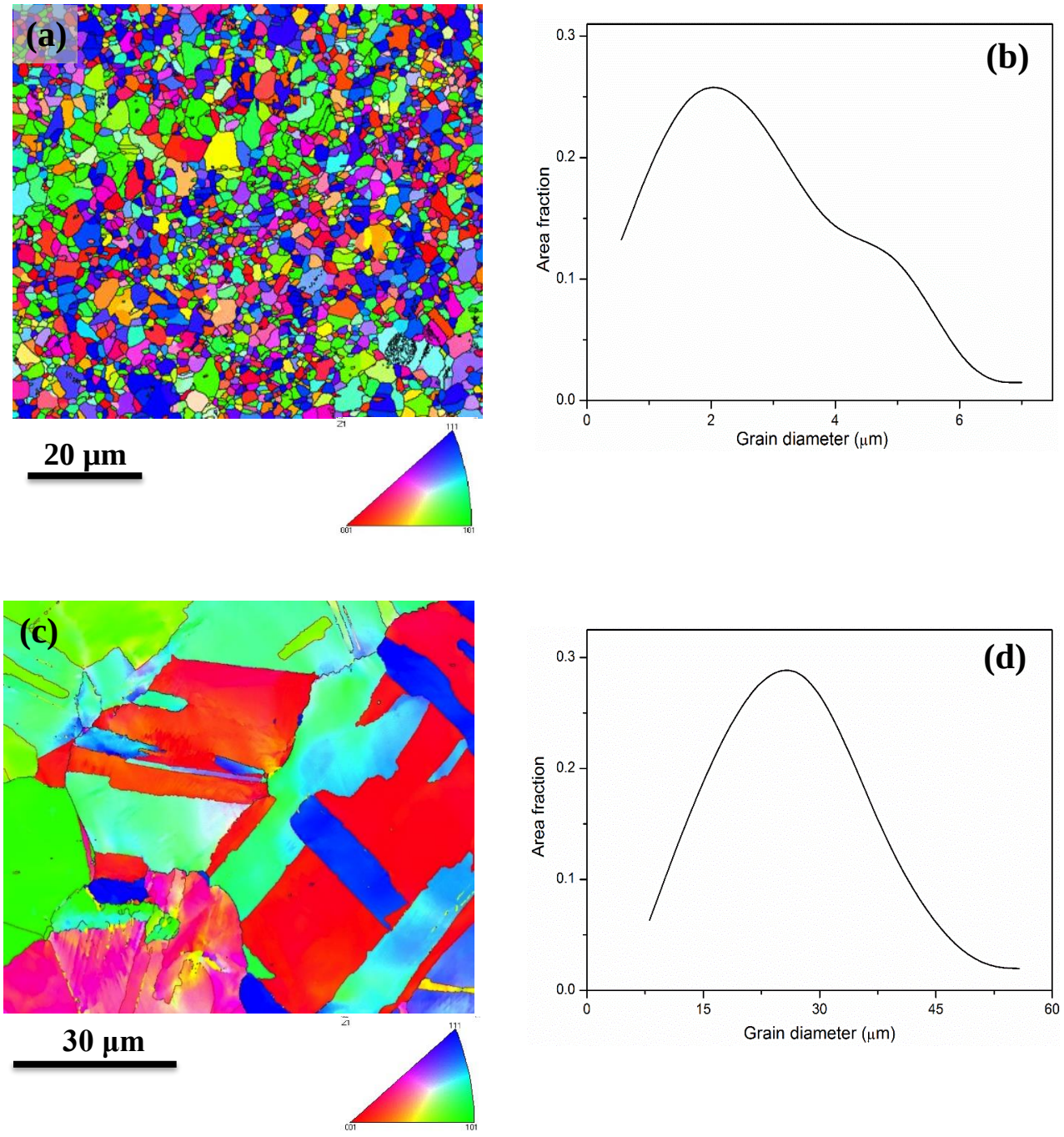

Fig. 3.2: Initial EBSD microstructures showing the EBSD IPF maps with its corresponding grain size distributions for (a,b) graded grain and (c,d) coarse grain (CG) specimen.

A low magnification TEM BF micrograph of the medium-Mn steel after heat treatment condition was obtained along $[01\bar{1}]$ zone axis and presented in Fig. 3.3(b), which clearly demonstrate the occurrence of precipitate in the austenite matrix. The precipitate in the austenite matrix was also identified from the SAED pattern obtained along $B \approx [01\bar{1}]$ zone axis, and the indexed SAED pattern corresponding to the TEM micrograph is also presented as inset in Fig. 3.3(b) which clearly indicate that the V(C,N) precipitates have a cube-cube orientation relationship with the austenite matrix, and that also support the previous observations made by Kwon et al. (2019). Interestingly, a careful observation of Fig. 3.3(b) also suggest that the observed V(C,N) precipitates are nearly spherical or rectangle in shape with a size range remain in between: 160-290 nm, and which is significantly larger than the precipitates observed by Kwon et al. (2019), whereas cementite remained absent. However, the V content in the precipitates varies in between: 65-70% (wt. %), and which was determined from the histogram obtained from energy dispersive X-ray spectroscopy (EDS) unit integrated with the TEM, and the obtained histogram to the corresponding V(C,N) precipitates observed in Fig. 3.3(b) is also presented in Fig. 3.3(c). The absence of cementite and the occurrence of larger precipitates size in the microstructures can be attributable in terms of relatively higher annealing temperature and time used in the present study as compared to the study made by Kwon et al. (2019). Furthermore, the difference in the observed as annealed microstructure between the present study and Kwon's study (Kwon et al., 2019) may also be understandable due to the major differences in the chemical compositions of the studied steel, namely, C, Si and Cr contents, and which may have some influence to the microstructures. A critical observation of Fig. 3.3(b) also indicates towards an interesting fact that the precipitates in Fig. 3.3(b) are not surrounded by any significant dislocations, unlike in the deformed state; and the importance of it will be critically introspected under TEM investigations of the deformed specimens in Chapter 6.

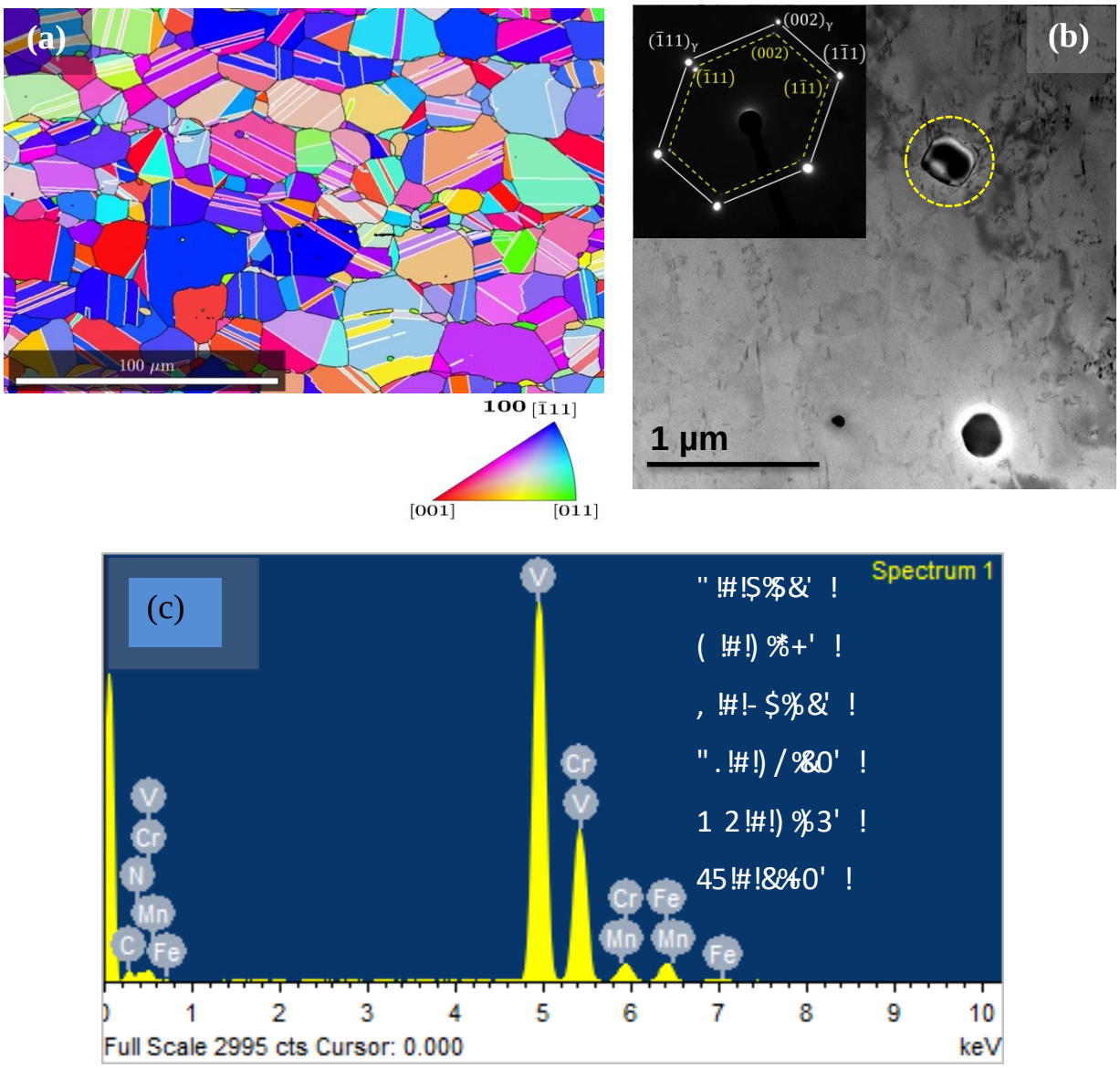

Fig. 3.3: The initial microstructure of the investigated meduim Mn steel showing: (a) EBSD inverse pole figure map of the initial microstructure with average austenite grain size ≈ 20 μm, (b) low magnification TEM BF microstructure in the annealed undeformed condition. The inset shows an indexed B≈ [011] SAD pattern of the matrix and precipitate in a cube-cube orientation: $[110]_{\gamma}$ ||$[110]_{V(C,\ N)}$, (c) EDX spectrum acquired with a nano probe on the precipitate within the encircled area of (b) and the corresponding elemental analysis in wt%.

3.3 Mechanical responses

The cyclic deformation behavior of high-Mn steel is often interpreted using the variation of measured Vickers microhardness with number of fatigue cycles. Thus, the mechanical responses of the studied high-Mn steels under cyclic deformation are presented in Fig. 3.4, which clearly demonstrate the variation of the measured microhardness value with the number of fatigue cycles. Fig. 3.4 clearly demonstrates that both the graded grain and CG specimen show almost similar kind of cyclic response. A rapid increase in the microhardness value was observed within the 10–20% of the expected fatigue life of the high-Mn steels (Karjalainen *et al*., 2012), and then the microhardness almost gets saturate. However, a careful observation of the Fig. 3.4 reveals that the initial microhardness value of the graded grain specimen is ~ 264 H_v, whereas it is quite low ~ 180 H_v in case of the CG specimen. It is also expected as we all know that the grain refinement increases the yield strength of the material by well known Hall-Petch relation (Hall, 1951; Petch, 1953), and therefore the initial microhardness of the graded grain specimen is quite higher than the CG specimen. The amount of measured microhardness in saturation is approximately ~ 8.6 % of the initially measured microhardness value for the graded grain specimens, whereas this increment is quite large ~ 19 % in case of the CG specimens.

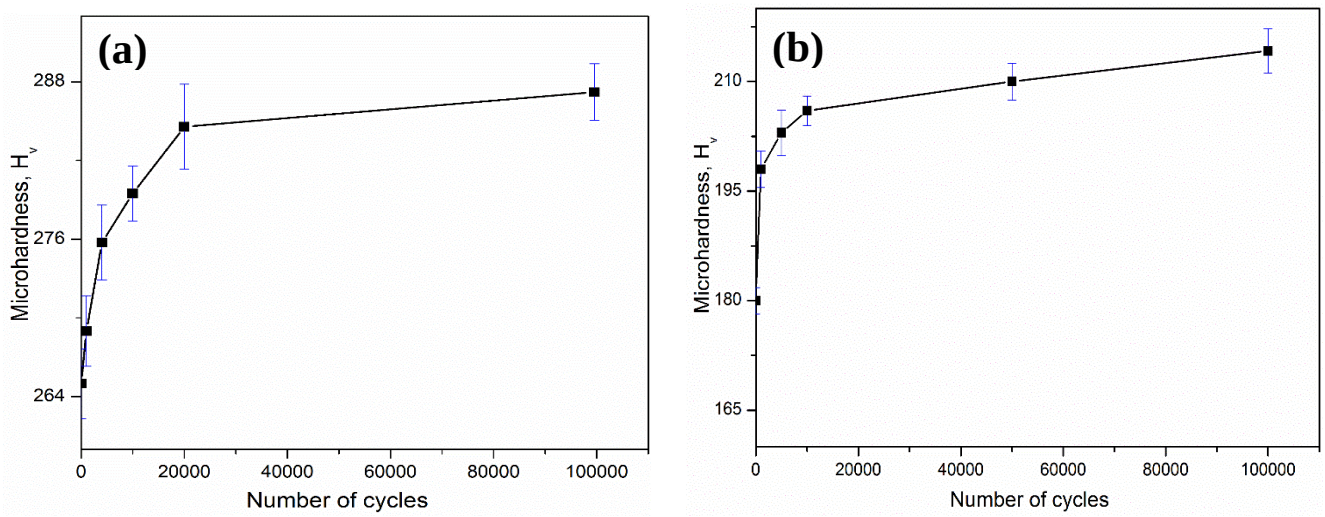

Fig. 3.4: The cyclic response of the studied steels in terms of microhardness vs number of fatigue cycles for (a) graded grain and (b) coarse grain specimen.

The cyclic response of the graded grain specimens presented in Fig. 3.4(a) shows that initially the microhardness rapidly increases from 264 H_v to 284 H_v for the first 20000 cycles, and thereafter the microhardness value almost saturates reaching only to 286 H_v at 100000 cycles. Such rapid increment in the microhardness value clearly indicates that cyclic hardening occurs during the first 20000 cycles. Since the microhardness value saturates after 20000 cycles, thus to understand the microstructural difference and its influence on the cyclic response the microstructural investigations were restricted to 10000 and 100000 cycles representing the pre-saturation and saturation stages, respectively. Similarly, the cyclic response of the CG specimens is presented in Fig. 3.4(b), which clearly indicates that the microhardness rapidly increased from 180 H_v to 206 H_v during first 10000 cycles, and thereafter it almost remains saturate upto 100000 cycles. However, a critical observation of Fig. 3.4(b) reveals that microhardness increasing marginally to 214 H_v after 100000 cycles. Thus, in case of CG specimen the microstructural investigations were restricted to 5000 and 100000 cycles, representing the fast hardening (pre-saturation) and slow hardening (saturation) stages, respectively. The microstructural investigations of the above-mentioned high-Mn steel deformed at different fatigue cycles, and the interpretation of the cyclic deformation behaviour in terms of deformation microstructures are critically described in chapter 5.

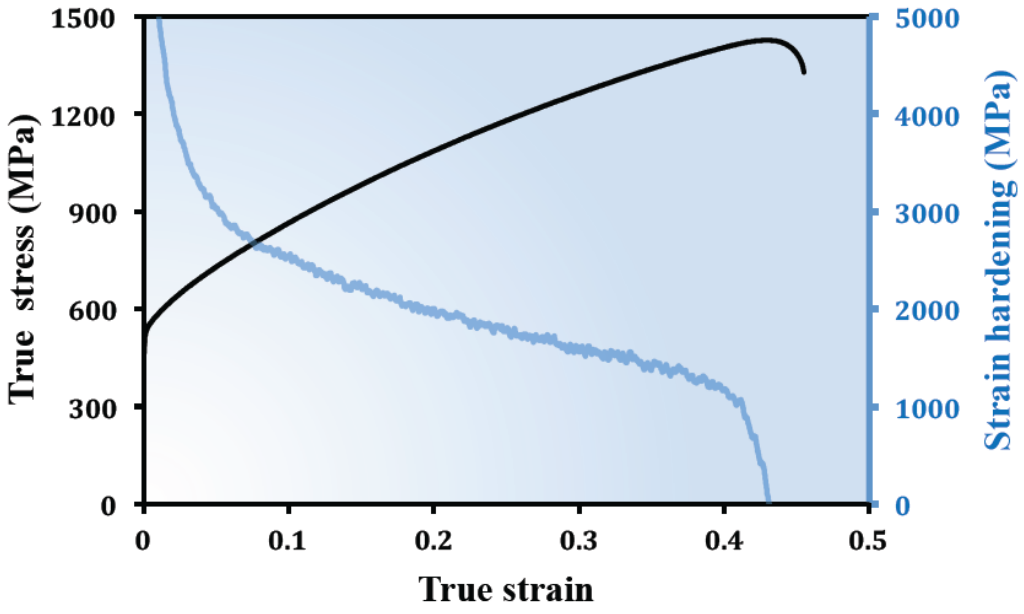

Fig. 3.5: Monotonic flow stress response and corresponding strain hardening rate vs. true strain plot.

The monotonic true stress–true strain tensile flow behavior and its corresponding strain hardening rate (SHR) of the investigated medium-Mn steel are superimposed and depicted in Fig. 3.5. The quasi-static tensile properties of the studied medium-Mn steel, such as: yield strength (YS), ultimate tensile strength (UTS) and total elongation can easily be found from the flow-stress behaviour plotted in Fig. 3.5. It is readily seen from Fig. 3.5 that the applied annealing treatment conditions led to a total elongation of ~ 45% along with a YS value of ~ 600 MPa, and which clearly reveals that the studied medium-Mn steel can be easily use with satisfactions for most kind of cold formability applications. Careful observations of Fig. 3.5 also suggest that the studied medium-Mn steel has somewhat comparable mechanical properties that of the conventional TWIP steel of the same grade, such as: X60MnAl17-1, whose corrosion resistant property was significantly improved by reducing Mn content and adding Cr, N and V content (Allam et al., 2019). The studied medium-Mn steel also possess a high initial SHR of ~ 3.9 GPa at a true strain of ~ 0.02, however, it decreases gradually to ~ 1.37 GPa while the true strain increases to ~ 0.37. Since, the studied medium-Mn steel have maximum SHR at a true stain level of ~ 0.02, therefore our investigations mainly focused at this strain level to indentify the activated deformation mechanism at this early stage of deformation, and which was greatly introspected under TEM investigations in chapter 6.

References

Allam, T., Guo, X., Sevsek, S., Lipińska-Chwałek, M., Hamada, A., Ahmed, E., Bleck, W. (2019) *Metals* **9(6)**, 705.

Hall, E. O. (1951) *Proc. Phys. Soc. Lond. B* **64**, 747-753.

Hamada, A.S., Karjalainen, L.P. & Puustinen, J. (2009) Mater. *Sci. Eng. A*. **517**, 68-77.

Kwon, Y., Zargaran, A., Ryu, J.H., Kim, N.J. (2019) *Scr. Mater*. **172**, 125–129.

Karjalainen, L.P., Hamada, A., Misra, R.D.K., Porter, D.A. (2012) *Scr. Mater.* **66**, 1034-1039.

N. J. Petch. (1953) *J. Iron. Steel. Inst.* **174**, 25-28.

Chapter 4*

Determination of SFEs of the selected steels

* This chapter is unpublished.

4.1 Methods of SFE estimation

The SFE of a material can be estimated using different computational as well as experimental methods. It must be mentioned here that there are basically two computational approaches, such as: thermodynamic approach and ab-initio approach, as mentioned in §1.5, whereas, the SFE can be directly determined experimentally by using the true potential of two different TEM imaging techniques such as: HRTEM and WBDF technique, although it can also be done only by measuring the radius of extended dislocation nodes operating in BF mode. However, each of the above-mentioned TEM techniques have it's own merits and demerits. Generally, the HRTEM technique is the most direct method for measuring SFE, since it directly measures the fault width from the cross-section (Balk & Hemker, 2001), but it has few inescapable drawbacks. An extremely thin sample region is essential to satisfy the weak phase-object approximation (WPOA) for HRTEM imaging (William & Carter, 2009), and which directly advocated towards the fact that not only the SFE value is estimated from a very limited area of the specimen, it also significantly influenced by the surface effect of the specimen. Still, HRTEM might be the only direct method to determine the SFE for the materials having very high SFE due to its high point resolution (Balk & Hemker, 2001).

Whelan (1958) first describe that SFE can also be determined from an extended threefold node by balancing the force between node arms and faulted regions. Although, the main challenge of this method is finding isolated and symmetrical dislocation nodes, which are often asymmetric in nature or non-uniform in size (Pierce *et al*., 2014). Another very challenging and tedious TEM method is the determination of a dissociation width of a Shockley partials using WBDF imaging technique, and once the width is measured then SFE can be easily estimated using simplified approach (Cockayne *et al*., 1971). Though, this method is restricted to low SFE material and very early stages of deformation, only when a perfect dislocation dissociates into a pair of parallel partial dislocation and the separation width is measurable. Another difficulty in WBDF technique is finding of partial dislocations parallel to each other, because in reality most of the partial dislocation arrangements contain curvature and kinks. SFE can also be estimated with a considerable accuracy by XLPA, but this method is often criticized due to its indirect nature that is established on some oversimplified postulates.

The underlying principle of each aforementioned experimental methods are briefly described subsequently.

4.1.1 Indirect approach

At first, Schramm & Reed method (1975) determine the SFE of a material indirectly by correlating the different microstructural parameters, which can be easily determined from XLPA, as described briefly in § 2.2. According to them, the SFE can be estimated only by utilizing the mean square strain $\langle \varepsilon_L^2 \rangle$ of a deformed austenite specimen associated along most prominent crystallographic direction $\langle 111 \rangle$ averaged over a coherence length $L = 50$ Å and the stacking fault probability i.e. P_{sf} value. However, the presence of any strain anisotropy in the microstructure is neglected in Schramm & Reed (1975) SFE estimation method, therefore it was modified by Dey *et al*. (2005) which includes the effects of dislocation density and their arrangements within the microstructure. In case of low SFE materials, micro-strain broadening component strongly depend on the corresponding Bragg reflections (hkl), and Wilkens (1970) suggested that this dependency could be taken in account by the introducing the dislocation contrast factors in the SFE estimation relation.

The aforementioned discussions suggest that estimation of the microstructural parameters related to dislocation and planar faults are prerequisites for an accurate measurement of SFE. It is well established that in the presence of dislocation-induced strain broadening, the variation of strain field can be described by the Wilkens strain function, given as (Wilkens, 1970):

$$\langle \varepsilon_L^2 \rangle = \rho \bar{C}_{hkl} \pi \left(\frac{b}{2\pi}\right)^2 \ln\left(\frac{R_e}{L}\right) \qquad (4.1)$$

where, the symbols have their usual meaning, as described in § 2.2 . The quantitative values of the parameters can be directly determined from the graphical plots of modified Williamson-Hall equation and modified WA procedure, as described in § 2.2.4. In terms of microstructural parameters, the SFE of the specimen (γ) can be expressed as (Smallman & Westmacott, 1957; Dey *et al*., 2005):

$$\gamma_{eff} = \frac{K_{111}\omega_0 G a A^{-0.37}}{\sqrt{3}\pi P_{sf}} \left\{ \left(\frac{b}{2\pi}\right)^2 (\rho \bar{C}_{111} \pi)\, ln\left(\frac{R_e}{L}\right) \right\} \qquad (4.2)$$

where, G is the shear modulus of the considered specimen and $A = 3.43$ is a constant related to the anisotropy factor, which can be easily determined from the elastic constants of the crystal and determined according to Pierce *et al*. (2014). The parameter, $K_{111}\omega_0$, is proportionality constant with a value of 6.6 (Martin *et al*., 2016), and $\bar{C}_{111}$ is the average contrast factor of dislocations along (111) Bragg reflection of austenite. After inserting the quantitative values of all the microstructural parameter, the SFE can be easily determined from Eq. (4.2). However, it is important to be mentioned here that the SFE value estimated according to Eq. (4.2) essentially produces the effective SFE, not the ideal SFE of the material. The ideal SFE of a material defined as the energy cost to produce only an infinitely long SF in the microstructure, and in practical situation it is impossible to find such case. Therefore, the presence of any microstructural defects increases the estimated SFE than the actual of the material. The ideal and effective SFEs of a real crystal can be related using the following relation (Müllner & Ferreira, 1996):

$$\gamma_{eff} = \gamma_{\infty} + \frac{\partial E_{str}}{\partial A} \tag{4.3}$$

where, γ_{eff} and γ_{∞} are the effective and ideal SFEs, respectively. The effect of interaction of SF to any other defects presence in the microstructure is included in the term $\frac{\partial E_{str}}{\partial A}$, which basically indicate the amount of increment in elastic coherence strain energy per unit area of the SF. In this approach, it is assumes that the coherence strain energy is conserved with in a volume, while Olson & Cohen (1976) assumes it comprises of two components, the dilatation energy (E_{str}) due to volumetric strain associated with volume change during $\gamma \rightarrow \varepsilon_{hcp}$ martensitic transformation and the shear energy (E_{sh}) involving the shear strain components, and can be expressed as:

$$E_{str} = E_{dil} + E_{sh} \tag{4.4}$$

The studied deformation conditions considered in the present study do not reveal any significant $\gamma \rightarrow \varepsilon_{hcp}$ transformation, and therefore Olson & Cohen (1976) treatment is not tenable here, and thus Mullner & Ferreira (1996) approach was adapted to interpret the experimentally estimated SFE value.

4.1.2 Direct approach

By considering the isotropic elastic approach, Whelan (1958) first proposed a simplified analysis of SFE estimation form extended dislocation node for stainless steel, while the interaction of partial dislocations and the effect of dislocation's curvature were neglected. Later, many influencing factors have gradually been taken into account in several reappraisals of the theory. The interaction energy of partial dislocations were taken into account by Simes *et al.* (1961) and it was further modified by Brown *et al.* (1964), in which the effect of node character (edge/screw) on dislocation line tension was also included. The most compatible SFE values for an equilibrium shape of isolated symmetric extended nodes were numerically estimated by Brown and Thölen (1964), and the outcomes of this numerical analysis in terms of dislocation character angle (β'), outer radius (R_1), inscribed radius (R_2) and core radius (r_c) of partial dislocations can be summarized as:

$$\frac{\gamma_{eff} \times R_1}{G b_p^2} = 0.27 - 0.08 \left(\frac{\nu}{1-\nu}\right) cos2\beta' + \left\{0.104 \left(\frac{2-\nu}{1-\nu}\right) + 0.24 \left(\frac{\nu}{1-\nu}\right) cos2\beta'\right\} log_{10} \frac{R_1}{r_c} \quad (4.5)$$

$$\frac{\gamma_{eff} \times R_2}{G b_p^2} = 0.055 \left(\frac{2-\nu}{1-\nu}\right) - 0.06 \left(\frac{\nu}{1-\nu^2}\right) cos2\beta' + \left\{0.018 \left(\frac{2-\nu}{1-\nu}\right) + 0.036 \left(\frac{\nu}{1-\nu}\right) cos2\beta'\right\} log_{10} \frac{R_2}{r_c} \quad (4.6)$$

The parameter G and ν refers to the shear modulus and the Poisson's ratio of the material, respectively. The Burger's vector of the partial dislocation is indicated by $\vec{b}_p$. The schematic of a dislocation node in Fig. (4.1) clearly indicates both types of radii and the character angles at different points A, B and C.

As discussed previously the SFE can also be determined by measuring the dissociation width of a perfect dislocation at equilibrium configuration. It is well known that a perfect dislocation in fcc lattice can dissociate into two partial dislocations such as: $\frac{a}{2}[01\bar{1}] \rightarrow \frac{a}{6}[\bar{1}2\bar{1}] + \text{SF} + \frac{a}{6}[11\bar{2}]$. The newly created two partial dislocations repel each other and create a stacking fault region in between them. In this method,

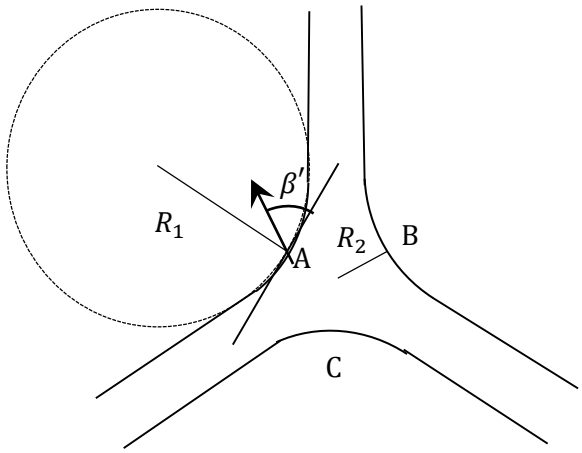

Fig. 4.1: Schematic representation of an extended three-fold dislocation node and the parameters related to Eqs. (4.5 & 4.6).

it is considered that the equilibrium is established between two partial dislocations only due to the fact that the attractive force originating from the increment of the SF area balances the repulsive elastic force acting between the two partials. Considering anisotropic dislocation theory, Hirth *et al*. (1982) suggest that the equilibrium separation distance of the partial dislocation pairs (x_{eq}) in nearly parallel segments of the perfect dislocations and their corresponding character angle (β') can be correlated to the SFE of the material through the following approximated relation:

$$\gamma_{eff} = \frac{Gb_p^2}{8\pi x_{eq}(1-\nu)}(2 - \nu - 2\nu\, cos\, 2\beta') \qquad (4.7)$$

Where the symbols in the Eq. (4.7) have their usual meaning, as describe earlier. The measured dissociation widths of several partial dislocation pairs can be easily plotted against their corresponding character angles according to the Eq. (4.7). Similarly, considering a particular SFE value one can get the variation of dissociation width for different character angle from the Eq. (4.7), and the SEF value can be easily estimated by the best-fitting of those two curves. Interestingly, there are many ways, which can actually produce a scatter in the estimated SEF values. Firstly, one has to measure the dissociation width from isolated straight dislocations that are not influenced by the presence of any other defects. Secondly, a special precaution should be taken while measuring the dissociation width using WBDF technique under TEM, as the WBDF micrograph of a dislocation does not corresponds to the actual position of its cores due to its strongly dependency nature on the specimen thickness and the excitation error.

Therefore, the measurement of partial dislocation separation from WBDF images required some corrections to get the actual dissociation width (William & Carter, 2009).

4.2 SFEs of the selected steels

As discussed in § 4.1, the various experimental methods related to the SFE estimation were adopted to get a quantitative idea of the SFE of the studied high-Mn steel at undeform condition, whereas the experimental SFE estimation of the medium-Mn steel is not possible due to the presence high precipitates density. Therefore, the SFE of the medium-Mn steel was estimated only by using a sub regular solution model (Dinsdale, 1991), and that predicts a SFE value of ~ 25 mJ/m^2. In this section, we will use different experimental techniques to estimate the SFE value of the high-Mn steel, and the estimated SFE values obtained from different methods were critically examined to identify their effectiveness for the studied high-Mn steel. As we know, the experimentally estimated SFE value don't represent the actual SFE of the materials due to its strong correlation with the other defects present in the microstructure, and therefore to minimize the influence of other defects on the SFE value of the studied steel, we estimated SFE value from the undeformed specimens of the present steel. This chapter is basically divided into three sections, namely; direct method, indirect method and combination of both, and which are discussed subsequently.

4.3 Direct method

The direct method of SFE assessment mainly involves the techniques of SFE estimation directly only by observing the stacking faulted regions under TEM investigations. There are mainly two well-known direct method, one of which deals with the dissociation width of a perfect dislocation, whereas, other deals with the radius of dislocation nodes. In general, the measurement of dissociation width is mostly used as compare to the node radius measurement due to the scarce appearance of isolated and symmetrical dislocation nodes in the microstructure. However, both the techniques are useful only for low to moderate SFE value materials, and as the SFE value increases the application of both the techniques restrict themselves due to deficiency of both the micrographs i.e., the extended dislocation node and dissociated perfect dislocation in the microstructure. Fortunately, we found both of them for the present steel and thus

we have estimated the SFE value of the studied steel using both techniques, which are described below.

4.3.1 Dissociation width measurement method

The dissociation widths of a few perfect $\frac{a}{2}[01\bar{1}]$ dislocations were measured near a [111] zone axis with a weak $g_{02\bar{2}}$ beam under $g-3g$ diffraction conditions. Inside–outside contrast techniques by reversing the g-vector were applied to distinguish partial dislocations from dipoles. To ensure that the measured dislocation dissociation widths are completely free from any influence of the microstructural defects and the equilibrium condition is produced only due to force balance between attraction of stacking fault and repulsion of partial dislocations, fully isolated parallel and almost straight partial dislocation pairs were strictly chosen for measurement setting far apart from any microstructural defects. During TEM observation we studied only those dislocations, which are at least 250 nm apart from each other and any other microstructural defects.

Fig. 4.2(a-b) shows a combination of two-beam BF images and their corresponding WBDF images of such isolated parallel partial dislocation pairs as representatives, which are obtained from the undeformed specimens. Interestingly, both partial dislocations are visible in the WBDF images of Fig. 4.2(a-b), which suggest that the Burgers vector of the perfect dislocation is nearly parallel to $[02\bar{2}]$ reflection, otherwise only one partial dislocation can be observed (Lu et al., 2016). However, detailed Burgers vector analyses were done by exciting different g vector in a systematic way to determine the exact Burgers vector of the perfect dislocation and therefore the total character angle of the dislocation line. At first, the Burgers vectors of the dislocations were by calculated from Burgers vector analysis by exciting different $\vec{g}$ vectors, and then angle between the dislocation line and the corresponding Burgers were measured using Digital Micrograph software. Considering [111]-zone axis and distinct g vectors, the Burgers vector analysis of the partial dislocations yields $|\vec{g}.\ \overrightarrow{b_p}| = \pm 1$ or 0, and both the partial dislocations have $|\vec{g}.\ \overrightarrow{b_p}| = \pm 1$ i.e., satisfying the visible criteria under TEM studies only at one g vector, $[02\bar{2}]$. The SAED pattern of the corresponding WBDF images captured under different $g-3g$ diffraction conditions are

also presented as inset in Fig. 4.2(a-b). The equilibrium separation distance of the partial dislocation pairs (x_{eq}) in nearly parallel segments of the $\frac{a}{2}[01\bar{1}]$ dislocations and their character angle (β') were then utilized to estimate the SFE of the steel via the isotropic approximation (Pierce et al., 2014; Mahato et al., 2015) of anisotropic dislocation theory according to the Eq. (4.7).

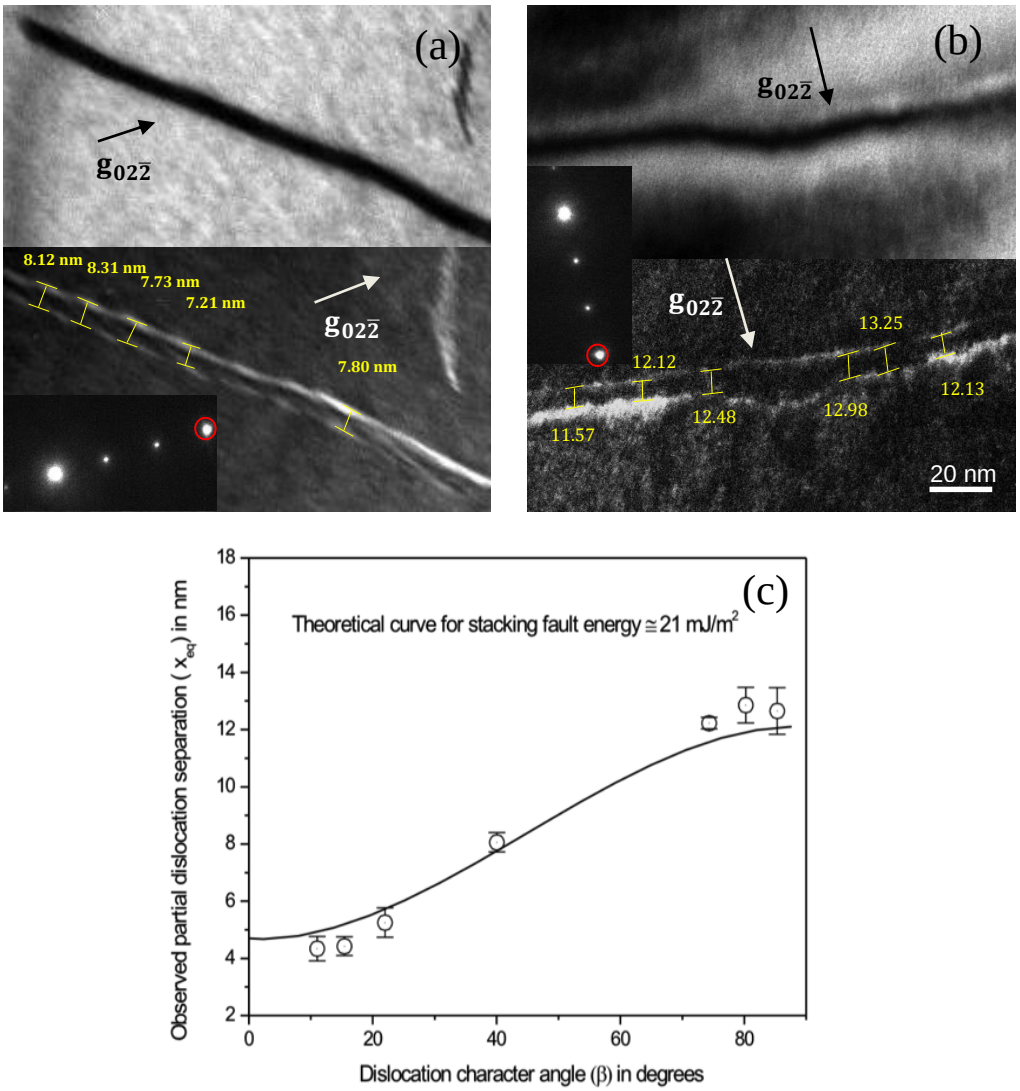

Fig. 4.2: Representative extension widths of $\frac{a}{2}[01\bar{1}]$ dislocations in the steel measured using weak $g_{02\bar{2}}$ beam under WBDF for: (a) nearly screw type dislocation, (b) nearly edge type dislocation; the corresponding two-beam BF images are also presented in the upper half, (c) the fitting of observed extension widths according to Eq. (1) yielding SFE of the steel ~ 21 mJ/m^2.

Assuming the shear modulus of the steel G ≈ 65 GPa (Karjalainen et al., 2012), the Poisson's ratio ν = 0.24 (Pierce et al., 2014) and considering $b_p = \left|\frac{a}{6}\langle 112\rangle\right|$,

the average separation distances, x_{eq}, for several $\frac{a}{2}[01\bar{1}]$ dislocations having different character angle were estimated. The variation of measured x_{eq} is plotted against β' in Fig. 4.2(c) and then they are fitted according to Eq. (4.7) using SFE value as a fitting parameter and that also plotted in Fig. 4.2(c). It is clear from Fig. 4.2(c) that the measured separation distances matched well ($R^2 = 0.98$) with character angles for a SFE value $\sim 21 \pm 3$ mJ/m^2, and interestingly it is also close to the SFE value as predicted by subregular solution based thermodynamic model of the steel (Saeed–Akbari et al., 2009). However, a low SFE value as estimated by measuring the separation between parallel partial dislocations using WBDF technique suggest that SFE can also be measured using extended dislocation node method for this alloy, whereas the HRTEM techniques is the only way for alloys having very high SFE (Balk et al., 2001). Therefore, the determination of SFE using HRTEM technique is excluded to minimize the surface influence on SFE of these types of very low SFE alloys, and to substantiate the findings of this partial dislocation separation method another TEM method named as extended dislocation node is used, and which is discussed subsequently.

4.3.2 Extended dislocation node method

Mostly, dislocation nodes are formed due to interaction of two extended dislocations on identical slip plane, or by interactions on intersecting planes i.e. cross slip of the dislocation into the slip plane of the other dislocation (Whelan et al., 1958). Only considering the isotropic elastic approach, Whelan (Whelan et al., 1958) first give a simplified analysis to determine the SFE form extended dislocation node for stainless steel, while the interaction of partial dislocations and the effect of dislocation's curvature were neglected. However, many other influencing factors have gradually been taken into account in several reappraisals of the theory as discussed in § 4.1. In this study, the SFE values were also estimated according to Eqs. 4.5 & 4.6 by measuring the inscribed and outer radius of dislocation nodes, and the estimated SFE value is compatible only for an isolated symmetric extended node although they are rarely observed under TEM investigations. Therefore, finding some isolated symmetric extended node is a big challenge for this technique, as most of the nodes are often entangled with dislocations.

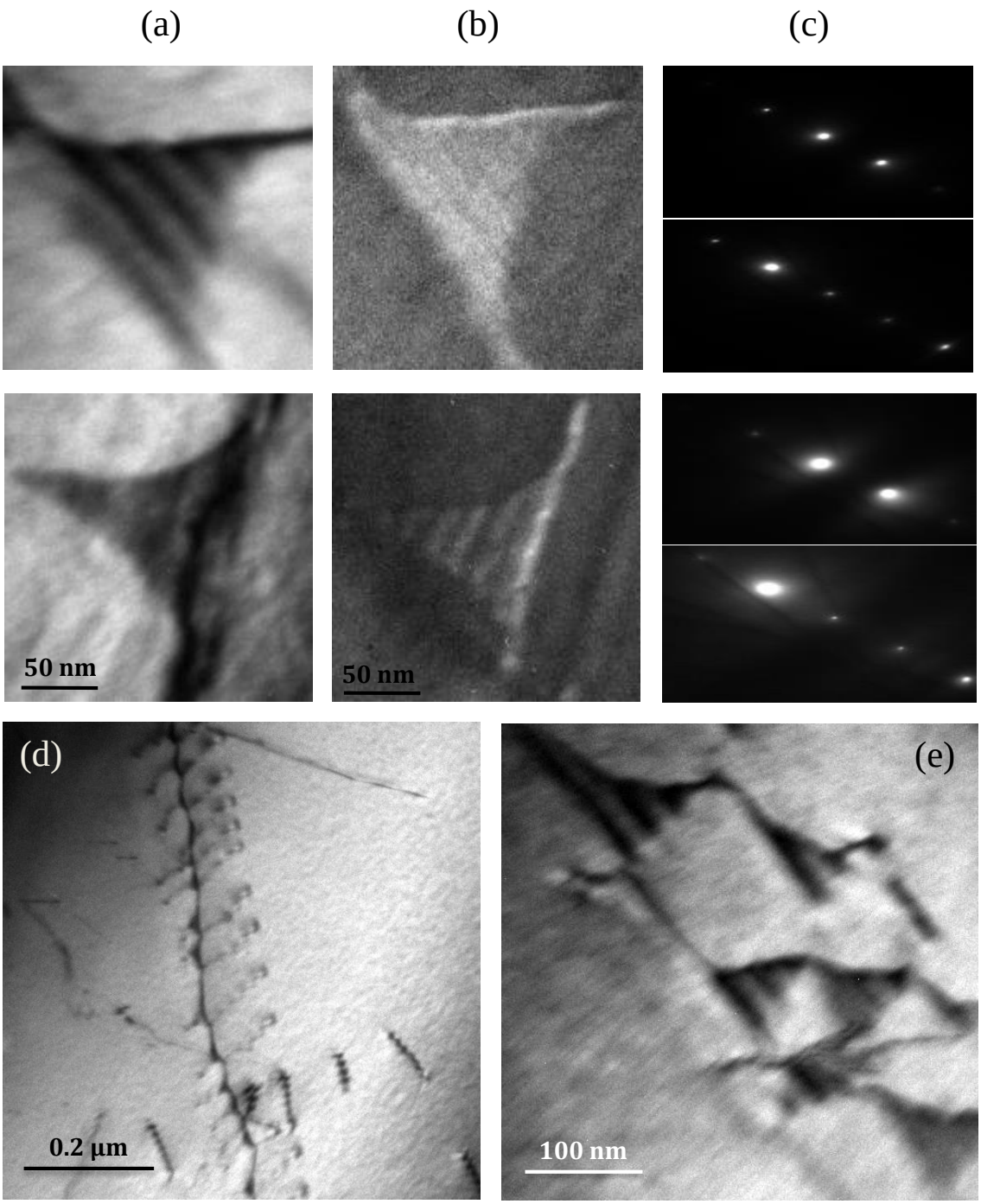

Fig. 4.3: Representative asymmetric dislocation nodes and inter-connected nodes observed under different diffraction conditions: (a) Two-beam BF image. (b) WBDF image of the same two- beam BF image. (c) Diffraction conditions correspond to the TEM micrograph (a) and (b) are presented in the upper and lower half, respectively. Micrograph in (d) & (e) represents array of inter-connected nodes under low and high magnification, respectively.

In general, the extended nodes are formed in arrays and they are found asymmetric in nature. Fortunately, in addition to extended dislocation arrays a few isolated dislocation nodes were also observed for the present steel under TEM

investigations, although they were scarce in most of the regions of this undeformed microstructures. The TEM micrographs of asymmetric nodes as well as arrays of dislocation nodes are presented in Fig. 4.3 obtained from undeform specimens. The two-beam as well as its WBDF micrographs of the asymmetric nodes are presented in Fig. 4.3 (a) & 4.2(b), respectively, whereas their corresponding diffraction conditions are presented in the upper half and the lower half of the Fig. 4.3(c). The difficulties to fit the outer radius, R_1, for any asymmetric node could be directly comprehensible from Fig. 4.3(a) & 4.3(b), however the inscribed radius, R_2, can be measured in a convenient way. The influence of occurrence of an array of closely placed dislocation nodes in Fig 4.3(d) clearly indicate towards an interesting fact that the interaction with the neighbouring node create an asymmetric line tension in the different node's arms, and that produce an asymmetric shape of dislocation node at its equilibrium conditions, which can also be observed more clearly from the high-magnification TEM micrograph presented in Fig. 4.3(e). In this study, we have selected only those dislocation nodes for the SFE measurement which are isolated, approximately symmetric in nature and also it is reasonably far away from the foil surface to minimize the surface influence as it creates anomalous curvature on dislocations by decreasing the dislocation line tension of the extended dislocation node. These conditions were deliberately chosen as being suitable for the SFE estimation model given by Brown and Thölen (Brown & Thölen, 1964).

Fig. 4.4 shows a set of isolated as well as approximately symmetric dislocation nodes, which are used for SFE measurement in this study. The two-beam BF micrographs of extended dislocation nodes are presented in Fig. 4.4(a), whereas the WBDF micrographs and the corresponding diffraction conditions are presented in Fig. 4.4(b) & 4.4(c), respectively. In general, screw characters of extended nodes are expected to produce more in the microstructures due to its slightly lower energy value as compared to an edge character node, and therefore it has also little large in size as compared to the edge character nodes (Brown, 1964). Interestingly, most of the nodes that are observed in the microstructure were predominantly tend towards screw character, and that can also be observed from the TEM micrographs presented in Fig. 4.3 & 4.4. Furthermore, only screw-orientated nodes were chosen for SFE measurement due to the fact that the Brown and Thölen model provides more precise SFE value only for screw character nodes (Brown & Thölen, 1964), whereas, the validation of this

model is quite challenging for an edge character node (Ruff, 1970). Incorporating the value of G ≈ 65 GPa (Karjalainen et al., 2012), the Poisson's ratio ν = 0.24 (Pierce et al., 2014) and assuming $\varepsilon \approx b_p$(Brown & Thölen, 1964) in the Eqs. (4.5) & (4.6) the SFE values are estimated for each nodes having different character angles, and the average value of such measurements yields a SFE value of $\sim 21 \pm 3$ mJ/m^2, which is almost similar to the estimated SFE value in § 4.3.1. To understand the reliability of the SFE values as determined using different TEM techniques, we will compare it with the SFE value estimated from the indirect method, and which is now described in § 4.4.

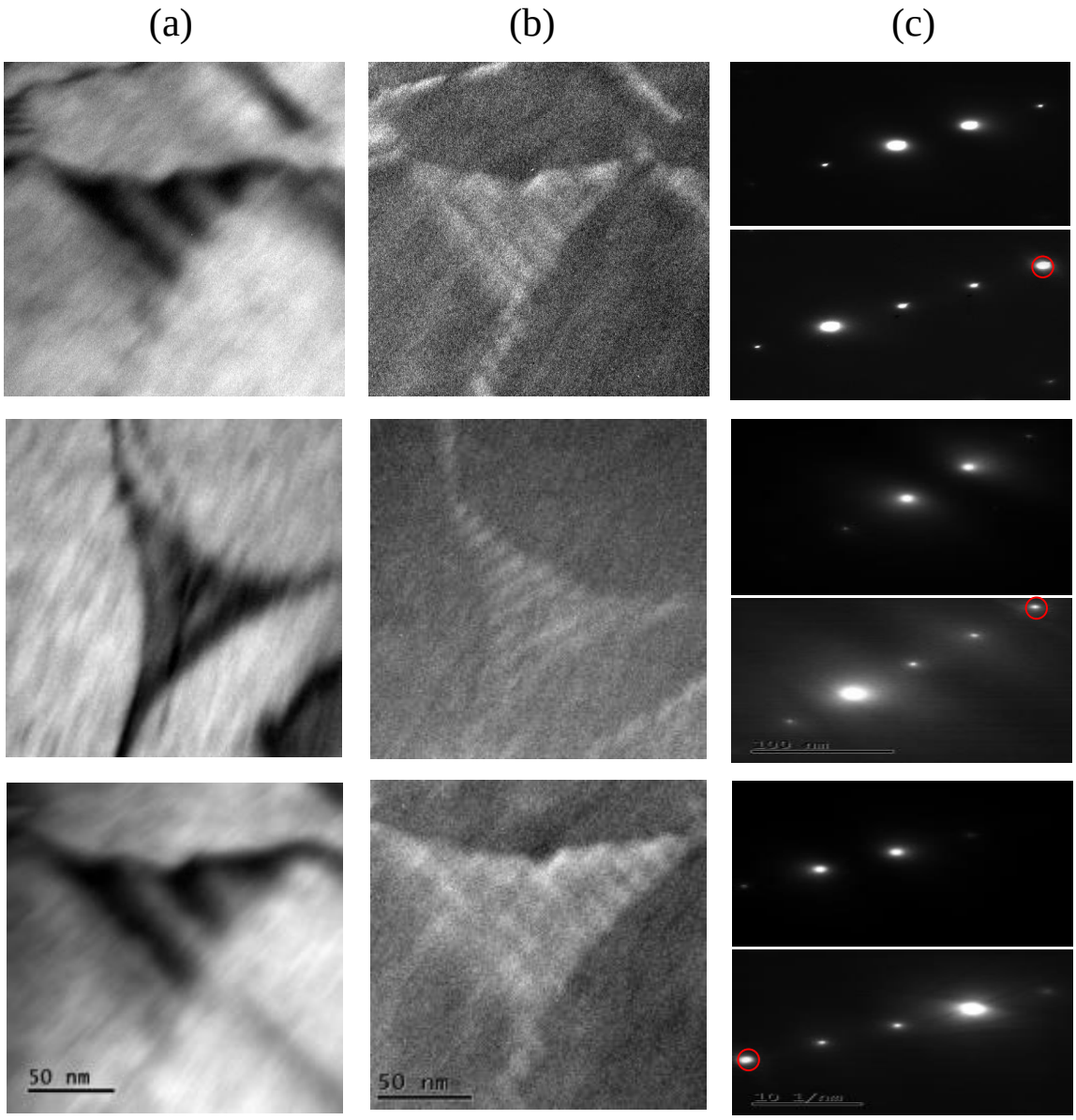

Fig. 4.4: Representative symmetric dislocation nodes used for SFE estimation observed under different diffraction conditions: (a) two-beam BF image, (b) WBDF image of the same two- beam BF image. (c) Diffraction conditions correspond to the TEM micrographs (a) and (b) are presented in the upper and lower half, respectively.

4.4 Indirect method

The indirect method of SFE estimation is basically gives the SFE value of the materials using the correlations between the different microstructural parameters related to the microstructures, which can be easily obtained from the XLPA of the XRD pattern. It is well known that Schramm and Reed (Schramm & Reed, 1975) first proposed a simple SFE estimation model in terms of different microstructural parameters for austenitic steel, and later it was modified significantly by several researchers to account the influence of different interaction among the microstructural parameters, as discussed in § 4.1.1. In this study the SFE of the present steel was estimated from Eq. (4.2) by inserting the related microstructural parameters such as: dislocation density, outer cut-off radius, average contrast factor, stacking fault probability and the Fourier variable were obtained from the XLPA as described in Chapter 2.

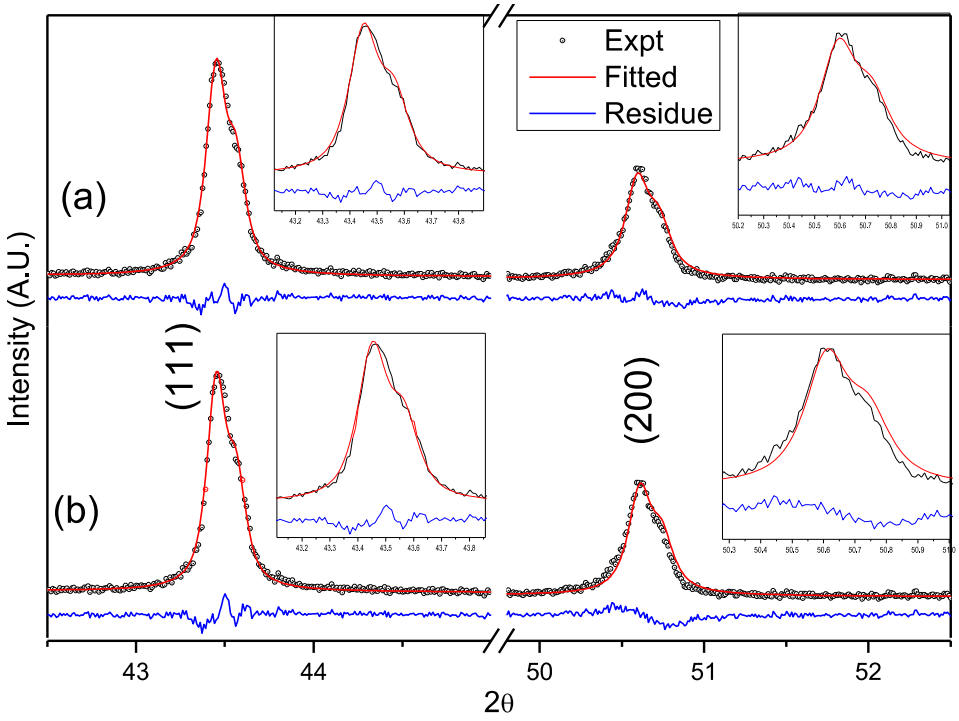

Fig. 4.5: Effect of SFs on the quality of Rietveld refinement in the XRD pattern for the relevant range of the present steel showing: (a) fitting considering with SFs, (b) fitting considering without SFs. The residue curves are plotted in the same scale at the bottom of the XRD patterns.

Important aspects of the Eq. (4.2) suggest that the dependency of SFE on P_{sf} value is very sensitive as compare to the other microstructural parameters, any small change in P_{sf} value produce a significant scatter in the estimated SFE value. However, the dislocation density of high-Mn austenitic steels at annealed conditions generally approximated as $\sim 10^{14}$ m^{-2}, and that increases by an order at highly deformed condition i.e. at fracture strain (Mahato et al., 2015; Das et al., 2021). Therefore, it is to be mentioned here that the determination of P_{sf} is most important and challenging task to estimate a precise SFE value from Eq. (4.2), and depending on the experimental conditions and other limitations there are different methods of P_{sf} value estimation as discussed in Chapter 2. Due to absence of any long-range residual stress in the microstructure, and the absence of deformed specimens we use the Wagner peak shift approximation (Wagner, 1966), and the P_{sf} value of the present steel were estimated according to Eq. (2.25) (Chapter 2). Relatively low P_{sf} value was obtained as compared to the other high-Mn steels under deformed conditions, and to verify the obtained P_{sf} value we have also fitted the full XRD pattern of the studied steel according to Rietveld refinement (Rietveld et al., 1969) process using Material Analysis Using Diffraction (MAUD) program and interestingly the order of the obtained P_{sf} value matched well with the previously estimated value. The fitted XRD pattern for the relevant range is also presented in Fig.4.5, and which clearly indicates that SF is present in the studied steel, although the concentration of SF is very low in the microstructure. To detect such small amount of peak shift and understand the

Table 4.1: Microstructural parameters obtained from X-ray line profile analysis.

Lattice parameter, a (Å) ±(0.0003-0.0006)	Contrast factor, C_{111} ± (0.01-0.02)	Dislocation character parameter, q	Dislocation density, ρ ($\times 10^{14}$ m^{-2}) ± (0.12-3.95)	Outer cut-off radius of dislocation, R_e (nm) ± (2-4)	Stacking fault probability, ($P_{sf} \times 10^{-4}$) ±(0.00001 - 0.0004)	SFE, γ (mJ/m^2) ± (3.5)
3.6061	0.0822	2.1	2.13	116	4.1	16

quality of refinement, the respective Bragg peaks were magnified and also plotted as inset in the Fig. 4.5. It is clearly observed from Fig. 4.5(a-b) that the quality of refinement significantly improved as we include Warren's planar fault model during the refinement process in MAUD program. The estimated SFE value and the related microstructural parameters obtained form XLPA analysis of the studied steel are also listed in Table 4.1.

4.5 A combination of direct & indirect method

In this section we will discuss a different approach that combine both, the indirect (XRD) and direct (TEM) observation to estimate the SFE of the present steel. Although this method is based on certain oversimplified postulates in which the influence of any types of interactions were neglected, but it can give an idea of the SFE of the material. However, this method was not recommended for the specimens in which the dislocation are strongly correlated i.e. the dislocation interactions is significant in the microstructures, and these situations mostly occurs at deformed conditions. In this case, as we studied the undeform specimen and therefore a significantly low probability of dislocation interactions were expected, thus it is expected that the estimation of SFE using this method can also produce a realistic SFE value for the studied steel. According to this method, the SFE of the studied steel be determined from the following relation expressed in terms of dislocation density (ρ), SF probability (P_{sf}) and inter planar spacing along [111] crystallographic direction (d_{111}) as (Smallman et al., 1957; Noskova et al., 1962):

$$\gamma_{eff} = \frac{Ga^2}{24\pi}\left(\frac{d_{111}\rho}{P_{sf}}\right) \qquad (4.8)$$

The values of the microstructural parameters such as: a, d_{111} and ρ were already obtained from the indirect method like XLPA and also listed in Table 4.1, whereas the most significant parameter in the Eq. (4.8) i.e. P_{sf} is determined in a different way using direct observation method like TEM. The SF probability of a materials basically express the fraction of slip planes which are faulted, and if we consider the SF as a band that lies between two partial dislocations then the SF probability can be represented as (Seeger, 1957; Vassamillet, 1961):

$$P_{sf} = \kappa.\rho.d \qquad (4.9)$$

where ρ and d represents the dislocation density and the inter-planar distance of the faulted crystal planes, respectively, whereas the width of SF band the is denoted by the parameter κ. In general, the value of $\rho \sim 10^{14}$ m^{-2} for annealed high-Mn austenitic steels (Mahato et al., 2015; Das et al., 2021) and that can also be observed from the output of XLPA presented in Table 4.1 for the studied steel. Therefore, the determination of P_{sf} using Eq. (4.9) essentially depends on the width of the SF bands, and the average width of the SF band was measured from the TEM micrographs, as discussed subsequently.

An important aspect related to the SF width measurement from the TEM microstructures is that the measured SF must be far away from any other defects which can modify the width of the SF. In this study we have considered only those SF bands, which are at least 200 nm apart from each other and any other microstructural defects presence in the microstructure. Several SF width measurements were carried out from different TEM micrographs, and the average SF width for the studied steel was obtained. Few multi-beam TEM microstructures comprising only SF bands obtained along [110]-zone axis are presented in Fig. 3.5 as a representative. A careful observation of the low magnification TEM microstructure in Fig. 4.6(a) & (b) also confirms that we have restrict the width measurement to only those SF bands which are not strongly interacting with any other defects, and the width of the measured SF bands are also delineated with double-headed arrow lines in red. However, a high magnification TEM micrograph of SF bands in Fig. 4.6(c) clearly reveals that the SF bands are closely packed, and some of them also predominantly interact with dislocations. As a consequence of these interactions, the width of the SF bands gets modified and which could be easily understood in terms of frequent occurrences of tiny and overlapping SFs in the microstructure presented in Fig. 4.6(c). The diffraction conditions at which the TEM micrographs are obtained is presented in Fig. 4.6(d), which clearly indicate that all the SF bands are extended along [111] or [200], eventually which are two most prominent crystallographic directions for austenitic steels.

The measured average width of the SF bands $\sim 4.6\ \mu m$ is inserted in Eq. (4.9), and that yields a SF probability value of ~ 0.0967, which is significantly higher as compared to the P_{sf} value obtained from XLPA (Table 4.1). The discrepancy in the

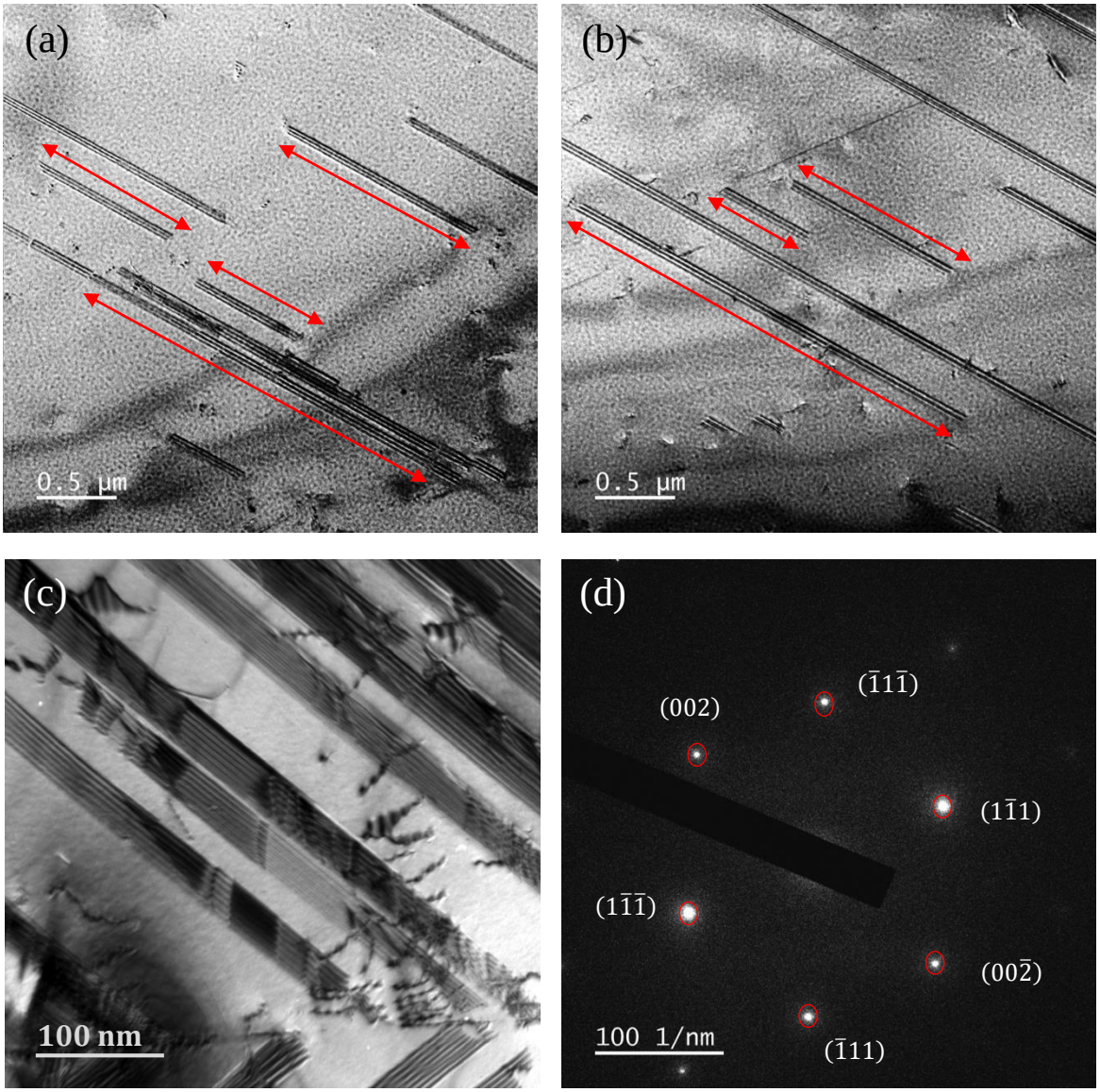

Fig. 4.6: TEM BF micrographs of the present steel under multi-beam diffraction condition showing: (a,b) SFs at low magnification, (c) SFs at high magnification, (d) corresponding diffraction condition. SF band widths are delineated with double-headed red arrow lines.

P_{sf} value obtained from XRD and Eq. (4.9) could be understood in terms of the fundamental postulates of XLPA that the SFs are uniformly distributed throughout the whole microstructures, but in reality, it is not true and the SFs density significantly varies for different regions of the specimen i.e., the SFs density is a localized quantity. As a result of which, the SF probability value obtained from TEM micrographs using SFs width measurement is much higher than the P_{sf} value obtained from the XRD measurement. Interestingly, a SF probability value close to 1, i.e. $P_{sf} \rightarrow 1$, signifies that the fcc structure is mostly transformed into $\varepsilon -$ martensite and the microstructure is

fully comprised of SFs (Wang et al., 2007), but no signature of $\varepsilon-$ martensite was found during XRD measurement and that can also be confirmed from the selected XRD pattern presented in Fig. 4.5, and therefore, the P_{sf} value obtained using Eq. (4.9) needs to be modified.

Table 4.2: Comparison of the experimentally measured SFE value of Fe-Mn-Al-C alloys.

Composition of alloy in wt%	Dissociation width of partial dislocation (mJ/m^2)	Extended dislocation node (mJ/m^2)	XRD (mJ/m^2)	Combination of TEM & XRD (mJ/m^2)	Thermodynamic model (mJ/m^2)
Fe–16.4Mn–1.54Al–0.29C	(21±3)*	(19±2)*	(16±3.5)*	(24±3)*	21*
Fe-18Mn-0Al-0.6C	13±3 (Kim et al. 2011)	-	17±3 (Jin et al. 2012)	-	16.6 (Zambrano, 2016)
Fe-18Mn-1.5Al-0.6C	-	-	25 (Jeong et al. 2012)	-	-
Fe- 16Mn-1.5Al-0.3C	-	-	21 (Shyamal et al. 2021)	-	19 (Hamada et al. 2009)

*Indicate measured in this work

Wang et al. (2007) first observed a similar kind of deviation in the P_{sf} value while estimating the SF probability from XRD and electron diffraction method while estimating the SFE of Fe-Mn-Si-Al TWIP steels. Later, Bae et al. (2022) was also observed the same while studying Fe-Mn-C steel, and they suggested a multiplication factor of $\sim 10^{-3}$ to the SF probability estimated using electron diffraction to get a practical SFE value that matched well with the theoretical SFE value of the studied steel obtained using supercell (Dong et al., 2019) and thermodynamic method (Lee et al., 2000). By inserting the P_{sf} value ~ 0.0967 in the Eq. (4.8) one can estimate the SFE value of $\sim 2.44 \times 10^{-2}$ mJ/m^2, nearly close to zero, which advocates towards the fact that most of the perfect dislocations are dissociated to partials and there is no difference in energy between austenite and any other phase, and this is not true in reality. However, considering the multiplication factor $\sim 10^{-3}$ in the P_{sf} value, as suggested by Bae. et.

al (2022), the estimated SFE value from Eq. (4.8) is ~ 24.4 mJ/m^2, and which match fairly well with the SFE values as determined by the other methods as discussed previously (§4.3-4.4).

To understand the efficiency of different methods for the studied steel the measured SFE values are listed in Table 4.2, and the previously reported experimentally determined SFE values of the similar types of steels are also purposefully included in Table 4.2 for comparison. It is clearly observed from Table 4.2 that the previous researchers has applied only one method, mostly XRD, to estimate the SFE of the studied steels, whereas we have used different existing experimental techniques and interestingly the outcomes agree considerably well to each other. The SFE is also calculated using thermodynamic model comprising the effect of grain size, temperature and compositions as described by Zambrano (2016) for Fe-Mn-Al-C-Si steels. Invoking the grain size ($\sim 25\,\mu m$) and temperature (RT) in the thermodynamic model (Zambrano, 2016) we obtain a SFE value of ~ 25 mJ/m^2 for the present steel, and that matched well with the experimental SFE values only for an interfacial energy value of ~ 10 mJ/m^2 (Zambrano, 2016), which is generally considered as a fitting parameter.

References

Bae, H.J., Ko, K.K., Ishtiaq, M., Kim, J.G., Sung, H., Seol, J.B. (2022) *J. Mat. Sci. & Tech.* **115**, 177-188.

Balk T. J. & Hemker K. J. (2001) *Philosophical Magazine A* **81(6)**, 1507-1531.

Brown, L.M. (1964) *Phil. Mag.* **10(105)**, 441-466.

Brown, L. M. & Thölen, A. R. (1964) *Disc. Faraday Soc*. **38**, 35-41.

Cockayne, D.J.H., Jenkins, M. L., Ray, I. L. F. (1971) *Philo. Mag.* **24: 192**, 1383-1392.

Das, S.R., Shyamal, S., Shee, S.K., Kömi, J.I., Sahu, P. (2021) *Mater. Charact.* **172**, 110833.

Dey, S. N., Chatterjee, P. & Sen Gupta, S. P. (2005) *Acta. Mater*. **53**, 4635-4642.

Dinsdale, A.T., (1991) *Calphad* **15**, 317–425.

Dong, Z., Schönecker, S., Chen, D., Li, W., Lu, S., Vitos, L. (2019) *Int. J. Plast.* **119**, 123–139.

Hamada, A. S., Karjalainen, L. P., Puustinen, J. (2009) *Mater. Sci. Eng. A* **517**, 68–77.

Hirth, J. P. & Lothe, J. (1982). *Theory of Dislocations*, Wiley, New York.

Jeong, J. S., Woo, W., Oh, K. H., Kwon, S. K., Koo, Y. M. (2012) *Acta Mater*. **60(5)**, 2290–2299.

Jin, J.-E. & Lee, Y.-K. (2012) *Acta Mater.* **60**, 1680-1688.

Karjalainen, L.P., Hamada, A. et al. (2012) *Scr. Mater.* **66**, 1034-1039.

Kim, J., Lee, S. J., De Cooman, B. C. (2011) *Scr. Mater*. **65(4)**, 363–366.

Lee, Y. -K., Choi, C. (2000) *Metall. Mater. Trans. A* **31**, 355–360.

Lu, J., Hultman, L., Holmström, E., Antonsson, K. H., Grehk, M., Li, W., Vitos, L., Golpayegani, A. (2016) *Acta Mater.* **111**, 39-46.
Mahato, B., Shee, S.K., Sahu, T., Ghosh Chowdhury, S., Sahu, P, Porter, D.A., Karjalainen, L.P. (2015) *Acta Mater*. **86**, 69–79.
Martin, S., Wolf, S., Martin, U., Krüger, L. & Rafaja, D. (2016) *Metal. Mater. Trans*. A. **47**, 49-58.
Müllner, P. & Ferreira, P.J. (1996) *Philos. Mag. Lett.* **73**, 289-297.
Noskova, N.I., Pavlov, V.A. (1962) *Phys. Met. Metallogr*. **14**, 87-92.
Olson, G.B. & Cohen, M. (1976) *Metall. Trans. A.* **78**, 1897-1923.
Pierce, D.T., Jimenez, J.A., Bentley, V., Raabe, D., Oskay, C. & Witting, J.E. (2014) *Acta Mater*. **68**, 238-253.
Rietveld, H. M. (1969) *J. Appl Cryst*. **2**, 65-71.
Ruff, A.W. (1970) *Metall. Mater. Trans. B* **1**, 2391–2413.
Saeed–Akbari, A., Imlau, J., Prahl, U., Bleck, W. (2009) *Metall. Mater. Trans. A* **40**, 3076-3090.
Schramm, R.E. & Reed, R.P. (1975) *Metall. Trans. A* **6**, 1345-1351.
Seeger, A. *Dislocations and Mechanical Properties of Crystals* (John Wiley & Sons, Inc., New York, 1957).
Shyamal, S., Das, S. R. et al., (2021) *Mater. Lett*. **285**, 129002
Simes, R., Delavignette, P. & Amelinckx, S. (1961) *Z. Physik*, **165**, 502-532.
Smallman, R.E., Westmacott, K.H. (1957) *Philos. Mag.* **2**, 669–683.
Vassamillet, L.F. (1961) *J. Appl. Phys.* **32**, 778–782.
Wagner, C. N. J. Local Atomic Arrangements studied by X--ray Diffraction (AIME, NewYork, 1966), Vol. 36, Chap.7.
Wang, X.D., Huang, B.X., and Rong, Y.H (2007) *J. Appl. Phys.* **101**, 093511.
Whelan, M.J. (1958) *Proc. R. Soc. Lond. A* **249**, 114-137.
Wilkens, M. in: J.A. Simmons, R. de Wit, R. Bulloug (Eds.), (1970) Fundamental Aspects of Dislocation Theory Vol. II, Natl Bur. Stand. Publ., Washington, 1195-1221.
William, D.B. & Carter, C.B. (2009) *Transmission Electron Microscopy*, second ed., Springer Science, NY, Vol-3.
Zambrano, O. A. (2016) *J. Eng. Mater. Technol*. **138(4)**, 041010.

Part C

Interpretation of Deformation Microstructure

Chapter 5*

Cyclic deformation microstructure of the high-Mn steel

*This chapter is published in Materials Letters, 285 (2021) 129002 & 327 (2022) 133006. (No. 2 & 3 in the list of publications)

5.1 X-ray line profile analysis (XLPA) of the deformation microstructure

It is well accepted to the material characterization community that the microstructural parameters, such as: lattice parameter, crystallite size, dislocation character, dislocation density, dislocation arrangement parameter, faulting propensity, SFE etc., are strongly correlated to the deformation behaviour of a material. Therefore, a detailed understanding of deformation behaviour of a material demands a precise quantitative estimation of the above-mentioned microstructural parameters for the deformed specimens, and that can only be achieved with considerable accuracy from X-ray line profile analysis (XLPA). In this chapter, the microstructural parameters related to the differently deformed specimens are evaluated according to XLPA as described in Chapter 2.2, and also their quantitative values are reported in the following sections.

5.1.1 Williamson-Hall plots and strain anisotropy

It is well known that the existence of any dislocation induced strain broadening in the deformation microstructure generally produces anisotropic strain broadening, and that can be confirmed through the manifestation of scatter in conventional W-H plot. For each differently deformed specimen, the conventional W-H plot was obtained by invoking the FWHMs of each Bragg reflections as a function of the diffraction vector (K), and the obtained plot for the graded grain and CG specimens are presented in Fig 5.1(a) & 5.1(c), respectively. Interestingly, both the plot shows a significant scatter, and which indeed confirms that the deformation microstructures are comprises of dislocation induced anisotropic strain broadening. Therefore, we obtain the modified W-H plots according to Eq. (2.16) (Chapter 2.2.4) in the analysis to assess the dislocation strain broadening contribution by introducing the concept of dislocation contrast factor as described in Ungar approach (Ungar et al., 1998). The corresponding modified W-H plots of the conventional W-H plots i.e. Fig. 5.1(a) & (c)) are presented in Fig. 5.1 (b) & (d), respectively.

As described in Chapter 2, the average contrast factor for different Bragg reflections were determined according to the Eq. (2.18) and the parameter q was determined from the the X-intercept of the linear fit of $[(\Delta K^2) - \alpha]/K^2$ vs. H^2plot according to the Eq. (2.20). The dislocation character parameter assessment plots

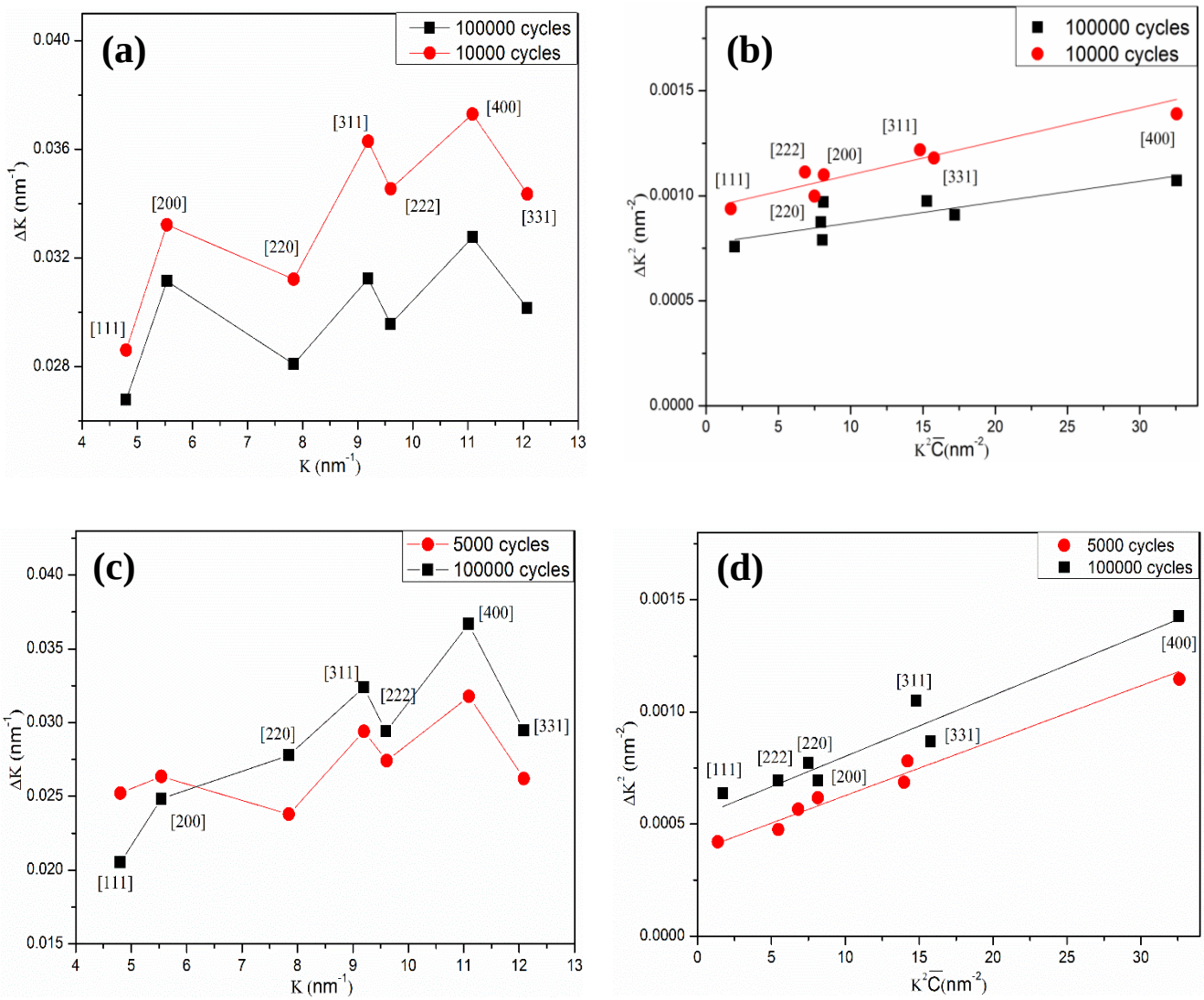

Fig. 5.1: The *conventional* Williamson-Hall plot for the graded grain (a) and CG specimen (c). The *modified* Williamson-Hall plot of (a) and (c) are presented in (b) and (d), respectively.

related to the differently cycled graded grain and CG specimens were presented in Fig. 5.2 (a) & (b), respectively. It is clearly observed from the modified W-H plots that the amount of scatter are significantly reduced as compared to the conventional W-H plots, and which advocates towards the fact that the application of Ungar approach (Ungar et al., 1998) can produce relatively reasonable value of the microstructural parameters associated to the deformation microstructure. A careful observation of modified W-H plots also indicates that in case of graded grain specimen ΔK^2 is higher in saturation stage as compared to the pre-saturation stage, whereas it is reverse in case of CG specimen. It is well known that the XRD peak profiles are fitted well with pV function,

which is basically a combination of Lorentzian and Gaussian distribution functions and the Lorentzian component is generally related to the crystallite size broadening, whereas Gaussian component is responsible for any strain broadening (Warren et al., 1952; Ungar et al., 1989). Therefore, to understand the effect of deformation actual behavior we need to first evaluate the microstructural parameters generated from the strain broadening, and which can not be done accurately from modified W-H plot, thus Warren-Averbach analysis were adopted in this study.

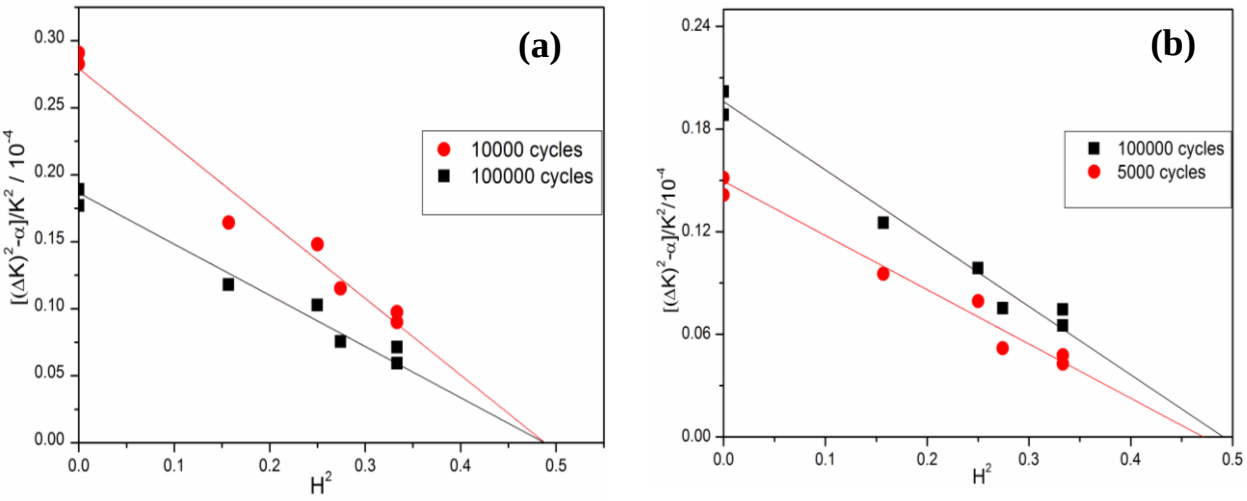

Fig. 5.2: Linear fitting to the variation of $[(\Delta K^2) - \alpha]/K^2$ with H^2 according to Eq. (6) for (a) graded grain (b) CG specimen.

5.1.2 Conventional and modified Warren-Averbach analysis

The Bragg reflections of the deformed specimens were fitted using pseudo-Voigt (pV) function according to Enzo et al. (1988), and the Fourier transformation of the fitted data is used to get the real part of the Fourier coefficients, $A(L)$ for different Fourier lengths, (L). It is important to mention here that here we obtain the Fourier coefficients only considering the Gaussian component related to the corresponding Bragg reflections. The obtained Fourier coefficients were then plotted against the square of the diffraction vector, K^2, to obtain the conventional W-A plots for each deformed specimen. As a representative, the conventional W-A plots for the graded grain and CG specimen deformed to saturation stage are presented in Fig. 5.3(a) and Fig. 5.3(c), respectively. Interestingly, $ln\,A(L)$s for different L in the conventional W-A plots demonstrate a similar kind of scatter points that were previously observed in

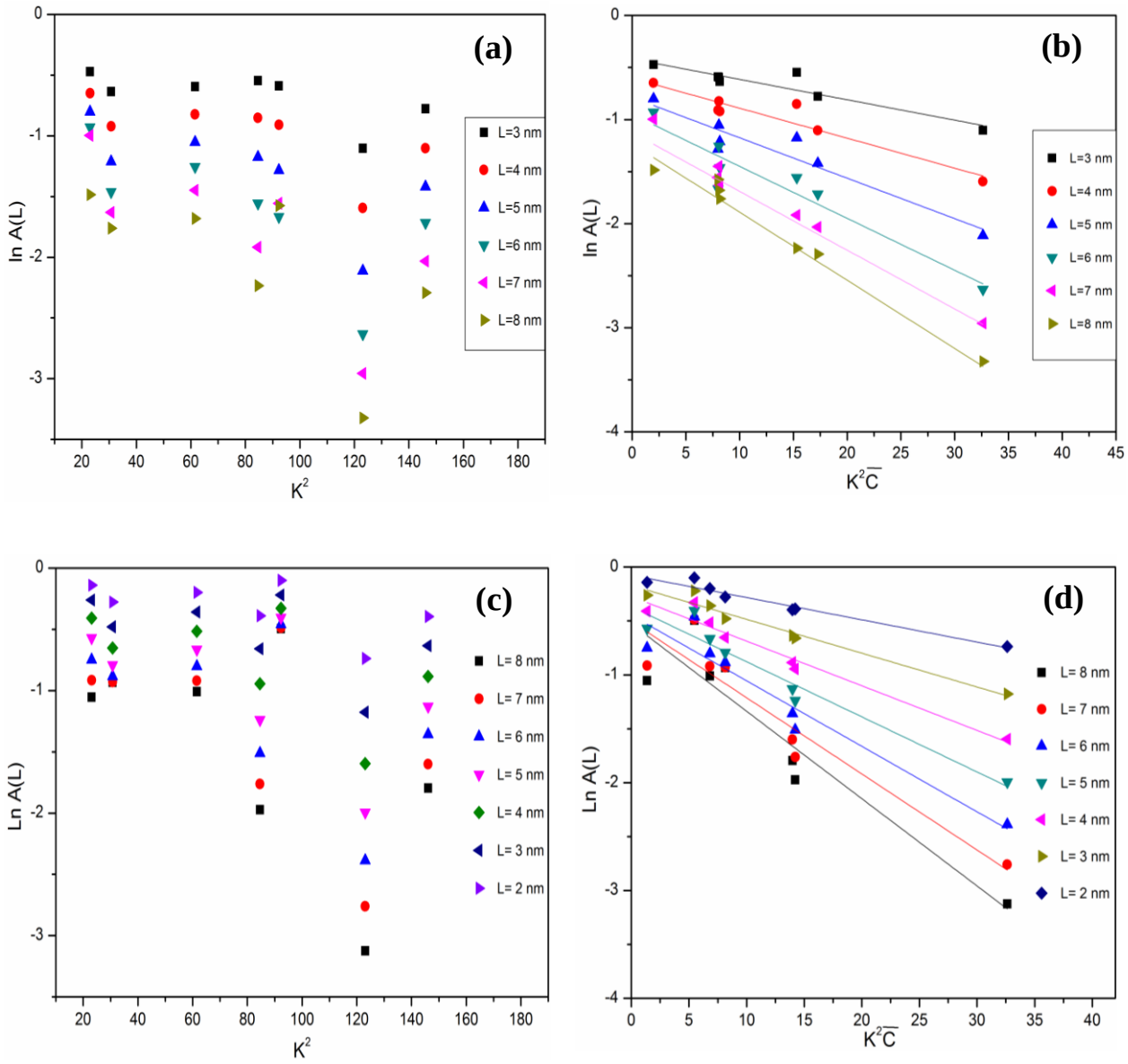

Fig. 5.3: Variation of logarithmic Fourier coefficient, $ln\,A(L)$, of the specimens deformed to saturation stage at different L values according to *conventional* Warren-Averbach plot for the graded grain (a) and CG specimen (c). The *modified* Warren-Averbach plot of (a) and (c) are presented in (b) and (d), respectively.

the conventional W-H plots in §5.1.1. Therefore, again we invoke the concept of dislocation contrast factor to assess the dislocation strain broadening component, and further use it to obtain the modified W-A plots according to Eq. (2.23) (Chapter 2). The corresponding modified W-A plot of the conventional W-A plots i.e. Fig. 5.3 (a) & (c) are presented in Fig. 5.3 (b) & (d), respectively. The W-A plots in Fig. 5.3 clearly demonstrate that the amount of scatter is significantly reduced, and comparatively smoother curves were obtained after invoking the concept of dislocation contrast factor.

A critical observation of the modified W-A plots also suggest that the scatter amount is larger for higher L value as compared to the lower L value, although a linear relationship between $ln\,A(L)$ and $K^2\bar{C}$ is almost maintained for all L values in the range of 2-8 nm. Therefore, the slopes of the liner fitted $ln\,A(L)$ and $K^2\bar{C}$ plots would consistently determine $\rho\frac{\pi b^2}{2}L^2 \ln\left(\frac{R_e}{L}\right)$, which will be discussed in the following.

5.1.3 Estimation of dislocation related parameters

The quantitative values of dislocation related microstructural parameters, such as: dislocation density, outer cut-off radius and dislocation arrangement parameter of the differently deformed specimens were easily determined from the Eq. (2.24) (Chapter 2). The variation of $\frac{Y(L)}{L^2}$ with $ln(L)$ of differently cycled specimen were presented in Fig. 5.4, and it is linearly fitted according to the Eq. (2.24) whose slope and Y-intercept gives the dislocation density and outer cut-off radius, respectively. Fig. 5.4 clearly demonstrate that the slope of $\frac{Y(L)}{L^2}$ vs $ln(L)$ plot decreases as the number of fatigue cycle increases, and which indicate towards an interesting fact that the dislocation density at saturation stage is comparatively lower as compare to its pre-saturation stage for both the specimens. However, the microstructural parameters of both the specimens obtained from the XPLA are listed in separate tables. The parameters related to the different stages of the graded grain and CG specimen are presented in Table 5.1.

Table 5.1: Microstructural parameters obtained using X-ray line profile analyses.

Sample	No of cycles	Lattice parameter, Å ±(0.0003-0.0006)	Contrast factor, C_{111} ± (0.01-0.02)	Dislocation character parameter, q	Dislocation density, ρ ($\times10^{14}$ m^{-2}) ± (0.12-2.35)	Outer cut-off radius of dislocation, R_e (nm) ± (5-8)	Stacking fault probability, ($P_{sf}\times10^{-4}$) ±(0.00001 - 0.0004)	Dislocation arrangement parameter, $M(=R_e\sqrt{\rho})$	SFE, γ (mJ/m^2) ± (3.5)
Graded grain	10000	3.6085	0.0742	2.16	3.01	146	4.6	0.4018	
	100000	3.6082	0.0863	2.02	2.82	192	2.1	0.4038	21
Coarse grain	5000	3.6061	0.0591	2.33	2.57	117	3.6	0.4067	16
	100000	3.6073	0.0733	2.17	2.13	142	2.3	0.4125	

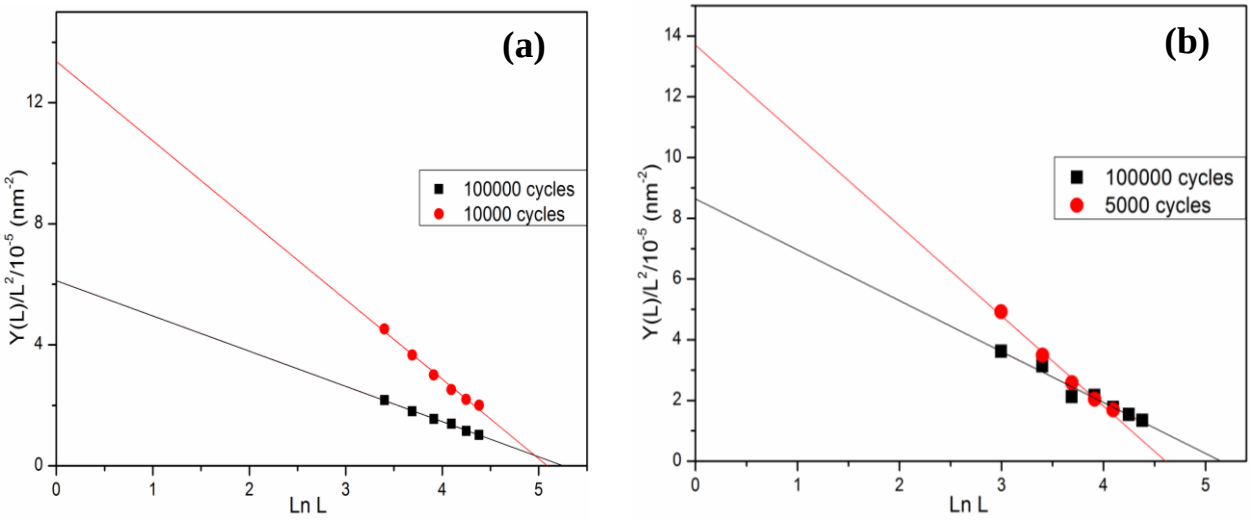

Fig. 5.4: Linear fitting to the variation of $Y(L)/L^2$ with $ln(L)$ according to Eq. (2.24) for: (a) graded grain (b) CG specimen.

5.1.4 Assessment of planar faults parameters

It is well established from Warren's planar fault theory (Warren, 1969) that the presence of significant amount of planar faults (SFs and/or twins) in the microstructure can be identified through the manifestation of asymmetry and selective opposite shifts in the (111) and (200) Bragg reflections in the XRD patterns of the material. In general, the presence of significant amount of SFs shift the (111) Bragg reflection towards the higher diffraction angle while the (200) Bragg reflection shift towards the lower angles, and which also observed previously for high-Mn steels containing significant SFs (Mahato *et al*., 2015). On the other hand, twins (i.e. overlapping SFs) do not cause any opposite shifts, but they introduce asymmetry in the most prominent (111) Bragg reflection in case of austenite. To understand the effects of planar faults on the Bragg reflections we need to critically examine the XRD pattern of the differently deformed specimens, and therefore we adopted Rietveld analysis (Rietveld et al., 1969) in this study.

The selected range of the XRD for differently deformed specimens were fitted according to Rietveld refinement (Rietveld et al., 1969) procedure using Material Analysis Using Diffraction (MAUD), and also presented in Fig. 5.5. It is clearly seen from the fitted XRD plot in Fig. 5.5(a) that the graded grain specimen remains fully

austenite in both pre-saturation and saturation stages, whereas Fig. 5.5(b) suggest that the CG specimen is fully austenite only in pre-saturation stage and some extent of $\gamma \rightarrow \epsilon$ martensitic transformation were observed at saturation stage that clearly indicate the occurrence of deformation induced martensite transformation at saturation stage. It should be mentioned here that due to a high cycling frequency of 23 Hz the temperature rise, and that might cause phase transformation. We have measured the temperature of the gauge regions of the specimens during the mechanical testing by an IR-camera at the center of specimen, and a maximum temperature increment of 100 °C was recorded. In case of the present TWIP steel, the austenite structure is stable at room temperature and also remains naturally stable at such elevated temperatures. Therefore, we can assure that the $\gamma \rightarrow \epsilon$ martensitic transformation observed in CG specimens was occurs due to cyclic deformations.

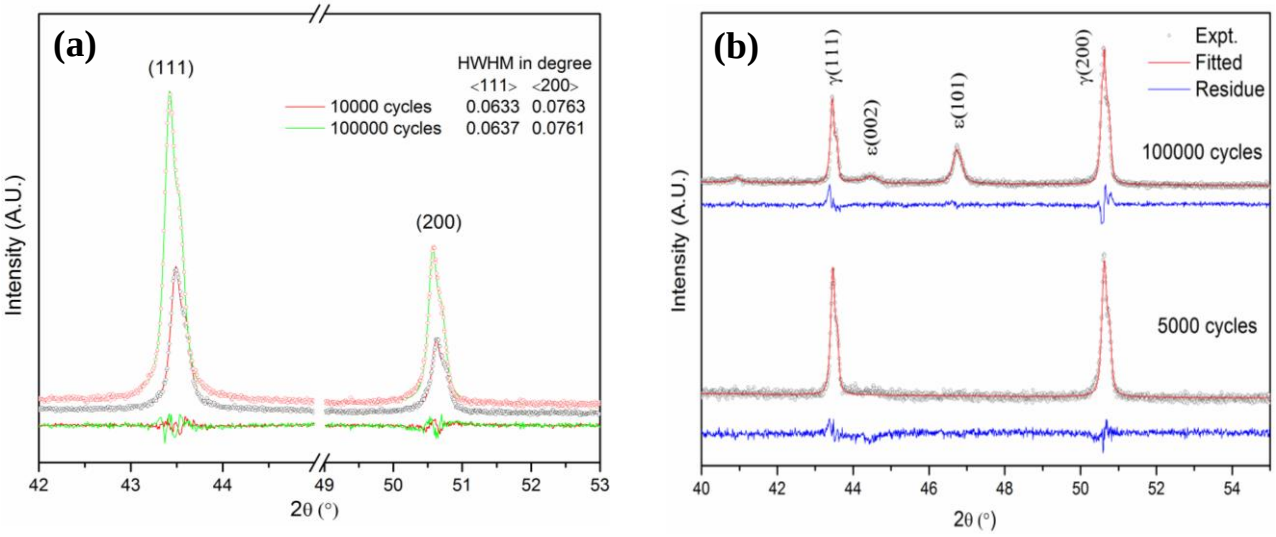

Fig. 5.5: Selected range of fitted XRD patters for (a) graded grain (b) CG specimen.

The volume fraction of $\epsilon-$martensite phase present in the deformation microstructure of the CG specimen was estimated using Rietveld analysis (Rietveld et al., 1969), and it is found that only ~ 15% of austenite were transformed into $\epsilon-$martensite at saturation stage. Interestingly, both the XRD plots in Fig. 5.5 clearly reveals that there was neither any profound asymmetry nor any noticeable opposing shifts in the most prominent (111) and (200) Bragg reflections. However, a detailed description related to the peak shape parameters of the differently deformed specimens

exceeds the scope of the present study. Further, the relative intensities of the characteristic Bragg reflections at differently cycled specimens were in good agreement with values reported in the International Centre for Diffraction Data (ICDD) indicating weak texture development during cyclic deformation, and which also fulfill the requirement of randomness in X-ray powder diffraction thus an accurate estimation of planar faults parameters can be done using XLPA methods. The determination of SF probabilities was done according to Eq. 2.27 (Chapter 2), and it is further used in Eq. 4.2 (Chapter 4) to evaluate the SFE value of the differently deformed specimens. It is to be mentioned here that unlike undeform specimen as describe in Chapter 4, the SFE estimation using the WBDF imaging technique at both deformation stage (pre-saturation & saturation) is not possible due to the evolution of complex dislocation configurations in the deformation microstructures. Therefore, the SFE of the deformed specimens were done only considering the XRD approach as proposed by Schramm and Reed (Schramm & Reed, 1975), and later modified by Dey *et al.* (2005). The estimated values related to the planar fault parameter i.e. stacking fault probability and SFE values of the corresponding deformed specimens are also included in Table 5.1, and which clearly indicate towards a common trend for both the specimen i.e. a reduction in SFs probability value in saturation stage as compared to its pre-saturation stage.

5.2 Deformation microstructure in terms of dislocation related parameters

It is well known that the primary deformation mechanism of any material is governed by dislocation glide, and the strength of the material directly depend on the dislocation density of the deformation microstructures. Therefore, it is expected that dislocation density increase with deformation, but in this study both the specimen show a reverse trend of dislocation density with deformation. The estimated dislocation density values in Table 5.1 clearly display that the dislocation density in pre-saturation stage is higher than the saturation stage, though the order of magnitude is same ~10^{14}. It can be infer from the dislocation density trend that the imposed plastic strain due to cycling decreases at saturation stage as compared to its pre-saturation stage, which causes a reduction in the dislocation density value. It can also be easily verified from the fitted XRD patterns in Fig. 5.5, which reveals that the full width half maxima (FWHM) of the most prominent Bragg reflections (111 & 200) are reduced in pre-saturation stage

as compared to its saturation stage. Additionally, it is also noted from Table 5.1 that as the number of fatigue cycle increases the average contrast factor related to the Bragg reflection (111) i.e. $\bar{C}_{111}$ increases. The marginal increments of $\bar{C}_{111}$ values indicate that although the dislocation density decreases, but the dislocation induced strain anisotropy is prominent at higher cycles.

Apart from dislocation density, another important microstructural parameter related to the deformation microstructure signify the level of shielding of the strain field of dislocations depending on the arrangement of dislocations is dislocation outer cut-off radius, R_e (Wilkens *et al*., 1970; Ungar *et al*., 1998b). The R_e values in Table 5.1 reveal that they are quite large as compared to other high-Mn steel (Sahu *et al*., 2012) deformed under monotonous loading. Generally, R_e value decrease with increasing strains, essentially due to formation of strongly correlated dislocation substructures at large strains, namely, tangles, cells (Sahu *et al*., 2012) under monotonic deformation. A lower R_e values were obtained for both the steels at pre-saturation stage, and it increases at saturation stage (Table 5.1). Thus, the variation in R_e values in the present study indirectly indicate that the dislocations in the present steels become strongly correlated at saturation stage, and their correlation decreases marginally at saturation stage. It is important to be mentioned here that a lower R_e value suggest a higher degree of shielding of the strain field of dislocations by other dislocations, and that can only be possible by the different arrangement of dislocations configurations. Interestingly, both the specimen show moderately high R_e value at saturation stage as compare to their pre-saturation stage, and that suggest towards a critical fact that at saturation stage the dislocations in the microstructures have arranged themselves in such a way that their shielding capability were decreased.

An additional explanation could be put forward to explain the low R_e values observed at pre-saturation stage (Table 5.1). If the strain fields of the individual dislocations screen each other than the total distortion within the lattice will be marginal, and in such situation a smaller value of R_e is expected and consequently, the dislocations would arrange into dipoles and/or low angle grain boundaries (Gubicza, 2014). The dipole character of dislocations is further related to the dislocation arrangement parameter, $M=R_e\sqrt{\rho}$, which can be easily determined using XLPA and the estimated M values of differently deformed specimens are also listed in Table 5.1. In

general, the parameter M signify the dislocation arrangement and whose values smaller or greater than unity indicate the strong or weak dipole nature, respectively (Wilkens, 1970; Borbely *et al*., 2000). Surprisingly, almost same M values were obtained which lies in between 0.4018 to 0.4125 for both the steels irrespective of their deformation stage (Table 5.1). The determined dislocation arrangement parameter value for both steel samples unequivocally reveal a high degree of correlation among the dislocations within the microstructures. Consequently, we anticipate the presence of distinct dislocation substructures in the deformed microstructure, and this phenomenon will be explored further through TEM investigations.

5.3 Deformation microstructure from SFE perception

It is well accepted that the SFE of high-Mn austenitic steels plays a crucial role in controlling the deformation behavior of the steels (Martin *et al*., 2016), and depending on the SFE value different plasticity enhancing mechanisms such as: twining induced plasticity (TWIP), transformation induced plasticity (TRIP) and micro-band induced plasticity (MBIP) activates. It is well known that for the high-Mn steels having SFE value less than 20 mJ/m^2, $\gamma \rightarrow \epsilon$ transformation act as a dominant deformation mechanism while the TWIP effect dominates for the SFE value lying in between 20 to 40 mJ/m^2, although the range of SFE value related to activation of different deformation mechanism varies marginally in different studies (De Cooman *et al*., 2018). Usually, SFE of a material is considered as intrinsic material property, but the presence of different microstructural defects in the deformed microstructures have great influence on SFE, and thus experimentally determined SFE value from a deformed specimen might be affected by the interaction of SFs with other microstructure defects (Mahato *et al*., 2015; Rafaja *et al*., 2014). Therefore, the estimated SEF values in Table 5.1 are different from the actual SFE of the material and it named as the effective SFE of the material as discussed in §4.1 (Chapter 4).

The various microstructural parameters related to the different deformation stages that were used in SFE estimation of the specimens, and the estimated effective SFE values are presented in Table 5.1. It is clearly observed from Table 5.1 that the average SFE is $\gamma \sim 21$ mJ/m^2 for the graded specimen, while it decreases to ~ 16 mJ/m^2 for the CG specimen, and the estimated SFE values matched quite well with the reported thermodynamic SFE value having almost similar types of compositions

(Hamada et. al., 2009). The estimated SFE value in Table 5.1 clearly shows that the SFE value of graded grain specimen lies in the range where a mixture deformation twin and $\gamma \rightarrow \epsilon$ transformation is possible, while the SFE value of CG specimen suggest only $\gamma \rightarrow \epsilon$ transformation and interestingly the selected range XRD pattern of CG specimen in Fig. 5.5(b) shows the presence of deformation induced ϵ martensite at saturation stage. However, the validations of actual deformations microstructures related to the differently deformed specimens at different deformation stage will be introspected thoroughly under TEM investigations, which is briefly discussed in § 5.5.

Another critical observation of SFE values in Table 5.1 indicate that the estimated SFE value decreases as the grain size increases. Interestingly, Volosevich *et al.* (1976) already proposed that the SFE could be greatly influenced by the grain size of the materials while studying the deformation behaviour of Fe-Mn binary alloys. Later, Takaki *et al*. (1993) also verified the hypothesis proposed by Volosevich, and showed that as the internal stresses are strongly correlated with the grain size of a material and therefore any change in grain size produce a distinct internal stress and that cause a change in the dislocation dissociation width of a perfect dislocation. Another proposition was also put forward by Lee and Choi et al. (Lee & Choi, 2000) to explain the grain size dependency of SFE of high-Mn steels, and they suggest that when the grain size is smaller than the equilibrium separation width of a perfect dislocation then grain boundary might act as a geometric obstacle to the dissociation of perfect dislocations, which causes a high SFE value for fine grain specimen. Lee and Choi (Lee & Choi, 2000) also reported that the influence of grain size on SFE is most pronounced when the grain size is 5 μm or smaller, and interestingly the graded grain specimen used in this study composed of grains with an average grain size of ~ 2 μm (Chapter 3), which is well below than 5 μm. Therefore, the reduction in SFE value with the increment of grain size in the present steel could be understood in terms proposition made by Lee and Choi (Lee & Choi, 2000).

Another aspect of the observed SEF value suggests that the estimated SFE values are different from the actual SFE, which is an intrinsic property of the material. In case of high-Mn steels Mahato *et al*. (2015) shown that the experimentally estimated SFE value can be modified due to the influence of several microstructural defects in the microstructure and therefore the effective or apparent SFE can manifest even more than

two-fold increase from the ideal SFE under monotonic loading (Mahato *et al*., 2015; Rafaja *et al*., 2014). The previous extensive investigations on SFE value estimation using different methods (Chapter 4) also produce quite similar SFE value for the given specimen at undeformed conditions, and which suggest an interesting fact that unlike the monotonic loading, the cyclic loading produce such microstructural defects whose influence on SFE value is minimal for the studied steels. Therefore, it is expected that the deformation microstructures of high-Mn steels under cyclic loading will be completely different than its deformation microstructures produced under monotonic loading. Additionally, it must be mentioned here that the deformation twin generally occurs in the deformation microstructure of high-Mn steels under monotonic loading as they have a major role in their deformation behaviour (De Cooman *et al*., 2018), whereas extensive shear bands (SBs), dense dislocation wall, channel-vain dislocation structures, persistent slip bands (PSBs) are the main characteristic deformation microstructures of high-Mn steels under cyclic loading, although twins are observed in some specimens consisting only large grains (Karjalainen *et al*., 2012; Shao et al., 2017). However, the detailed microstructural features of the deformation microstructures of the differently cycled specimens were investigated in the next sections.

5.4 EBSD investigations

The deformation microstructures of the studied steels were studied at both stage, pre-saturation and saturation stages, using EBSD techniques and the outcome of the EBSD investigations for the graded grain specimens and CG specimens are presented in Fig. 5.6 and Fig. 5.7, respectively. The image quality (IQ) maps of the graded grain specimens in Fig. 5.6(a) & (c) represents the pre-saturation stage and saturation stage EBSD micrographs, respectively. Furthermore, the misorientation angles of the internal interfaces, i.e. grain boundaries (GBs) and/or twin boundaries (TBs) of the graded grain specimen were investigated by EBSD analysis. Fig. 5.6(b) & (d) represent the misorientation angle distributions for the corresponding EBSD image quality (IQ) maps presented in Fig. 5.6(a) and (c), respectively. It can be easily infer from Fig. 5.6(a)-(b) that at pre-saturation stage, the high-angle grain boundaries

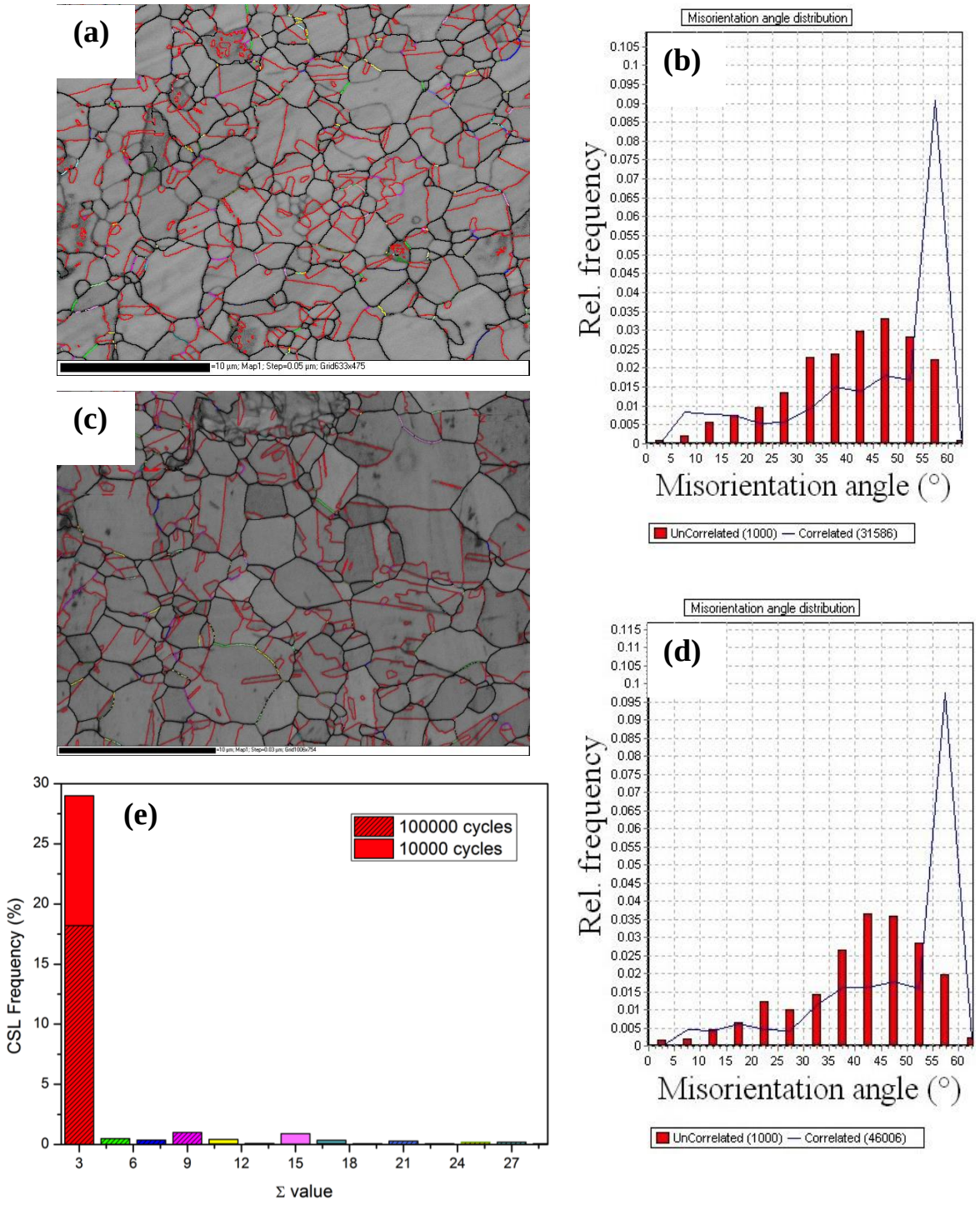

Fig. 5.6: EBSD observations of graded grained specimen: (a) IQ map after 10000 cycles. (b) GBCD after 10000 cycles. (c) IQ map after 100000 cycles. (d) GBCD after 100000 cycles. (e) Frequencies of CSL with increasing ∑ at each cycle.

(HAGB) i.e. having misorientation ≥ 15° are quite predominant, while the low-angle grain boundaries (LAGB) are nearly non-existent (represented as black lines). On the other hand, an interesting observation in Fig. 5.6(a) is that numerous twin boundaries

were recognized in EBSD (represented as red lines) at pre-saturation stage, and whose propensity decreases at significantly at saturation stage; although the HAGB and LAGB character distributions remains nearly invariant in Figs. 6.1(b) & (d).

Additionally, the frequencies of various coincidence site lattice (CSL) boundaries of the graded grain specimen deformed to pre-saturation stage (10000 cycles) and saturation stage (100000 cycles) are further presented in Fig. 5.6(e). It is clearly evident from Fig. 5.6(e) that only ∑3 CSL boundaries are the predominant in nature. However, beside the prominent ∑3 boundaries very few higher order CSL boundaries ($\sum 3^n$, n > 1) were also observed at both deformation stage, and that are also plotted in Fig. 5.6(e). It should be mentioned here that the GBs/TBs with ∑3–∑29 that are considered as low ∑ (or special boundaries) are plotted in Fig. 5.6(e), while the random boundaries having ∑ value beyond 29 were deliberately omitted. An interesting observation of Fig. 5.6(e) is that the density of ∑3 boundaries in the microstructure decreases at 100000 cycles as compared to 10000 cycles, which advocate towards an interesting fact that the removal of ∑3 boundaries occurs at higher cycles may be due to sliding of ∑3 boundary. Therefore, the presence of any types of faceted internal interfaces (TBs and GBs) are expected in the microstructures and that will be confirmed under TEM studies.

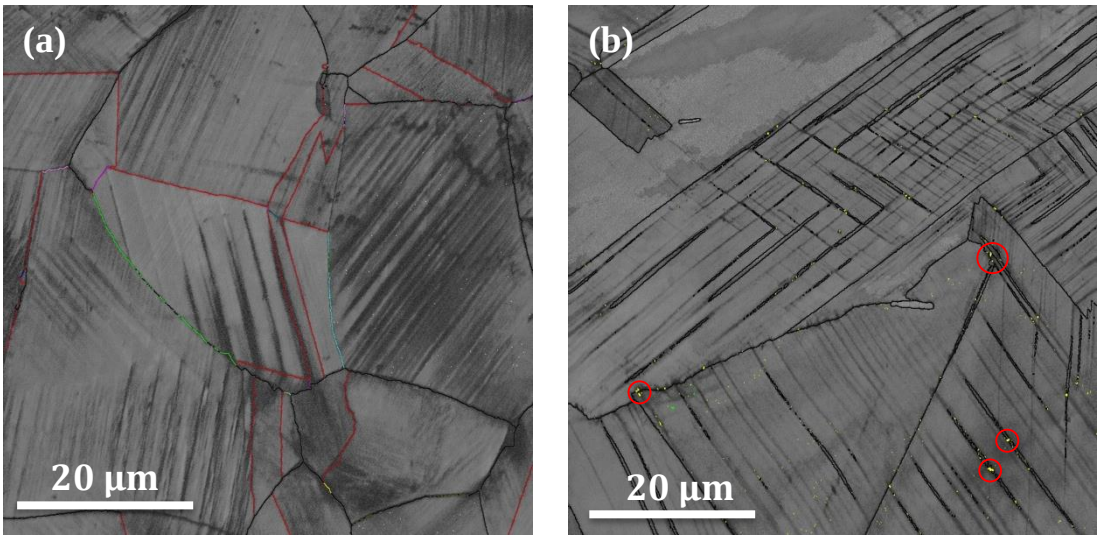

Fig. 5.7: EBSD microstructures of CG specimen showing: (a) EBSD image quality map at pre-saturation stage. (b) EBSD IQ image overlapped with phase map showing the presence of ϵ martensite phase (encircled in red) at saturation stage.

Similarly, the EBSD microstructure of the CG specimen at pre-saturation stage and saturation stage are presented in Fig. 5.7 (a) & (b), respectively. The EBSD IQ map overlapped with phase map in Fig. 5.7(a) reveals that the deformation microstructure was fully austenitic in nature and the microstructures comprises of extensive shear bands (SBs) at pre-saturation stage (5000 cycles). The presence of extensive SBs at pre-saturation stage intuitively suggests towards an interesting fact that at this stage i.e., pre-saturation stage, the cyclic deformation behaviour of the steels is primarily controlled by dislocation slip activity. However, after 100000 cycles i.e., in the saturation stage; several new features were evolved in the deformation microstructure and the situation is exemplified in Fig. 5.7(b). The EBSD IQ map overlapped with phase map in Fig. 5.7(b) indicate not only the profoundness of intense SBs as compared to 5000 cycles i.e. pre-saturation stage (Fig. 5.6(a)), but also it clearly indicate the presence of strain-induced $\epsilon-$ martensite in the deformation microstructure at saturation stage. The occurrence of $\epsilon-$martensite Fig. 5.7(b) can be easily found within the SBs regions that were delineated in yellow, and few of which were also encircled in red. Interestingly, the XRD findings also supports the EBSD observations and that can also be reaffirmed from the most relevant range XRD plots in Fig. 5.5(b). Generally, the strain-induced $\epsilon-$martensite is observed in case of monotonic deformation of TWIP steels having a low SFE (Allain et al., 2004; Kim et al., 2016), but its prevalence during the cyclic deformation is not well known. However, the occurrence of is interpreted in terms of overlapping SFs on alternate closed-packed $\langle 111 \rangle$ austenite planes. This also results in a reduction in P_{sf} value at saturation stage of the CG specimen, as listed in Table 5.1, since some of the SFs systematically arranged on alternate $\langle 111 \rangle$ planes are interpreted as ϵ-martensite in Rietveld analysis (Rietveld et al., 1969).

5.5 TEM investigations of the deformation microstructure

Unlike XRD and EBSD techniques, the TEM is a direct observation technique that can give the direct flavour of microstructural features present in the deformation microstructures and therefore the main aim of this section is to reveal the active deformation mechanism prevailing in the steel at different deformation stage from TEM point of view and its correlation to the cyclic deformation behavior. In this portion, the TEM investigations of the differently deformed specimens are reported and the

corresponding implications on the deformation mechanism(s) are critically introspected. Depending on the deformation stage, the following sections are divided into two parts, one part of which deals with the pre-saturation stage microstructures while the other describe the deformation microstructures related to the saturation stage of the specimens.

5.5.1 Pre-saturation stage

In this section, we will discuss the deformation microstructures related to the pre-saturation stage of both the steels i.e. the graded grain and CG specimens. A set of BF micrographs obtained from the graded grain specimen deformed to 10000 cycles (pre-saturation stage) are presented in Fig. 5.8, which reveals several interesting microstructural features. As expected from the EBSD observations discussed in § 5.4, the TEM micrograph in Fig. 5.8(a) clearly indicates the existence of micro-facetted GB/TB and which is also delineated using yellow rectangle. A careful observation of Fig. 5.8(a) also shows a SF, which originates from the micro-facets of the regions and extends towards the grain interior. It should be mentioned here that the ledges in a GB/TB arise due to faceting, and therefore the coherency of the facetted GB/TB is lost but at the same time its mobility greatly enhanced (Sutton, 1995). Now if we can recall the initial microstructure observed in Chapter 4 then we found that the graded grain specimens comprise of few larger grains of grain size ~ 5 μm along with finer grains of grain size ~ 2 μm. Further, it is well known that the deformation microstructure strongly influenced by the grain size of the material. Therefore, we expect different deformation microstructure related to grains of different size, and thus the TEM observations were made for both, the lager and smaller grains.

Fig. 5.8(b-c) shows that deformation microstructures related to the finer grains, while the microstructural features of larger grains is presented in Fig. 5.8(d). It can be easily observed from Fig. 5.8(b) that it contains only wide SFs with negligible dislocation activity, whereas Fig. 5.8(c) shows a completely different features which shows that the widening of SFs in fine grains can be restricted by dislocation configurations. Therefore, Fig. 5.8(b-c) together advocate towards an important fact that there is a competition between the line defect and planar defect, and the grains with deficient dislocation activity promote the extension of SFs (Fig. 5.8(b)), while

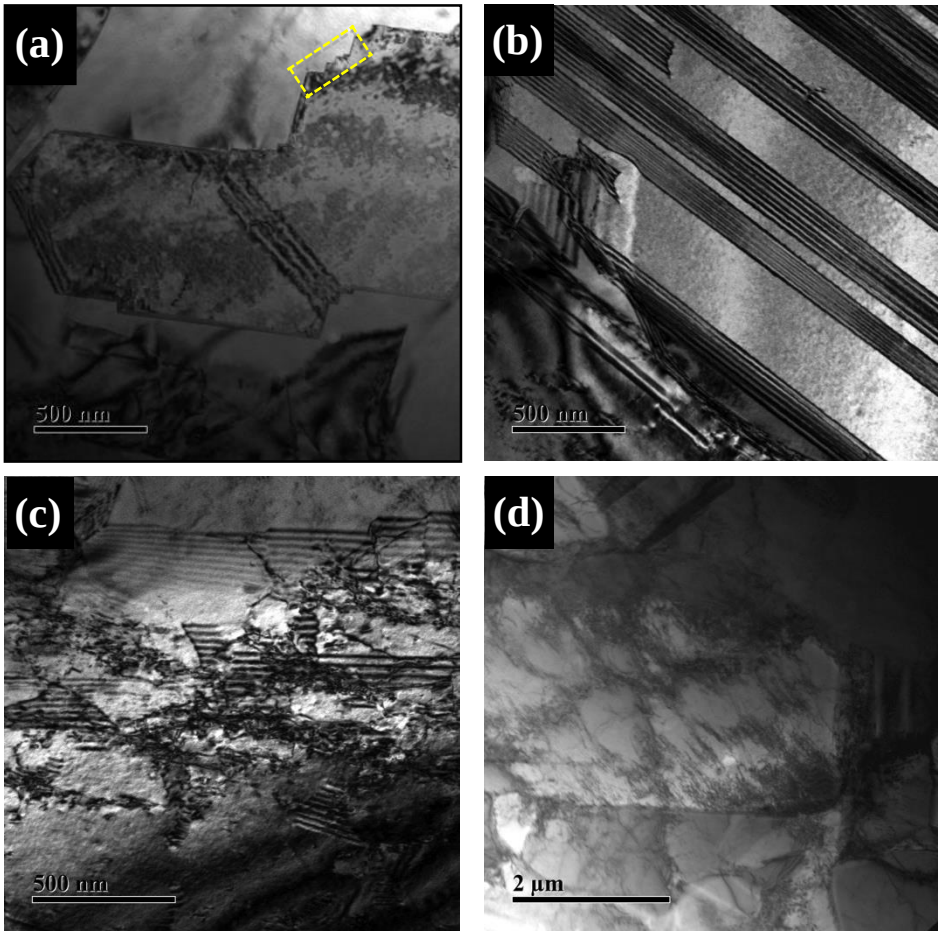

Fig. 5.8: TEM microstructures of graded grain specimen after 10000 cycles showing: (a) faceted TB/GB and a SF originating from micro-facets. (b) Long hindered SFs within FG. (c) Dislocations hindering widening of SFs in FG. (d) Developing dislocation cells within larger grains.

the reverse is also true i.e. the extension of SFs were restricted by the dislocation activity in some grains which was also clearly observed in Fig. 5.8(c). However, a complete distinct microstructure was observed for the larger grains, and the TEM micrograph in Fig. 5.8(d) reveals a developing dislocation cell pattern. Interestingly, no twins were observed at this pre-saturation stage, neither in finer or larger grains. It is known that slip usually precedes twinning, while the later occurs when the imposed plastic strain rate cannot be completely accommodated through dislocation slip, thereby requiring additional deformation mechanisms. The existence of dislocation cells in Fig. 5.8(d) indicates that activation of multiple slips can sufficiently accommodate the imposed plastic strain without requiring twinning as an additional deformation mode.

A set of BF micrographs obtained from the CG specimen deformed to 5000 cycles (pre-saturation stage) are presented in Fig. 5.9, which reveals several interesting microstructural features that are mostly different from the microstructures observed in graded grain specimen (Fig. 5.8). Interestingly, the presence of extensive SBs at pre-saturation stage as previously observed from EBSD microstructure were also reaffirmed by TEM BF micrograph in Fig. 5.9(a), and therefore, one can confirmed the fact that the pre-saturation stage of the high-Mn steels under cyclic deformation is primarily controlled by dislocation slip and SBs formations. Additionally, Fig. 5.9(a) demonstrates special types of microstructural features which are often known as channel-vein structure of dislocation walls, and that is partly transformed into a ladder-like structure while the ladder is usually observed inside persistent slip bands (PSBs) (Mughrabi et. al., 1979). However, the dislocation walls in Fig. 5.9(a) do not completely resolve into sharp channels at this pre-saturation stage and the schematic of the microstructure is also presented in Fig. 5.9(b) to understand the observed deformation microstructure in more scientific approach.

Fig. 5.9(b) clearly reveals the co-existence of dislocation walls inside the SBs delineated using grey shade regions and the onset of a ladder-like structure within the diffusive channels. Further, the dislocation walls with in the persistent slip band like (PSB) region marked as: A', B' and C' moves faster within the channel regions than those inside the SBs regions labelled as: A, B and C in Fig. 5.9(b). The differential velocities of the dislocation walls between the two regions produces bending curvatures in the dislocation walls, and which are clearly observed in Fig. 5.9(a). Although the differential velocities of the dislocation walls produce bending, but the dislocation walls arrange themselves in a way that they remain nearly parallel within the two regions. On the other hand, Fig. 5.9(c) emphasizes some interesting details about the pre-saturation dislocation structure that clearly reveals that SFs and perfect dislocations co-exist and the widening of SFs was restricted by the prevailing dislocation activity, which also indicate almost similar kind of features as observed in case of graded grain specimen (Fig. 5.8(c)). However, no twins are observed in this pre-saturation stage, and that also coincide with the observation for graded grain specimen. Therefore, alike the graded grain it can be concluded that the imposed plastic strain in the pre-saturation stage of CG specimens were accommodated through the creation of SFs and dislocation

channel-vein structures. The occurrence of PSB like structures can easily be understood using static-dynamic (SD) model of PSBs formation, and which is discussed below.

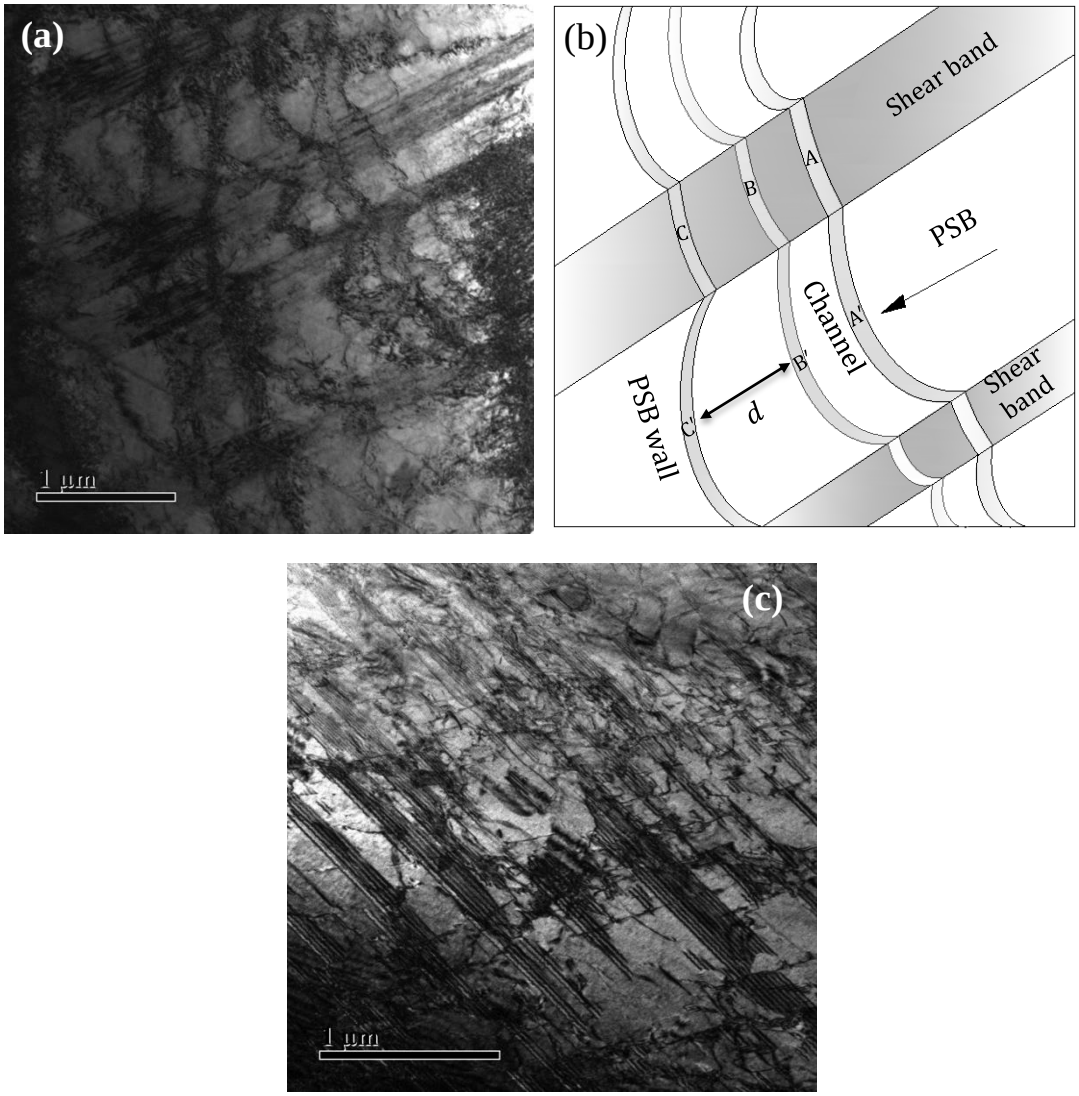

Fig. 5.9: TEM micrographs $B \approx [110]$ at pre-saturation stage of GC specimen showing: (a) SBs and PSB like structure. (b) Schematic representation of (a). (c) Dislocations hindering the widening of SFs.

According to static-dynamic model (Pedersen et al., 1996) of PSB formation, the average separation distance (d) between two PSB walls is proportional to the annihilation distance (X_s) of the screw dislocations and can be expressed as: $d \approx 4\pi X_s$. Again, the screw the annihilation distance of a materials can be approximated as (Li et al., 2017): $X_s \approx \frac{Gb}{2\pi\Delta\sigma}$. Inserting the value of shear modulus of the steel, $G \approx 65$ GPa (Karjalainen et al., 2012), Burgers vector, $b \approx 0.2565$ nm, determined from Rietveld

analysis (Rietveld et al., 1969), and the difference between the effective stress and the saturation stress, $\Delta\sigma \sim 328$ MPa (Karjalainen et al., 2012), one can estimate $d \approx 0.63$ μm (Fig. 5.9(b)). Interestingly, the estimated d value as predicted by SD model is very much comparable with the average PSB wall separation distance ~ 0.50 μm measured from TEM micrograph (Fig. 5.9(a)). Although no such prominent PSBs were observed in this study, but this calculation seems tenable here since a ladder-like structure is observed in PSBs and which are often observed in case of low SFE metals/alloys deformed under cyclic deformation (Li et al., 2017). Moreover, the dislocation ladders like structures continue to preserve the average separation distance among themselves, which is in good agreement with the requirements of PSB formation according to the SD model (Pedersen et al., 1996).

5.5.2 Saturation stage

Like previously discussed pre-saturation stage microstructures in § 5.5.1, now we will discuss the deformation microstructures related to the saturation stage of both the steels i.e. the graded grain and CG specimens. A set of BF micrographs obtained from the graded grain specimen deformed to 100000 cycles (saturation stage) are presented in Fig. 5.10, which reveals several interesting microstructural facts related to the deformation microstructures. Fig. 5.10(a) clearly shows an overlapping SFs with in a fine grain may be due to the activation of a greater number of slip systems at higher cycles and the characteristic periodic contrast of Shockley partials in high-Mn steels generally indicate the precursor of deformation twin nucleation (Mahato et al., 2015), and the observed twin lamella in Fig. 5.10(a) was also delineated using yellow rectangle. Interestingly, no prominent discernible dislocation substructure is observed in the same grain, and which advocate towards a well-accepted fact that the grains accommodate the strain mostly by creating the twin faults and thus the dislocation activity were supressed. However, a completely distinct microstructures were observed in case of coarser grains, and that are also presented in Fig. 5.10(b-c).

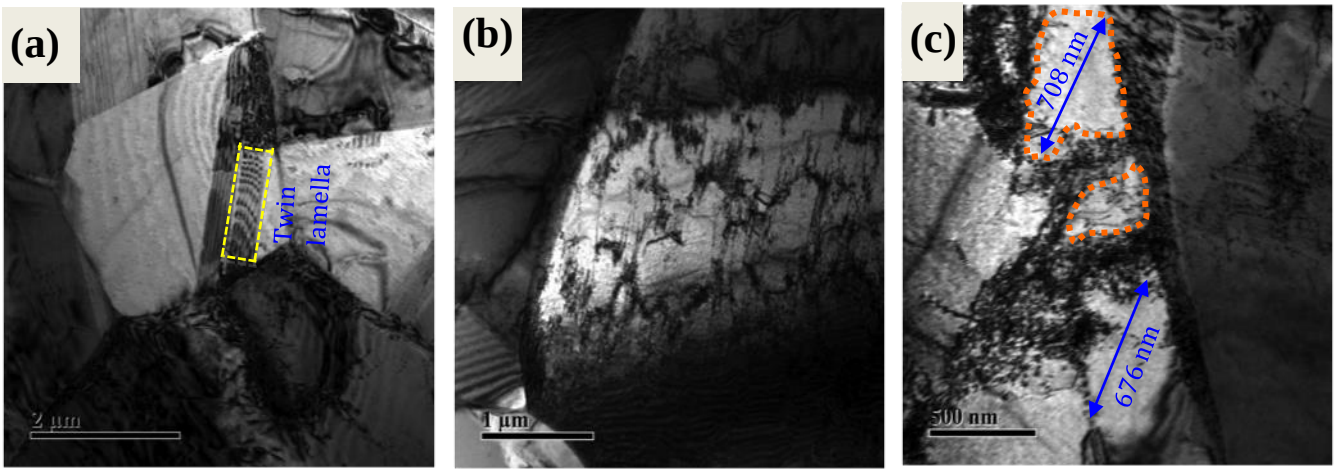

Fig. 5.10: TEM microstructures after 100000 cycles of graded grain specimen showing: (a) A twin lamella within FG region. (b) Interconnected dislocation cell (low magnification). (c) Recovered regions within dislocation cells (high magnification).

The TEM micrograph in Fig. 5.10(b) clearly reveals that dislocation cells become more prominent at this stage as compared to its pre-saturation stage (Fig. 5.8(d)), while the high magnification TEM micrograph in Fig. 5.10(c) reveals the existence of some dislocation cells along with dynamically recovered regions. Interestingly, the absence of twinning in coarser grains is also in good agreement with Boucher and Christian (Boucher et al., 1972) observations suggesting the absence of twin in the grains containing complex dislocation substructure like dislocation cells (Fig. 5.10(b)-(c)). The marginal increment in the microhardness value after 20000 cycles as observed in Fig. 3.4(a) (Chapter 3) could be due to the formation of twins at higher cycles, because they act as barriers to the dislocation motion and contribute to cyclic flow resistance as well as providing obstacles to fatigue crack growth (Karjalainen et al., 2012). The graded microstructures in Cu are reported, and which suggest that the dislocation substructures remain absent in grains up to 0.2 μm in diameter but it may appear in larger grains with diameters 0.1–0.5 μm (Valiev et al., 2000). In our case the graded microstructures of the present high-Mn steels suggest that dislocation cells were observed with in the larger grains, whereas twinning was rarely observed only in the finer grains at saturation stage. However, the occurrence of distinct microstructural features in different grains under cyclic deformation can be understood in terms of the numerical value of the unified evolution factor as suggested by Li et al. (2017), and which was discussed below.

The evolution of graded deformation microstructures in the present steel (Figs. 5.8 & 5.10) has been quantitatively established using the parameter as suggested by Li et al. (2017). Prof. Li and his co-workers proposed an unified factor for cyclically deformed microstructures of pure Cu, Ag and Cu-Al alloys at room temperature, and they suggest that the evolution of various cyclic deformation microstructures, namely, dislocation cells and walls, labyrinth, persistent Luders band (PLB), shear bands and PSBs strongly depends on the annihilation distance (X_s) and split distance (d_{ex}) of a screw dislocations, which are expressed as: $X_s \approx \frac{Gb}{2\pi\Delta\sigma}$ and $d_{ex} = \frac{3}{48\pi}\left(\frac{Gb^2}{\gamma}\right)$ where, G is the shear modulus ≈ 65 GPa (Karjalainen et al., 2012), b is the Burgers vector ~ 0.255 nm, Δσ is the difference between the effective stress and the saturation stress. The effective stress is further regarded as the sum of the lattice friction stress and critical resolved shear stress (CRSS) (Li et al., 2017), which is calculated as ~ 530 MPa using previously reported YS and CRSS values of the steel (Karjalainen et al., 2012), while the saturation stress was approximated as ~ 937 MPa from the microhardness plot of graded grain specimen in Fig. 3.4(a) (Chapter 3), leading to Δσ = 407 MPa. Li et al. (2017) also indicated that for a fixed grain size, the parameter α defined by the ratio $\frac{X_s}{d_{ex}}$, plays a crucial role in the microstructure development in cyclic deformation, and that various dislocation substructures will be generated only if $X_s >> d_{ex}$, which corresponds to the condition $\alpha >> 1$, while for $\alpha \sim 1$, only SFs and dipolar arrays would be expected. Inserting the values of all the parameters the α value turns out to be ~ 1.6 for the present graded grain steel. The estimated α value is comparable to unity, and which can reasonably explain as to why SFs were the only dominant aspects within the finer grains, irrespective of cycle numbers (Li et al., 2017).

Another important microstructural aspect observed in lager grains i.e. the appearances of dislocation cells could further be interpreted by considering that the structure of dislocation cell is influenced by the internal factors, namely; the elastic constants, grain size and SFE value, as well as, the external factors such as: the applied shear stress, dimension, temperature and the other parameters determining the dislocations' mobility (Kuhlmann-Wilsdorf, 1968). It is known that the formation of dislocation cells is more difficult near the grain boundary within the finer grains (Chu et al., 1996) and in corroboration of this, Yu et al. (2014) observed that the formation of dislocation cell was strongly suppressed in Al single crystal pillars for sizes below

2.5 μm. It is also known that the average size of dislocation cell substructure d_{cell} during the deformation of fcc metals/alloys is governed by the well-known Holt relation (Holt et al., 1970). Using the dislocation density value from Table 5.1 and considering the constant K~ 7 (Koneva et al., 2008), the Holt relation i.e. $d_{cell} = \frac{K}{\sqrt{\rho}}$ predicts an average dislocation cell size, d_{cell} ~ 0.4 μm, and interestingly the observed cells sizes in the TEM images Fig. 5.10(c) are also in good agreement with the predicted cell sizes. It is also to be remembered that the dislocation cells in a cellblock are usually interconnected to form a cell network and the chances of forming an isolated dislocation cell is very low (Huang et al., 2001). Therefore, any finer grains would not have sufficient space to sustain any three-dimensional dislocation network generally interconnected and this clearly explain the suppression of dislocation cell formation in the finer grains, while the larger grains would not suffer from any such restrictions due to their relatively extensive size.

The TEM BF micrographs obtained from the CG specimen at saturation stage are presented in Fig. 5.11, which clearly indicate that occurrence of completely different microstructural features as compared to its pre-saturation stage microstructures (Fig. 5.9). A set of parallel and prominently developed SBs in Fig. 5.11(a) clearly advocate towards the fact that the SBs formations are the key features of the deformation microstructures at saturation stage. However, a critical observation of Fig. 5.11(a) reveals the presence of fine SFs in between SBs and that was also highlighted as upper inset in the Fig. 5.11(a), while the lower inset indicates the diffraction conditions in which the TEM micrograph was obtained. A high magnification TEM micrograph in Fig. 5.11(b) shows several intersecting SBs, while the corresponding SAD pattern obtained from the encircled region reveals the existence of ϵ-martensite within the SBs intersection, and which also substantiated the previously observed XRD and EBSD findings presented in Fig. 5.5(b) and Fig. 5.7(b), respectively. The presence of ϵ-martensite in the matrix is known to enhance cyclic flow resistance (Nikulin et al., 2016) and it can also attribute the material strength by acting as an obstacle to the dislocation movement. Therefore, the minor increment in microhardness after 10000 cycles as observed from Fig. 3.4(b) (Chapter 4) can also be justified in terms of the occurrence of ϵ -martensite within the austenite matrix. Another important microstructural feature in Fig. 5.11(c) shows the existence of

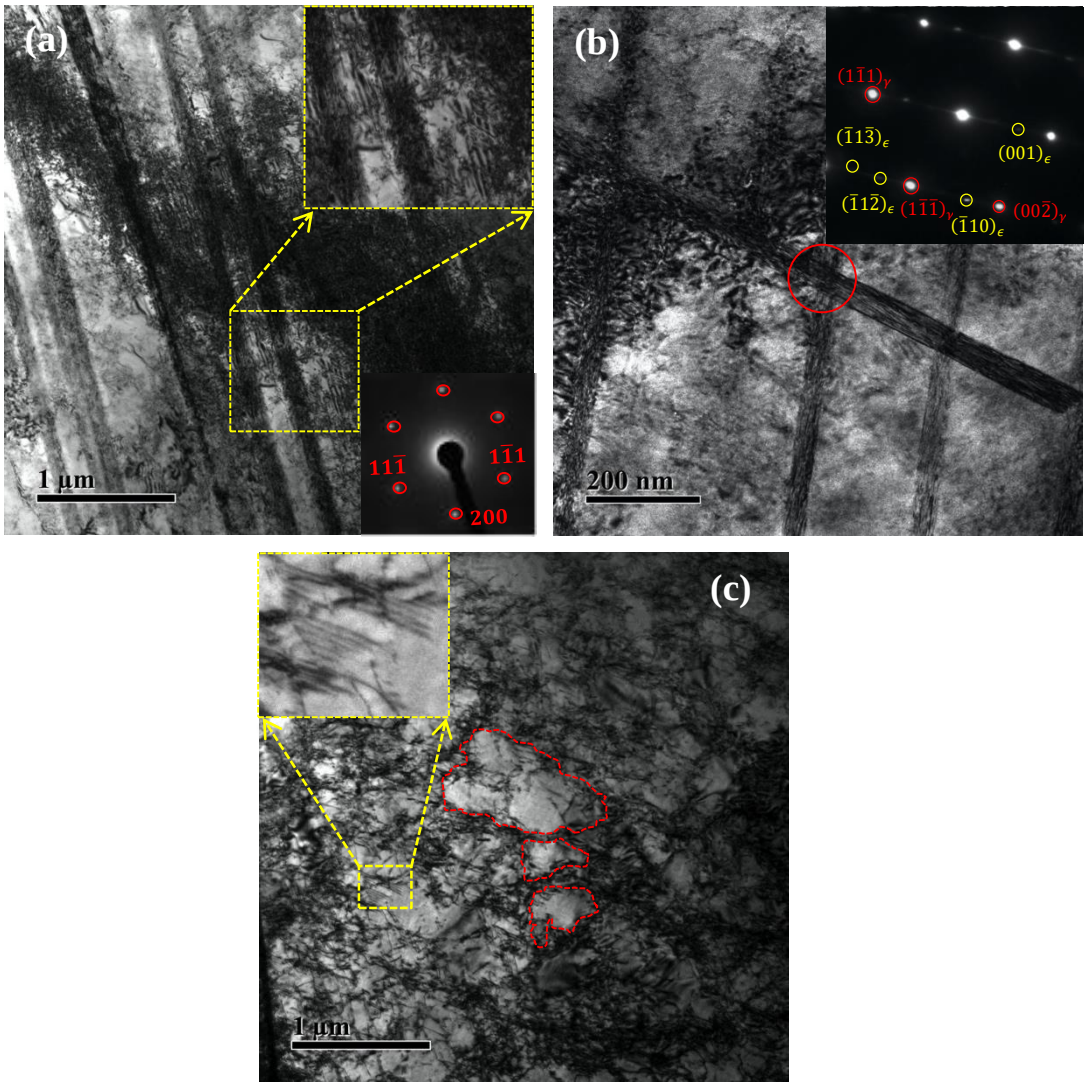

Fig. 5.11: TEM microstructures at saturation stage showing: (a) SBs hindering widening of SFs. (b) SBs intersections at high magnification showing the presence of ϵ martensite phase (encircled in red). (c) Irregular dislocation cluster coexisting with recovered regions.

irregular dislocation clusters coexisting with some dynamically recovered regions, which are delineated in red. However, a critical observation of Fig. 5.11(c) also indicate the presence of tiny SFs within the dislocation cluster regions, and the magnified view of which are shown as an inset and that also outlined in yellow. Interestingly, deformation twins again remained absent quite alike to the pre-saturation stage, which agrees with the previous report that deformations twins during cyclic deformation of high-Mn steels are expected only within fine grains (Shyamal et al., 2021).

References

Allain, S., Chateau, J.-P, et al. (2004) *Mater. Sci. Eng. A* **387-389**, 158-162.
Boucher, N.A., Christian, J.W. (1972) *Acta Metall*. **20(4)**, 581-591.
Chu, J.W.M. D. (1996) *Acta Mater*. **44**, 2599–2610.
D. Kuhlmann-Wilsdorf, in Work Hardening, J. Hirth and J. Weertman, eds., Gordon and Breach, New York, 1968, p.97.
Hamada, A.S., Karjalainen, L.P. & Puustinen, J. (2009) *Mater. Sci. Eng. A* **517**, 68-77.
Holt, D.L. (1970) *J. Appl. Phys*. **41**, 3197–3201.
Huang, J.Y., Zhu, Y.T., Jiang, H., Lowe, T.C. (2001) *Acta Mater*. **49**, 1497–1505.
Karjalainen, L.P., Hamada, A., Misra, R.D.K., Porter, D.A. (2012) *Scr. Mater*. **66**, 1034-1039.
Kim, J.K., De Cooman, B.C. (2016) *Mater. Sci. Eng. A* **676**, 216-231.
Koneva, N.A., Starenchenko, V.A., Lychagin, D.V., Trishkina, L.I., Popova, N.A., Kozlov, E.V. (2008) *Mater. Sci. Eng. A* **483**, 179-183.
Li, P., Li, S.X., Wang, Z.G., Zhang, Z.F. (2017) *Acta Mater*. **129**, 98-111.
Mahato, B., Shee, S.K., Sahu, T., Ghosh Chowdhury, S., Sahu, P, Porter, D.A., Karjalainen, L.P. (2015) *Acta Mater*. **86**, 69–79.
Martin, S., Wolf, S., Martin, U., Krüger, L. & Rafaja, D. (2016) *Metal. Mater. Trans*. A. **47**, 49-58.
Mughrabi, H., Ackermann F. and Herz, K. (1979) *In Fatigue Mechanisms ASTM STP* **675**, 69-105.
Nikulin, I., Sawaguchi, T., Ogawa, K., Tsuzaki, K. (2016) *Acta Mater*. **105**, 207-218.
Pedersen, O.B. (1996) *Philos. Mag.* **73**, 829-858.
Rietveld, H.M. (1969) *J. Appl Cryst*. **2**, 65-71.
Shao, C.W., Zhang, P., Zhang, Z.J., Liu, R., Zhang, Z.F., (2017) *Metall. Mater. Trans. A* **48**, 5833-5848.
Shyamal, S., Das, S.R. et al. (2021) *Mater. Lett.* **285**, 129002.
Sutton, R.W., Balluffi, A.P., (1995) Interfaces in Crystalline Materials, Oxford Univ. Press.
Ungar, T.; Groma, I.; Wilkens, M. J. (1989) *Appl. Cryst.* **22**, 26–43.
Ungar, T., Revesz, A. & Borbely, A. (1998) *J. Appl. Crystallogr.* **31**, 554-558.
Valiev, R.Z., Islamgaliev, R.K., Alexandrov, I.V. (2000) *Prog. Mater. Sci.* **45**, 103-189.
Warren, B.A., Averbach, B.L. (1952) *J. Appl. Phys*. **23**, 497.Yu, Q., Mishra, R.K., Morris, J.W., Minor, A.M. (2014) *Philos. Mag.* **94(18)**, 2062-2071.

Chapter 6*

Monotonic deformation microstructure of the medium-Mn steel

*This chapter is published in Scripta Mater., 192 (2021) 83-88. (No. 1 in the list of publications)

6.1 TEM investigations and its implications on the deformation mechanism

As mentioned in Chapter 3, in this chapter we carried out a detailed TEM investigations on the early stage of deformation microstructures of the specimens of the medium-Mn steel that are deformed to a true strain of ~ 0.02, and also the outcomes of the investigations are briefly discussed here. Furthermore, the influence of the observed early-stage local deformation microstructures on the corresponding deformation mechanism(s) is also critically introspected. The following sections strive to reveal the influence of the locally observed TEM microstructures on the activation of different deformation mechanisms prevailing in the steel at early strain and also to identify the different deformation mechanisms that are activated at this early strain.

6.1.1 Influence of local defects on deformation microstructure

A set of TEM BF micrographs of the specimen strained up to true strain 0.02 are presented in Fig. 6.1, and which clearly reveals several interesting microstructural aspects related to the deformation microstructures of the studied steel containing the V(C,N) precipitates. It can be easily seen from Fig. 6.1 that the observed precipitates are almost spherical in shape as observed from the as-annealed microstructure in Fig. 3.3(b) (Chapter 3), however, a completely different scenario was observed in the regions around the precipitates. As observed from Fig. 6.1, the precipitates are intensely surrounded by high density of forest dislocations at this strain level, whereas, such kind of environment around the precipitates were not observed in case of as-annealed microstructures presented in Fig. 3.3(b) (Chapter 3). The discrepancies between the observed microstructures at deformed and as-annealed conditions i.e. the occurrence of high dislocation density regions in the vicinity of precipitates within the deformation microstructures can be understood in terms of the imposed plastic strain which causes several defect creation in the matrix and thereby increases the dislocation density in the microstructure. However, the dark regions around the precipitates in the TEM micrographs (Fig. 6.1) suggest that the dense forest dislocations in the vicinity of the precipitates associated with a high stress field that can have different consequences on the deformation microstructure of the MMn steel at this strain level, and which will be witnessed now from the critical interpretations of the deformation microstructures discussed below.

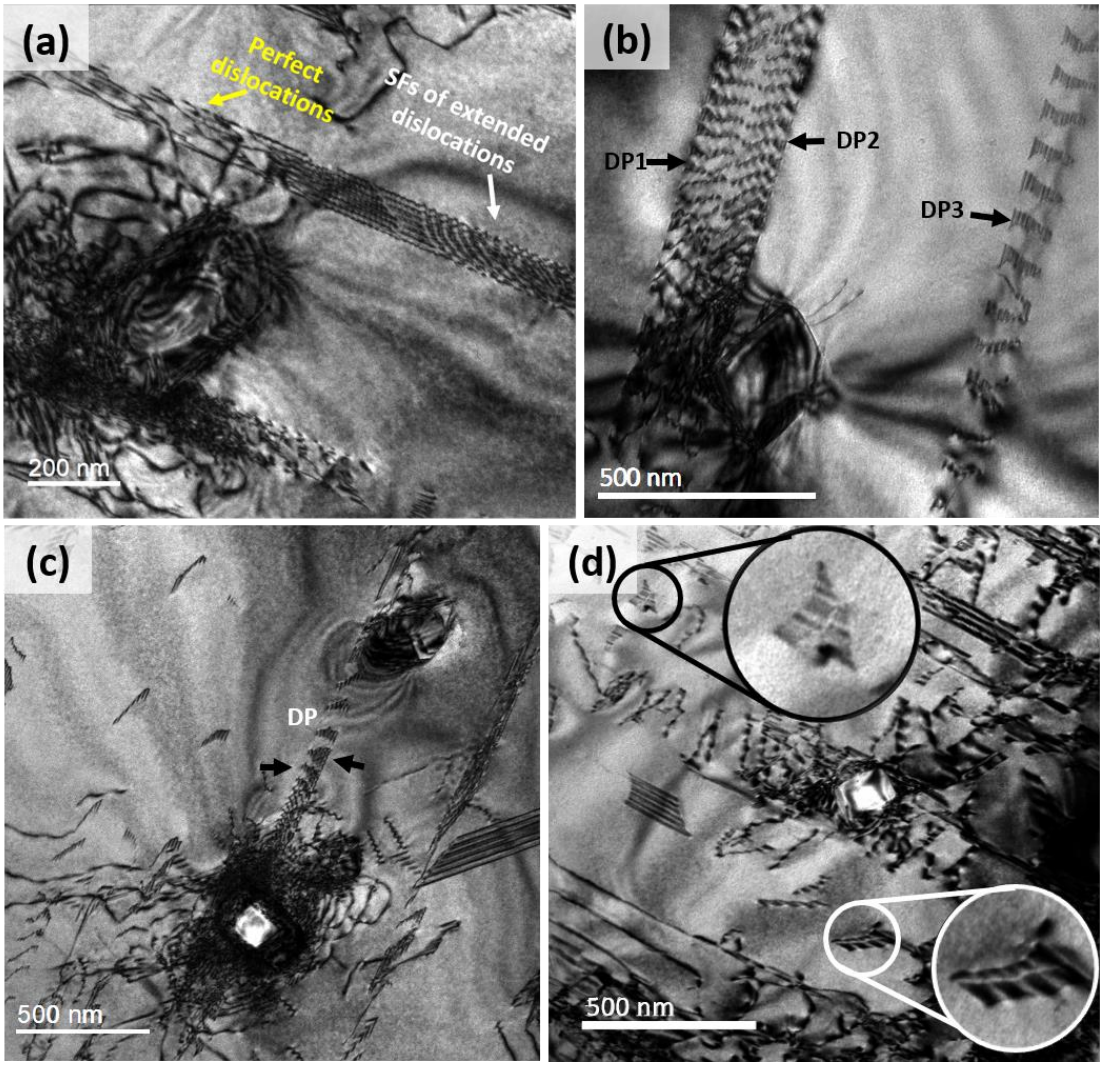

Fig. 6.1: TEM BF microstructures at true strain: 0.02: (a) extended and full dislocations surrounding a precipitate are indicated using white and yellow arrows, respectively. (b) dislocation pile-ups (DPs) observed at different distances from a precipitate (c) nucleation of SFs in a DP is indicated using black arrows (d) nucleation of three-layer twin nuclei, away from the precipitates are encircled and also magnified.

An in-depth observation of Figure 6.1 reveals several intriguing features pertaining to the deformation microstructures, with one notably highlighting the presence of dislocation pile-up (DP) occurring as it traverses through the matrix near the precipitates. A couple of arrows in Fig. 6.1(a) suggest an interesting fact that the dislocation pile-up (DP) comprises of both, the perfect and partial dislocations as delineated using yellow and white arrows, respectively. It is also further seen from Fig. 6.1(a) that as we move away from the precipitate the characteristic SF fringe contrast

becomes prominent with in the pile-up, and the fringed region (i.e. the SF) is narrowed down gradually, and finally disappears as we move closer to the precipitates along the DP. Therefore, the above stated unusual observations suggest that the dissociation of perfect dislocations were strictly restricted in the regions closer to the precipitates, whereas, the dissociation into Shockley partials dislocation (SPD) occurs within the DP only at the end which is far away from the precipitates. Thus, one can infer that the conversion of partial dislocations to perfect dislocations occurs within the DP as the extended dislocations approaches towards the precipitate i.e. near the tip of the pile-up, which is also delineated using yellow arrow.

It is important to mention in this context that any SF removal can only occurs as a result of the following unfaulting dislocation reaction in the Thompson tetrahedron notation described as (Hull & Bacon, 2011):

$$B\alpha + \alpha A \rightarrow BA \qquad (6.1)$$

However, the above-mentioned unfaulting dislocation reactions can occur only under high SFE conditions, and there is a reduction in total energy depending upon the removal of a Frank loop (Hull & Bacon, 2011), but the steel under consideration has a SFE ~ 25 mJ/m^2, calculated using a sub regular solution model (Dinsdale, 1991). It is to be additionally remarked that high SFE here does not refer to the global SFE value of the steel, rather any local high value near the precipitates, arising out of the interaction between SF in the Frank loop with the stress field of the forest dislocations around the precipitates, consequently raising the energy of the SFs according to the concept of effective SFE (Müllner et al., 1996). The removal of SF near the vicinity of the precipitate in Fig. 6.1(a) is further evidenced from the TEM micrograph presented in Fig. 6.1(b). It is clearly seen from Fig. 6.1(b) that there are three independent DPs with in the matrix, which were detected at different distances from the precipitate. Among the observed three independent DPs, two DPs lie close to the precipitate and which are also named as: DP1 and DP2, while the third one i.e. DP3 is found relatively far away from it. Additionally, it is also easily discernible in Fig. 6.1(b) that the SFs in DP1 and DP2 are narrower than the ones detecting with in the third DP i.e. DP3, and that the glide of dislocations in DP1 and DP2 ceases in the immediate vicinity of the precipitate, while it is continuing in DP3.

Furthermore, Fig. 6.1(c) demonstrate another DP captures under a completely different environment as compare to the previously observed DPs, i.e. Figs. 8.1(a & b), in which the precipitates are located only at one end or at the vicinity of the DPs, but not at the both ends of the DP. Interestingly, the DP in Fig. 6.1(c) is located in between two reasonably separated precipitates, and it can be easily seen that the width of any SF created by the extended dislocations with in the pile-up is maximum when it is equidistant from both the precipitates. The above observation advocates towards an important fact that the influence of the net stress field associated to the forest dislocations around the precipitates is minimum at the mid position of the DP, and which is not able to restrict the dissociations of perfect dislocations and thereby creating SFs at the mid position of the DP, indicated using a pair of black arrows. Thus, it is likely that the stress field associated with dislocation substructure around the precipitate raises the critical stress for the glide of dislocations along the DP near precipitates' vicinity, and responsible towards the unfaulting dislocation reaction according to Eq. (6.1). Another new microstructural aspect related to the deformation microstructures of the studied steel is presented in Fig. 6.1(d), which clearly demonstrates the first incidence of twin nuclei in the form of three-layer SFs. The twin nuclei regions in Fig. 6.1(d) are encircled, while their enlarged view clearly reveals the occurrence of three-layer SFs. It is well known that such three-layer SF twin nucleus under two-beam dynamical conditions reveals a characteristic periodic contrast of the SPDs bounding the overlapped SF pairs, which is reported in several studies (Mahato et al., 2015; Kim et al., 2017; Mahato et al., 2017), and that these SF pairs continue to grow one above another to yield a macroscopic twin lamella (Mahato et al., 2015).

It is generally regarded that dislocation slip and twinning are competitive mechanisms in coarse-grained (CG) metals/alloys, and a critical dislocation activity governed by dislocation slip length and density is required before any deformation twin nucleation in the microstructures (El-Danaf et al., 1999). In contrary, the strain accommodation associated with the onset of twinning in nano crystal (NC) cases is accomplished through various grain boundary (GB) mediated mechanisms, which mainly involves the emission and/or glide of SPDs and leaving behind intrinsic stacking faults (ISFs) as a result of their glides (Zhu et al., 2012; Wang et al., 2010, 2014, 2017; Warner et al., 2007). However, the set of TEM BF microstructures presented in Fig. 6.1 clearly revealed that any other activities of a perfect dislocations having Burgers vectors

$\frac{a}{2}\langle 110\rangle$ were not prevalent at this strain level excluding the previously described unfaulting reactions according to Eq. (6.1), even though twin nucleation were observed at this strain level as described in Fig. 6.1(d). This directly questions about the active twinning mechanism operating in the present precipitation hardened MMn steel, while any significant dislocation activity is absence in the deformation microstructures. In an attempt to resolve this issue, it is therefore imperative to focus the concentration on two aspects, firstly, how exactly the SFs are created in the course of deformation, and secondly, their sequential overlapping on the successive close packed $\{111\}$ planes so that the combination is regarded as a twin nucleus, which are discussed below.

6.1.2 Activation of a hybrid-twining mechanism

The HRTEM investigations and the corresponding inverse fast Fourier transform (IFFT) analysis of the 0.02 strained specimen are presented in Fig. 6.2, which reveals some interesting propositions that would not only shed some light on the twinning mechanism active in the present MMn steel, but also the role of the precipitates on the twinning behavior of the steel. In Fig. 6.2(a), a fringed region is observed within the austenite matrix and such fringed regions are recently shown to arise due to SFs with at least one atomic layer distance, rather than an alternated SF pair, behaving like a twin precursor through a non-classical twinning method (Ghiasabadi Farahani et al., 2020). In other words, these fringed regions were observed in the deformation microstructure when twinning is realized according to a non-classical method (Ghiasabadi Farahani et al., 2020). The lattice image presented in Fig. 6.2(b) acquired along $B \approx [0\bar{1}1]$ also strengthens the argument about the incidence of overlapped one atomic layer SF regions within the microstructure and such prevalence is not sporadic in nature. The corresponding IFFT image of the delineated region of Fig. 6.2(b) is presented in Fig. 6.2(c), and which clearly reveals even few more interesting propositions, which are now discussed below.

Along with IFFT image, additionally Fig. 6.2(c) also contains the local g-maps related to the individual dislocations, and which was based on an image processing technique that captures even the small displacements of the lattice fringes in HRTEM

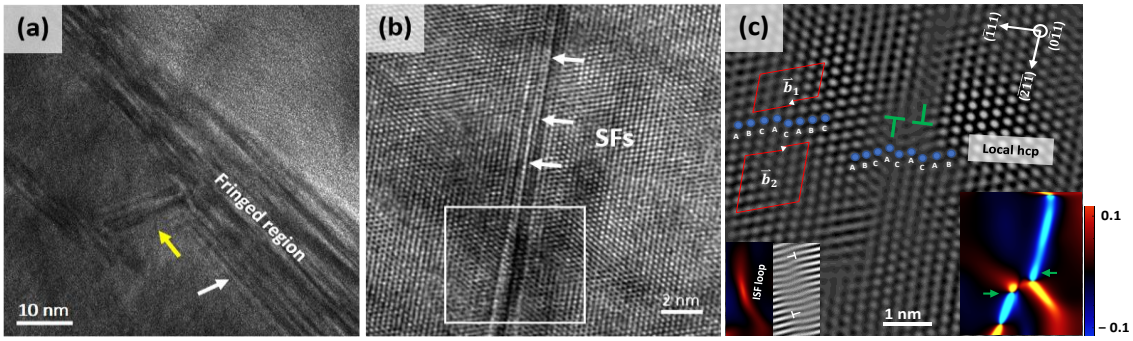

Fig. 6.2: HRTEM microstructures at true strain: 0.02: (a) fringed region serving as twinning precursors through alternated SF pairs in two different slip systems indicated by black and yellow arrows (b) higher magnification image of SFs along $B \approx [0\bar{1}1]$ (c) IFFT image of the white delineated region (b), Frank partials produced according to Eq. (2) are labeled as green "⊥". An ISF loop is also bound by two Shockley partials having opposite Burgers vectors ($\vec{b}_1$ and $\vec{b}_2$). The g-map and filtered IFFT image of the left lower inset shows that the ISF loop is bound by two 30° Shockley partials having opposite Burgers vectors: $\frac{a}{6}[\bar{2}\bar{1}\bar{1}]$ and $\frac{a}{6}[211]$. The g-map from the local hcp region (middle region) along $[\bar{2}\bar{1}\bar{1}]$ is shown in right lower inset. The indigo and yellow legends therein, respectively indicate the maximum compressive and tensile strains around the partial and full dislocations in the region.

images, and a mask is applied during IFFT processing with a particular diffraction vector (g-vector) of interest (Hÿtch et al., 2003). The g-maps and filtered IFFT image in the lower left inset of Fig. 6.2(c) would allow one to identify two 30° mixed character of leading Shockley partial loops without the trailing loops having opposite Burgers vectors: $\frac{a}{6}[\bar{2}\bar{1}\bar{1}]$ and $\frac{a}{6}[211]$. The *ab-initio* calculations for fcc metals, based on the generalized SFE theory suggest that when an ISF is formed due to passage of the leading partial, the trailing partial needs to overcome a nucleation and gliding barrier which is a function of the ratio of unstable SFE, *i.e.* energy barrier that is to be overcome for nucleation of a SF (γ_{usf}) to intrinsic SFE (γ_{isf}), and partials are expected for: $\frac{\gamma_{usf}}{\gamma_{isf}} \gg 1$, while no dissociation of $\frac{a}{2}\langle 110\rangle$ dislocation should occur for: $\frac{\gamma_{usf}}{\gamma_{isf}} \approx 1$ (Jin et al., 2011). The γ_{usf} value of the present steel based on a previous study (Ghiasabadi Farahani et al., 2020) was approximated as ~ 280 mJ/m^2, relying on

the consideration that γ_{usf} is so large in comparison to γ_{isf} (~ 25 mJ/m^2) that the effect of additional alloying elements can be assumed as insignificant. Furthermore, it has been also reported that γ_{usf} remains largely unaffected by the variations of Mn content in a γ-iron (Boukhvalov et al., 2007; Kioussis et al., 2010), and extending this argument to the present steel, a very high value of $\frac{\gamma_{usf}}{\gamma_{isf}} \approx 11$ is obtained for the present steel, and which clearly indicates that dissociation of a perfect dislocations should occur at this strain level for the studied steel. Since the experimental determinations of the generalized SFEs are not possible, and therefore, the literature values are adapted to interpret the deformation microstructure.

A further critical observation from the middle region of the IFFT presented in Fig. 6.2(c) demonstrate the formation of two ISFs identified on the basis of stacking sequences; $ABCA/CA/CAB$ representing a local hcp crystal structure, and which is synonymous to the formation of an alternated SF pair in the concerned region. The g-map obtained from this region *i.e*. the alternated SF pair region of Fig. 6.2(c) along the direction of $[\bar{2}\bar{1}\bar{1}]$ is shown in the lower right inset, and that additionally indicate the presence of a pair of Frank partial dislocation delineated using the green symbol "⊥" in Fig. 6.2(c), which allows to understand that the alternated SF pair representing the local hcp region is most likely formed through dissociation of a $\frac{a}{2}\langle 110\rangle$ perfect dislocation according to the dislocation reaction:

$$\frac{a}{2}[011] \rightarrow \frac{a}{6}[211] + \frac{a}{3}[\bar{1}11] \qquad (8.2)$$

The presence of dissociated lattice dislocations and ISF loops in Fig. 6.2(c) directly indicate that away from the locations of the V(C,N) precipitates, dissociation of $\frac{a}{2}\langle 110\rangle$ dislocations should occur with in the matrix due to a high value of the $\frac{\gamma_{usf}}{\gamma_{isf}}$ ratio ~ 11, while stress field associated to the dislocation substructure around the precipitate modify the energy barriers near the precipitates, and a consequent increase in γ_{isf} in their vicinity would result in lowering the $\frac{\gamma_{usf}}{\gamma_{isf}}$ value from its actual value. Therefore, the dissociation of $\frac{a}{2}\langle 110\rangle$ dislocations in the immediate neighborhood regoins of the V(C,N) precipitates would be prevented. On the other hand, the prevalence of local hcp structures in the Fig. 6.2 (c) also provides a distinct indication that a non-classical twinning route, namely, the alternated SF pair mechanism, which

commonly known to be valid in NC systems is also operating for the studied steel. According to this non-classical twinning mechanism, a third ISF has to be nucleated in between the previously formed SF pair (*i.e.* the twinning precursor) to subsequently convert it into a three-layer twin lamella (Wang et al., 2017). Thus, the information that observed from the Fig. 6.2 collectively indicate towards an interesting fact that the active deformation mechanism in the vicinity of V(C,N) precipitates emulate a NC metal/alloy like situation, and which is introspected in what follows.

It is known that any increment in γ_{usf} value has the effect of elevating the energy barrier i.e. $\gamma_{usf} - \gamma_{isf}$ value, while the nucleation of any trailing partial needs to overcome this energy barrier (Rice et al., 1992). Therefore, the absence of trailing partial loops in Fig. 6.2(c) should be deciphered in terms of an increase in γ_{usf}, which is equivalent to elevation of energy barrier $(\gamma_{usf} - \gamma_{isf})$ for the generation of a SF and consequently, the formation any new SF is also destitute. Since the energy barrier; $\gamma_{usf} - \gamma_{isf}$ is gradually lowered towards the precipitate due to local elevation of γ_{isf}, this situation would suppress any twin formation there due to restrictions on the nucleation of a second leading SPD on the second atomic plane. The TEM microstructures of Fig. 6.1 also strengthen this conjecture from the high density of dislocations readily seen in the vicinity of precipitates and the associated stress field that subsequently elevates the local SFE of the microstructure (Boukhvalov et al., 2007; Mahato et al., 2015), and a SF formation in the vicinity of the precipitates is quite unlikely in such instances. The unfaulting reaction in Fig. 6.1(c) is a further reaffirmation of the fact that SF formation is not preferred in the immediate vicinity of the precipitates, where the local γ_{usf} is relatively higher.

It is worth mentioning that V(C,N) precipitation would cause a local C depletion in the matrix, and consequent lowering of local γ_{isf}. It is however, reported that experimentally determined γ_{isf} value in Fe-Mn-Si-Al steels containing simple dislocation substructures can manifest more than two-fold increase due to its interaction with SFs (Mahato et al., 2015). Therefore, it is reasonable to expect that any drop in γ_{isf} due to C depletion would be overwhelmed by the dislocations' stress field effect on the SFs. Furthermore, a multitude of SFs in Fig. 6.1 ensures that it would be relatively easy for the deformation twins to nucleate at the end away from the

precipitates. Once a local hcp layer is formed, a twinning SPD having the same Burgers vector as the initial leading partial could be emitted on the intermediate plane

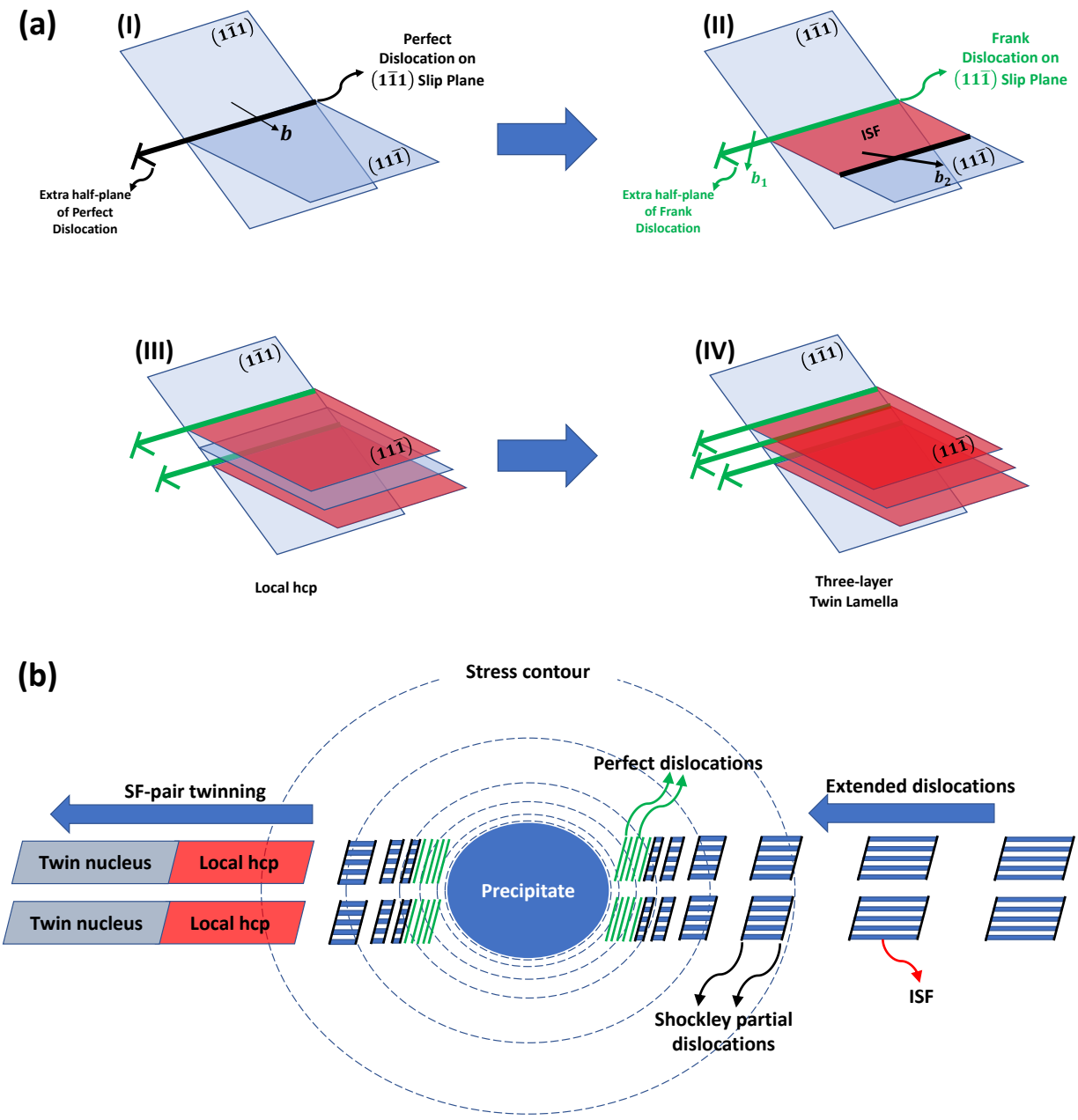

Fig. 6.3: Schematic illustrations of: (a) SF nucleation and alternated SF-pair twinning mechanism and (b) comprehensive picture of microstructure evolution due to presence of precipitate.

to nucleate a twin. Alternatively, a trailing partial could also be emitted, which would erase the SF. However, it is predicted that below a critical grain size, the nucleation of a twinning SPD is easier than emitting a trailing partial (Pierce et al., 2014). Yamakov

et al. (2001) further report that the twinning SPDs emitted from the GBs of NC metals/alloys experience a very high local stress, and that the movement of the trailing SPDs into grain interior is suppressed unless the grain size exceeds a critical value. Therefore, the absence of trailing partial loops in Fig. 6.2 could be reasonably attributed to the high local stress fields around the precipitates (Fig. 6.1) transforming the deformation mechanism in the surrounding matrix to that observed in NC systems.

In classical theory, equilibrium width of SF depends only on γ_{isf} (Hirth & Lothe, 1968), and it cannot explain the finer SFs observed in Fig 8.1, despite the steel possessing a low γ_{isf} ~ 25 mJ/m^2. This however, could be explained by modern dislocation dynamics studies for NC fcc metals that the equilibrium width depends not on γ_{isf} alone, but on the energy barrier, $\gamma_{usf} - \gamma_{isf}$, which must be overcome for any widening of SFs (Hunter et al., 2013). Therefore, the deformation mechanism in the present steel is now introspected from a NC metal/alloy viewpoint. It is known that narrower SFs are expected in NC Cu and Al having $\gamma_{usf} - \gamma_{isf}$ values: 122 mJ/m^2 and 28 mJ/m^2, respectively (Jin et al., 2011). The equilibrium SF width directly influences the deformation mechanism, particularly in NC metals, and that the width depends on – grain size, temperature and applied stresses (Van Swygenhoven et al., 2004; Hunter et al., 2013). The prevalence of narrower SFs in Fig 8.1 indeed advocates according to Hunter et al. (2013) that the barrier: $\gamma_{usf} - \gamma_{isf}$ in the present steel is effectively lowered from its calculated value: (280 – 25) mJ/m^2 ≈ 255 mJ/m^2 to inhibit any widening of SFs. At the same time, the multitude of SFs in Fig. 6.1 and the fringed region in Fig. 6.2 (a) would further ensure that twins should nucleate through overlap of SFs once the energy barrier is surpassed, while the activation of non-classical alternated SF pair mechanism is ascribed to the $\frac{\gamma_{usf}}{\gamma_{isf}}$ ratio (Wang et al., 2017; Ghiasabadi Farahani et al., 2020). The active deformation mechanism related to the deformation microstructure of the studied steel is further summarized and schematically presented in Fig. 6.3.

References

Boukhvalov, D.W., Gornostyrev, Y.N., Katsnelson, M.I., Lichtenstein, A.I. (2007) *Phys. Rev. Lett*. **99**, 247205.
Dinsdale, A.T., (1991) *Calphad* **15**, 317–425.
El-Danaf, E., Kalidindi, S.R., Doherty, R.D. (1999) *Metall. Mater. Trans. A* **30**, 1223–1233.
Ghiasabadi Farahani, M., Zarei-Hanzaki, A., Abedi, H.R., Kim, J.H., Jaskari, M., Sahu, P., Karjalainen, L.P. (2020) *Scr. Mater*. **178**, 301–306.
Hirth, J.P. & Lothe, J. (1968) Theory of Dislocations, NewYork: McGraw-Hill.
Hunter, A., Zhang, R.F., Beyerlein, I.J., Germann, T.C., Koslowski, M. (2013) *Model. Simul. Mater. Sci. Eng.* **21**, 25015.
Hull, D. & Bacon, D.J. (2011) Introduction to Dislocations, Fifth Edition, Butterworth-Heinemann, Oxford.
Hÿtch, M.J., Putaux, J.-L., Pénisson, J.-M. (2003) *Nature* **423**, 270–273.
Jin, Z.H., Dunham, S.T., Gleiter, H., Hahn, H., Gumbsch, P. (2011) *Scr. Mater*. **64**, 605–608.
Kim, J.-K., Kwon, M.-H., De Cooman, B.C. (2017) *Acta Mater*. **141**, 444-455.
Kioussis, N.G., Ghoniem, N.M., Comput. J. (2010) *Theor. Nanosci*. **7**, 1317-1346.
Mahato, B., Sahu, T., Shee, S.K., Sahu, P., Sawaguchi, T., Kömi, J., Karjalainen, L.P. (2017) *Acta Mater*. **132**, 264–275.
Mahato, B., Shee, S.K., Sahu, T., Ghosh Chowdhury, S., Sahu, P., Porter, D.A., Karjalainen, L.P. (2015) *Acta Mater*. **86**, 69–79.
Müllner, P., Ferreira, P.J. (1996) *Philos. Mag. Lett*. **73**, 289–298.
Pierce, D.T., Jiménez, J.A., Bentley, J., Raabe, D., Oskay, C., Wittig, J.E. (2014) *Acta Mater*. **68**, 238–253.
Rice, J.R., Mech. J. (1992) *Phys. Solids* **40**, 239–271.
Van Swygenhoven, H., Derlet, P.M., Frøseth, A.G. (2004) *Nat. Mater*. **3**, 399–403.
Wang, L., Guan, P., Teng, J., Liu, P., Chen, D., Xie, W., Kong, D., Zhang, S., Zhu,
Wang, L., Han, X., Liu, P., Yue, Y., Zhang, Z., Ma, E. (2010) *Phys. Rev. Lett*. **105**, 135501.
Wang, L., Teng, J., Liu, P., Hirata, A., Ma, E., Zhang, Z., Chen, M., Han, X. (2014) *Nat. Commun*. **5**, 4402.
Warner, D.H., Curtin, W.A., Qu, S. (2007) *Nat. Mater*. **6**, 876–881.
Yamakov, V., Wolf, D., Salazar, M., Phillpot, S.R., Gleiter, H. (2001) *Acta Mater.* **49**, 2713–2722.
Zhang, T., Ma, Z., Chen, E., Han, M., (2017) *Nat. Commun*. **8**, 1–7.
Zhu, Y.T., Liao, X.Z., Wu, X.L. (2012) *Prog. Mater. Sci*. **57**, 1–62.

Chapter 7

Summary and conclusions

7.1 General conclusions

In this thesis a comprehensive comparison of various experimental methods for estimating the SFE of a high-Mn steel was carried out under the framework of the dissertation, and the corresponding deformation behaviour of some medium/high-Mn steels under monotonous and cyclic deformations were then interpreted using the concept local/global SFE of those steels. The quasi-static monotonous deformation of medium-Mn Fe-0.17C-2.2Si-10.8Mn-18.0Cr-4.7Ni-0.9V-0.25N (all in wt.%) steel were carried until failure with a strain rate of 10^{-3} s^{-1}, while the high-Mn Fe–16Mn–1.5Al–0.3C steels were deformed under HCF regime. The XRD data acquisitions of the differently deformed specimens were carried out to know the quantitative evolution of structural and microstructural information. EBSD measurements were performed using a high-resolution field emission scanning electron microscope, while the TEM investigations were carried out to observe the deformation microstructure and identify the active deformation mechanisms. Based on the results the following conclusions can be drawn:

- The high-cycle bending fatigue deformation of coarse-grained (~ 25 μm) and graded-grained high-Mn austenitic steel revealed that in both cases the Vickers microhardness initially increased due to cyclic hardening and almost saturated at prolonged cycling. Initial cyclic hardening was observed until 20000 cycles in graded grained specimen, while this decreases to 10000 cycles for the CG specimen.
- The lattice strain values along the individual crystallographic directions were $\sim 10^{-4}$, and the associated dislocation densities in both the specimens were also quite low (~ 10^{14} m^{-2}), and which decreased further at higher cycles due to recovery of dislocations.
- Depending on the grain sizes the deformation mechanisms in the graded-grained specimen varied widely; stacking faults were predominant in the fine grains (~ 2 μm), while interconnected dislocation cells representing a low energy dislocation structure (LEDS) were observed within the larger grains (~ 5 μm). Deformation twins were scarce and observed only within a finer grain when the stacking faults in the microstructure overlapped after saturation stage.

- For CG specimen, the imposed cyclic plastic strain in the pre-saturation stage was accommodated through perfect and extended dislocations' slip and formation of shear bands, while trace amount of deformation induced ϵ-martensite at intersections of shear bands was detected at the saturation stage.
- The SFE of the medium-Mn steel was estimated as ~ 25 mJ/m^2 from sub regular solution model, while the effective SFE of CG and graded grained steel was estimated as ~ 21 mJ/m^2 and ~ 16 mJ/m^2, respectively.
- In case of monotonous deformation of medium-Mn austenitic steel, twinning nucleation was observed at low true strain ~ 0.02 and the local microstructures i.e. the occurrence of V(C,N) precipitates significantly influenced the deformation mechanism due to the presence a high stress field around the precipitates in the matrix, and that it raised the energy barrier for nucleation of a stacking fault.
- Unfaulting dislocation reaction was favored only near vicinity of the precipitates, while twinning was activated further from the precipitates. The occurrence of stacking faults and any twins were occasionally observed in the immediate vicinity of the precipitates.
- A hybrid mechanism of twin nucleation was observed for the first time, wherein, the stacking faults were created through a classical dislocation dissociation, and the high unstable to intrinsic stacking fault energies ratio of the steel (~ 11) was responsible for overlap of those stacking faults following a non-classical route that subsequently created a three-layer twin.

7.2 Scope for future work

In continuation of the studies on the monotonous and cyclic deformation of high/medium-Mn steels, it is imperative that the following aspects should be planned as future activity.

1 The effective SFE of medium-Mn steel should be estimated according to different experimental techniques using XRD and TEM, and its influence on the cyclic deformation behaviour will be studied.

2 The evolutions of different dislocation substructures, share band, PSB in the cyclic deformation behaviour of high-Mn Fe-Mn-Al-C steels need further inspection using high-resolution TEM investigation.

3 The exact role of local deformation microstructure at higher strain on the monotonous deformation behaviour of medium-Mn steel containing precipitates needs to be addressed more critically using extensive TEM investigation.

Publications

Journal Publications

Scripta Materialia 192 (2021) 83–88

Contents lists available at ScienceDirect

Scripta Materialia

journal homepage: www.elsevier.com/locate/scriptamat

Activation of a hybrid twinning mechanism in a Cr-Ni-Si-V-N medium manganese austenitic steel containing precipitates

S. Shyamal [a], M. Ghiasabadi Farahani [b], T. Allam [c,d], A.S. Hamada [e], C. Haase [c], J.I. Kömi [f], P.C. Chakraborti [g], P. Sahu [a,*]

[a] Department of Physics, Jadavpur University, Kolkata 700 032, India
[b] Hot Deformation and Thermomechanical Processing Laboratory of High-Performance Engineering Materials, School of Metallurgy and Materials Engineering, College of Engineering, University of Tehran, Tehran, Iran
[c] Steel Institute (IEHK), RWTH Aachen University, 52056 Aachen, Germany
[d] Department of Metallurgical and Materials Engineering, Suez University, 43528 Suez, Egypt
[e] Kerttu Saalsti Institute, University of Oulu, Pajatie 5, Nivala FIN-85500, Finland
[f] Centre for Advanced Steels Research, Box 4200, University of Oulu, FIN-90014 Oulu, Finland
[g] Department of Metallurgical and Material Engineering, Jadavpur University, Kolkata 700 032, India

Materials Letters 285 (2021) 129002

Contents lists available at ScienceDirect

Materials Letters

journal homepage: www.elsevier.com/locate/mlblue

Graded deformation in an Fe-Mn-Al-C steel under bending fatigue

S. Shyamal [a], S.R. Das [a], M. Jaskari [b], D.A. Porter [c], L.P. Karjalainen [c], P. Sahu [a,*]

[a] Department of Physics, Jadavpur University, Kolkata 700 032, India
[b] Kerttu Saalasti Institute, University of Oulu, FIN-85500, Finland
[c] Centre for Advanced Steels Research, University of Oulu, FIN–90014, Finland

Materials Letters 327 (2022) 133006

Contents lists available at ScienceDirect

Materials Letters

journal homepage: www.elsevier.com/locate/matlet

Evolution of deformation microstructure in a coarse-grained Fe-Mn-Al-C steel under bending fatigue

S. Shyamal [a], S.R. Das [a], M. Jaskari [b], P. Sahu [a,*]

[a] Department of Physics, Jadavpur University, Kolkata 700 032, India
[b] Kerttu Saalasti Institute, University of Oulu, FIN 85500, Finland

Materialia 15 (2021) 101042

Contents lists available at ScienceDirect

Materialia

journal homepage: www.elsevier.com/locate/mtla

Full Length Article

On the mechanism of cross-slip induced dislocation substructure formation in an high-Mn steel

S.R. Das [a], S. Shyamal [a], T. Sahu [b], J.I. Kömi [c], P.C. Chakraborti [d], D.A. Porter [c], L.P. Karjalainen [c], P. Sahu [a,*]

[a] Department of Physics, Jadavpur University, Kolkata 700 032, India
[b] Department of Physics, S.A. Jaipuria College, Kolkata 700 005, India
[c] Centre for Advanced Steels Research, University of Oulu, Box 4200, FIN–90014, Finland
[d] Department of Metallurgical and Material Engineering, Jadavpur University, Kolkata 700 032, India

Materials Letters 324 (2022) 132730

Contents lists available at ScienceDirect

Materials Letters

journal homepage: www.elsevier.com/locate/matlet

Transmission electron microscopy investigations on the twinning suppression attributes in a Fe-Mn-Al-C steel and the associated strain hardening

S.R. Das [a], S. Shyamal [a], M. Jaskari [b], P.C. Chakraborti [c], L.P. Karjalainen [d], P. Sahu [a,*]

[a] Department of Physics, Jadavpur University, Kolkata 700 032, India
[b] Kerttu Saalasti Institute, University of Oulu, FIN-85500, Finland
[c] Department of Metallurgical and Material Engineering, Jadavpur University, Kolkata 700 032, India
[d] Centre for Advanced Steels Research, University of Oulu, FIN-90014, Finland

Materials Letters 300 (2021) 130216

Contents lists available at ScienceDirect

Materials Letters

journal homepage: www.elsevier.com/locate/matlet

A quantitative assessment on the contribution of various dislocation substructures to flow stress in a fine-grain high-Mn steel

S.R. Das [a], T. Riaz [a], S. Shyamal [a], P.C. Chakraborti [b], P. Sahu [a,*]

[a] Department of Physics, Jadavpur University, Kolkata 700 032, India
[b] Department of Metallurgical and Material Engineering, Jadavpur University, Kolkata 700 032, India

Materials Characterization 172 (2021) 110833

Contents lists available at ScienceDirect

Materials Characterization

journal homepage: www.elsevier.com/locate/matchar

X-ray line profile analysis of the deformation microstructure in a medium-grained Fe-Mn-Al-C austenitic steel

S.R. Das [a], S. Shyamal [a], S.K. Shee [b], J.I. Kömi [c], P. Sahu [a,*]

[a] Department of Physics, Jadavpur University, Kolkata 700 032, India
[b] Department of Physics, Midnapore College, Midnapore 721 101, West Bengal, India
[c] Centre for Advanced Steels Research, University of Oulu, Box 4200, FIN 90014, Finland

materials

MDPI

Article

Microstructural Constituents and Mechanical Properties of Low-Density Fe-Cr-Ni-Mn-Al-C Stainless Steels

Steffen Scherbring [1], Guanghui Chen [1], Bastian Veltel [1], Gert Bartzsch [2], Julia Richter [3], Malte Vollmer [3], Malte Blankenburg [4], Saikat Shyamal [5], Olena Volkova [2], Thomas Niendorf [3], Ulrich Lienert [4], Puspendu Sahu [5] and Javad Mola [1,*]

[1] Materials Design and Structural Integrity Laboratory, Faculty of Engineering and Computer Sciences, Osnabrück University of Applied Sciences, 49076 Osnabrück, Germany; steffen.scherbring@hs-osnabrueck.de (S.S.); chenguanghui@wust.edu.cn (G.C.); baveltel@gmail.com (B.V.)
[2] Institute of Iron and Steel Technology, Technische Universität Bergakademie Freiberg, 09599 Freiberg, Germany; gert.bartzsch@iest.tu-freiberg.de (G.B.); volkova@iest.tu-freiberg.de (O.V.)
[3] Institute of Materials Engineering—Metallic Materials, University of Kassel, 34125 Kassel, Germany; julia.richter@uni-kassel.de (J.R.); vollmer@uni-kassel.de (M.V.); niendorf@uni-kassel.de (T.N.)
[4] Deutsches Elektronen-Synchrotron (DESY), Photon Science, 22607 Hamburg, Germany; malte.blankenburg@desy.de (M.B.); ulrich.lienert@desy.de (U.L.)
[5] Department of Physics, Jadavpur University, Kolkata 700032, India; saikat.shyamal923@gmail.com (S.S.); psahu74@gmail.com (P.S.)
* Correspondence: j.mola@hs-osnabrueck.de

Materials Characterization 196 (2023) 112567

Contents lists available at ScienceDirect

Materials Characterization

journal homepage: www.elsevier.com/locate/matchar

X-ray line profile analysis on the deformation microstructure of Al-bearing high-Mn steels

T. Riaz [a], S. Shyamal [a], S.K. Shee [b], L.P. Karjalainen [c], P. Sahu [a,*]

[a] Department of Physics, Jadavpur University, Kolkata 700 032, India
[b] Department of Physics, Midnapore College, Midnapore 721 101, West Bengal, India
[c] Centre for Advanced Steels Research, University of Oulu, FIN–90014, Finland